Title
Towards the Detection of an Abelian Dark Sector

Author
Smolinsky, Jordan Abraham

Publication Date
2019

Peer reviewed|Thesis/dissertation

UNIVERSITY OF CALIFORNIA,
IRVINE

Towards the Detection of an Abelian Dark Sector

DISSERTATION

submitted in partial satisfaction of the requirements
for the degree of

DOCTOR OF PHILOSOPHY

in Physics

by

Jordan Smolinsky

Dissertation Committee:
Professor Jonathan L. Feng, Chair
Professor Arvind Rajaraman
Professor Manoj Kaplinghat

2019

DEDICATION

In memory of
Jerry Alan Smolinsky

TABLE OF CONTENTS

LIST OF FIGURES

Page

LIST OF TABLES

ACKNOWLEDGMENTS

Academic science is a community endeavour. In doing the work that makes up this dissertation I am grateful for the mentorship, support, and insight I received by working with my primary two collaborators and mentors, Jonathan L. Feng, who is also my PhD advisor, and Flip Tanedo. I would like to thank Ivone Albuquerque, Pietro Baratella, James Bullock, Gustavo Burdman, Marco Cirelli, Eugenio Del Nobile, Anthony DiFranzo, Bertrand Echenard, Rouven Essig, Adam Green, Francis Halzen, Eder Izaguirre, Yoni Kahn, Gordan Krnjaic, Adam Leibovich, Fabian Machate, Cameron Mahoney, Gopolang Mohlabeng, Simona Murgia, Maxim Pospelov, Aldo Serenelli, Stefan Schael, Brian Shuve, Tim M.P. Tait, Alex Wijangco, Hai-Bo Yu, and Andrew Zentner, for discussions that contributed to the work presented here.

The work presented in this dissertation is supported in part by NSF Grant Nos. PHY–1316792 and PHY–1620638 and by Department of Education GAANN Grant No. P200A150121 at UC Irvine.

I would like to thank the professors of the UC Irvine particle theory group, who most directly shaped my development as a physicist: Jonathan L. Feng, Tim M.P. Tait, Arvind Rajaraman, Yuri Shirman, Mu-Chun Chen, and Michael Ratz.

For all the times I wanted to talk about physics or lounge on a couch without the pressure of talking to someone with tenure, I am grateful to Flip Tanedo, Iftah Galon, Bart Fornal, Sebastian Trojanowski, and Felix Kling.

For making the grad office fun as well as a decent working and learning environment, I want to thank Anthony Difranzo, Alex Wijangco, Mohammad Abdullah, Ben Lillard, Sunny Yu, Arianna Braconi, Alexis Romero, and Michael Waterbury.

Grad school is an immense personal undertaking. As in all things it is important to have a support structure around us in different aspects of our lives. To that end I want to thank Dwight Spires, Dave Fisher, Lubo and Rossina Kolev, and Joe Luttrell, who pushed me to improve myself physically and sharpened my beach volleyball game.

Last, but definitely not least, I want to thank the people who gave me the most personal support, outside of the academic realm. Thank you to my mother Hannah Smolinsky. Thank you to my sister Halle Smolinsky. Thank you to my dearest friends Daniel and Brian Coffee, Andy Fernandez, Andrew Greminger, and Perry Leventhal for all the innumerable ways you have improved my life by being part of it.

CURRICULUM VITAE

Jordan Smolinsky

EDUCATION

Doctor of Philosophy in Physics **2019**
University of California, Irvine *Irvine, California*

Bachelor of Arts in Physics **2014**
University of California, Berkeley *Berkeley, California*

RESEARCH EXPERIENCE

Graduate Research Assistant **2014–2019**
University of California, Irvine *Irvine, California*

TEACHING EXPERIENCE

Teaching Assistant **2014–2019**
University of California, Irvine *Irvine, California*

Grader **2013**
University of California, Berkeley *Berkeley, California*

ARTICLES

1. A. Rajaraman and J. Smolinsky, "Self-Interacting Dark Matter Through the Majoron Portal," `arXiv:1811.06619 [hep-ph]`

2. J. L. Feng and J. Smolinsky, "Impact of a resonance on thermal targets for invisible dark photon searches," *Phys. Rev.* **D96** no. 9, (2017) 095022, `arXiv:1707.03835 [hep-ph]`

3. J. Smolinsky and P. Tanedo, "Dark Photons from Captured Inelastic Dark Matter Annihilation: Charged Particle Signatures," *Phys. Rev.* **D95** no. 7, (2017) 075015, `arXiv:1701.03168 [hep-ph]`. [Erratum: Phys. Rev.D96,no.9,099902(2017)]

4. J. L. Feng, B. Fornal, I. Galon, S. Gardner, J. Smolinsky, T. M. P. Tait, and P. Tanedo, "Particle physics models for the 17 MeV anomaly in beryllium nuclear decays," *Phys. Rev.* **D95** no. 3, (2017) 035017, `arXiv:1608.03591 [hep-ph]`

5. J. L. Feng, B. Fornal, I. Galon, S. Gardner, J. Smolinsky, T. M. P. Tait, and P. Tanedo, "Protophobic Fifth-Force Interpretation of the Observed Anomaly in ^{8}Be Nuclear Transitions," *Phys. Rev. Lett.* **117** no. 7, (2016) 071803, `arXiv:1604.07411 [hep-ph]`

6. J. L. Feng, J. Smolinsky, and P. Tanedo, "Detecting dark matter through dark photons from the Sun: Charged particle signatures," *Phys. Rev.* **D93** no. 11, (2016) 115036, `arXiv:1602.01465 [hep-ph]`. [Erratum: Phys. Rev.D96,no.9,099903(2017)]

7. J. L. Feng, J. Smolinsky, and P. Tanedo, "Dark Photons from the Center of the Earth: Smoking-Gun Signals of Dark Matter," *Phys. Rev.* **D93** no. 1, (2016) 015014, `arXiv:1509.07525 [hep-ph]`. [Erratum: Phys. Rev.D96,no.9,099901(2017)]

8. A. Rajaraman, J. Smolinsky, and P. Tanedo, "On-Shell Mediators and Top-Charm Dark Matter Models for the Fermi-LAT Galactic Center Excess," `arXiv:1503.05919 [hep-ph]`

COLLABORATIONS

1. **FASER** Collaboration, A. Ariga *et al.*, "FASER: ForwArd Search ExpeRiment at the LHC," `arXiv:1901.04468 [hep-ex]`

2. **FASER** Collaboration, A. Ariga *et al.*, "Technical Proposal for FASER: ForwArd Search ExpeRiment at the LHC," `arXiv:1812.09139 [physics.ins-det]`

3. **FASER** Collaboration, A. Ariga *et al.*, "FASER's Physics Reach for Long-Lived Particles," `arXiv:1811.12522 [hep-ph]`

PROCEEDINGS

1. M. Battaglieri *et al.*, "US Cosmic Visions: New Ideas in Dark Matter 2017: Community Report," `arXiv:1707.04591 [hep-ph]`

PROFESSIONAL DEVELOPMENT

1. **Pheno 2018**, University of Pittsburgh, May 2018

2. **Prospects in Theoretical Physics**, IAS Princeton, July 2017

3. **Theoretical Advanced Studies Institute**, University of Colorado, Boulder, June 2016

4. **UCLA Dark Matter**, UCLA, February 2016

5. **Pre-SUSY Symposium**, UC Davis, August 2015

ABSTRACT OF THE DISSERTATION

Towards the Detection of an Abelian Dark Sector

By

Jordan Smolinsky

Doctor of Philosophy in Physics

University of California, Irvine, 2019

Professor Jonathan L. Feng, Chair

Dark matter remains the foremost sign of particle physics beyond the Standard Model. Little is known about its microscopic properties, but there are compelling astrophysical and cosmological reasons to believe that it resides in a "dark sector" with its own forces, and with weak coupling to the Standard Model. One popular theory which may explain these dark matter interactions is known as the "kinetic mixing portal" wherein a "dark photon" of a new abelian gauge symmetry is induced to mix with the Standard Model photon, and thus to mediate interactions with the visible sector. In this dissertation we will examine the phenomenology of this theory. As dark matter travels through the galaxy it may scatter off of nuclei through dark photon exchange, losing enough energy to become gravitationally trapped and accumulate in astrophysical bodies. We propose and examine in detail a search for the dark photons radiated by this trapped population of dark matter in Chapters 2, 3, and 4, finding that there are viable regions of parameter space that cannot be probed by direct detection but would be amenable to discovery by this search. In Chapter 5 we perform a detailed calculation of the dark matter abundance in theories where dark matter annihilates through the kinetic mixing portal. We find that the reach of current dark photon search experiments are remarkably sensitive to the mass of the dark photon near resonance and place an absolute lower limit on the thermal relic parameters of scalar dark matter coupled to a dark photon.

Chapter 1

Introduction

1.1 21st Century Particle Phenomenology and the Dark Matter Problem

Despite the remarkable success of the Standard Model (SM) in describing the interactions of all directly observed elementary particles, we know it is not the final fundamental theory of nature. Many phenomena still evade sufficient description. For one, it is believed that such a final theory must include an understanding of quantum gravity near the Planck scale. But even from the decidedly classical dynamics of stars and galaxies, it is readily apparent that the SM is missing pieces. This mystery of 1930s astrophysics, now specified as the question of particle dark matter, remains the clearest empirical indicator that our sub-Planckian particle zoo is incomplete.

Dark matter was discovered through its gravitational influence [13, 14, 15], and though there have been several tantalizing signals, it has not been confirmed that dark matter interacts with the SM in any other way. At the same time, quantum field theory has shown to be successful in describing the dynamics of all observed particles, and it emerged as the unique synthesis of quantum theory and special relativity. Whatever dark matter is, it must be embodied in a quantum field theory. But how can we determine the properties of that theory? What are its symmetries? What matter particles does it contain, and how do they interact among themselves? To answer these questions, dark matter phenomenologists employ our portion of the scientific method: we propose new theories that fit established empirical and internal consistency criteria, and we predict new phenomena to create new checks on established theories.

Broadly speaking, there are two complementary currents in model building. On the one hand there is the focus on top-down model building, tending towards a final theory that resolves the SM's internal mysteries. For instance, the Higgs mass is stabilized in supersymmetry by the presence of a fermionic superpartner for every boson and a bosonic superpartner for

every fermion (see e.g. [16] for a review), and grand unified theories embed the SM's gauge group into some larger group, collecting the SM fermions into GUT multiplets [17]. The profusion of new particles and interactions required to fill out these theories often include several dark matter candidates. But different UV theories can produce the same IR physics. If we are motivated primarily to describe the physics at low scales, our analysis will be simplified by adding only one or two particles to the SM at a time. While this approach is less complete, it is appropriate for the current environment of particle physics research. We don't know for sure if dark matter is a fermion or a boson, so it is prudent to eschew the overbearing requirements of UV completeness and work with the simplest possible theory that will meet observations. Let us review what these motivating observations are, before considering common theoretical resolutions.

Dark matter was first proposed in the 1930s as an explanation of the anomalously high velocity dispersions that Zwicky first observed in the Coma cluster [13]. In order to sustain these high velocity dispersions, there must be much more mass in these astrophysical systems than the mass accounted for in visible stars and hot gas. Measurements of the orbital velocity of the galactic disk revealed that orbital velocity stayed close to its high central value even at distances far outside the majority of the visible disk mass [14, 15], similarly suggesting the presence of extra, invisible matter. As observational technology advanced it became possible to measure the expansion of spacetime and subject general relativistic cosmology to experimental tests. Relativity tells us that the dynamics of spacetime are linked to the density of matter and energy on that spacetime, so measurement of the universe's expansion must be complemented by determination of its content. This pushed the missing mass discrepancy to foremost prominence and served as a catalyst for bringing together the previously disparate realms of particle physics, cosmology, and astrophysics to tackle what is now known as the dark matter problem. For a while, it was thought that these odd galactic features could be explained without appeal to a new type of matter, and might be due to modified dynamics. The 21st century observation of the Bullet cluster through the dual

methods of x-ray spectroscopy of hot gas and gravitational lensing by the total mass density of the cluster showed that the dominant component of the galactic mass was weakly-or-non interacting and thus could not be explained by "dim stars", dust, or modified Newtonian dynamics [18]. Study of the thermal history of the early universe in the ΛCDM cosmology has provided invaluable insights in the hunt for dark matter. Density perturbations in the dark matter caused tiny fluctuations in the temperature of the hot baryonic plasma shortly after the Big Bang, which leaves an imprint on the high-multipole anisotropies of the Cosmic Microwave Background. Precision measurements of these anisotropies [19] are now considered the strongest evidence for the existence of nonbaryonic dark matter, and reveal its abundance to be $\Omega_X \equiv \rho_X/\rho_c \approx 0.26$, where ρ_c is the critical density of the universe and ρ_X is the dark matter energy density.

The abundance of dark matter is its best measured quality, and a complete model of dark matter should explain its value. Dark matter's interactions today are so feeble that no existing experiment has observed its decay or production in a collider, it is thought that temperatures were high enough in the early universe to enable the dark and visible sectors to achieve chemical equilibrium. As the universe expanded, the plasma's momenta redshifted and eventually the reactions connecting the dark and visible sectors ceased, freezing in the comoving dark matter density. For a detailed review of this process see [20, 21].

Another hint towards the structure of the dark sector is furnished by further galactic observations. The standard ΛCDM cosmology postulates cold, collisionless dark matter, and its predictions for large scale structure formation appear to be borne out by observation. However, observations at the galactic scale appear to diverge from ΛCDM simulations, which points towards a more exotic picture of the dark sector. Simulations of galaxy formation in the standard cosmology predict more sharply cusped dark matter density profiles than have been observed [22], and the discrepancy can be resolved by postulating that dark matter

experiences self-interactions, with a transfer cross section σ_T on the scale of

$$\sigma_T \equiv \int d\Omega \frac{d\sigma}{d\Omega}(1-\cos\theta) \sim 1 \text{ cm}^2 \frac{m_X}{\text{g}} \ . \tag{1.1}$$

Other unexpected features of galactic dynamics, primarily the "too big to fail" problem [23] and the anomalous diversity of rotation curves [24, 25] may be explained by such a self interaction. In order to enable self-interaction, the dark sector cannot be adequately described with a single field. A minimal self interacting dark sector must contain at least one matter particle and one mediator to induce the interaction.

1.2 Simplified Models and the Vector Portal

What sort of bottom-up theories can we construct to meet these cosmological and astrophysical observations? The dark matter is a SM singlet, so all interactions between the dark sector and the SM must factorize as

$$\mathcal{L}_{\text{portal}} = \sum_i \mathcal{O}^i_{\text{SM}} \mathcal{O}^i_{\text{dark}} \ , \tag{1.2}$$

where $\{\mathcal{O}^i_{\text{SM}}\}$ are SM singlets composed of SM fields and $\{\mathcal{O}^i_{\text{dark}}\}$ are singlets under dark symmetries composed of dark sector fields (and therefore trivially singlets under the SM). This condition is remarkably restrictive on renormalizable operators. There are a few common combinations of operators in the literature, which we will quickly review here.

The Higgs portal [26, 27] may be written in the unbroken phase as

$$\mathcal{L} \supset -g\phi H^\dagger H - \lambda \phi^2 H^\dagger H \ , \tag{1.3}$$

where g carries mass dimension 1, λ is dimensionless, H is the electroweak Higgs doublet,

and ϕ is a dark sector scalar. When the electroweak symmetry is broken these interactions produce mixing between ϕ and the dynamical Higgs boson, which induces a Yukawa coupling to SM fermions proportional to their mass.

The axion portal [28] posits interactions of a pseudoscalar a with fermions and gauge bosons

$$\mathcal{L} \supset \frac{\partial_\mu a}{f_a} \sum_f g_f \bar{f} i \gamma^\mu \gamma^5 f + \frac{a}{f_a} F^{\mu\nu} \widetilde{F}_{\mu\nu} \ , \tag{1.4}$$

where f_a is the axion decay constant.

The vector portal or kinetic mixing portal [29, 30] is given by

$$\mathcal{L} \supset \frac{\varepsilon}{2} F^{\mu\nu} F'_{\mu\nu} \ , \tag{1.5}$$

where F' is the field strength of a new $U(1)$ symmetry of the dark sector, and ε is the dimensionless kinetic mixing parameter. Sometimes in the literature this parameter is denoted by κ or χ. Indeed, to avoid confusion with ϵ, which will denote the dimensionless energy of a dark matter annihilation reaction, we will switch to using κ in Chapter 5.

For the rest of this dissertation we will focus on the vector portal, but before we specialize let us review how these models have met our observations. The portals all enable the dark matter to be in thermal contact with the visible sector during the early universe, and they all constitute candidates for a thermal relic. Though the portals are agnostic to the nature of the dark matter itself, all of the mediators can potentially induce self-interactions in the dark sector [31], though they may not be the only such contributors.

With an eye towards the top-down view of phenomenology, let us motivate the kinetic mixing portal, following the treatment of [29]. The SM already contains a factor of $U(1)_Y$, which in the Higgs regime is mixed with one generator of $SU(2)_L$ to produce the photon. Embeddings of the SM gauge group into GUT theories, such as in [32], include extra factors of $U(1)$, and

Table 1.1: Charge and mass assignments for the matter contents of our toy $U(1)_A \times U(1)_B$ theory.

Field	A	B	Mass
ψ_A	g_A	0	m
ψ_B	0	g_B	m
ψ_{AB}	g_A	$-g_B$	m_{AB}
Ψ_{AB}	g_A	g_B	M_{AB}

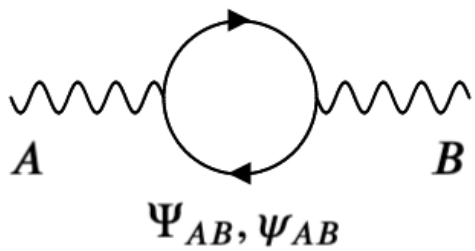

Figure 1.1: Feynman diagram producing kinetic mixing between A and B boson in toy $U(1)_A \times U(1)_B$ theory.

heavy fermions carrying both hypercharge and these new charges. To simplify our analysis we will examine a toy theory under the gauge symmetry $U(1)_A \times U(1)_B$ and populated by four Dirac fermion species, summarized in Table 1.1. We take $M_{AB} > m_{AB} \gg m$ and suppose that at some scale $\Lambda > M_{AB}$ the gauge kinetic terms are canonically normalized, so that the Lagrangian of the theory is

$$-\frac{1}{4}A^{\mu\nu}A_{\mu\nu} - \frac{1}{4}B^{\mu\nu}B_{\mu\nu} + i\sum_f \bar{f}\ \not{D} f - \sum_f m_f \bar{f} f\ , \tag{1.6}$$

where f labels the fermion states $f \in \{\psi_A, \psi_B, \psi_{AB}, \Psi_{AB}\}$, $A^{\mu\nu}$ and $B^{\mu\nu}$ are the field strength tensors associated with the corresponding gauge boson $A_{\mu\nu} \equiv \partial_{[\mu}A_{\nu]}$, and $D_\mu = \partial_\mu + iq_A A_\mu + iq_B B_\mu$ is the gauge covariant derivative of the theory. Now consider the behavior of this theory at some lower scale $m < \Lambda' < m_{AB}$. We need to integrate out the heavy fermions ψ_{AB} and Ψ_{AB}. At one loop these will contribute the desired kinetic mixing through the diagram shown in Fig. 1.1, as well as the wavefunction renormalization of both gauge bosons.

This diagram evaluates to

$$\frac{g_A g_B}{12\pi^2} \log(M_{AB}^2/m_{AB}^2)(p^2 g^{\mu\nu} - p^\mu p^\nu) \ , \tag{1.7}$$

which contributes the term

$$\frac{g_A g_B}{12\pi^2} \log(M_{AB}^2/m_{AB}^2) A^{\mu\nu} B_{\mu\nu} \tag{1.8}$$

to the effective action. We recognize this as the kinetic mixing term of the vector portal, with the kinetic mixing parameter ε defined in terms of the toy parameters as

$$\varepsilon = \frac{g_A g_B}{6\pi^2} \log(M_{AB}^2/m_{AB}^2) \ . \tag{1.9}$$

With $\mathcal{O}(0.1)$ gauge constants this suggests a kinetic mixing parameter on the order of $\varepsilon \sim \mathcal{O}(10^{-3})$. The wavefunction contributions from the other vacuum polarization diagrams are of the same order of smallness as the kinetic mixing, and thus negligible in the effective action when compared to the gauge kinetic terms themselves. The gauge sector of the toy theory is now

$$-\frac{1}{4} A^{\mu\nu} A_{\mu\nu} + \frac{\varepsilon}{2} A^{\mu\nu} B_{\mu\nu} - \frac{1}{4} B^{\mu\nu} B_{\mu\nu} \ , \tag{1.10}$$

while the fermion interactions are

$$-g_A \bar{\psi}_A \not{A} \psi_A - g_B \bar{\psi}_B \not{B} \psi_B \ , \tag{1.11}$$

To perturbatively calculate low energy scattering between ψ_A and ψ_B from this Lagrangian we could simply insert the kinetic mixing vertex. We would also have to consider the series of contributions from having three insertions, and five, and so on. It is more convenient to perform a field redefinition to eliminate the kinetic mixing term. For the details of this transformation, including a complete treatment of mixing with hypercharge in the broken

phase of electroweak theory, see Appendix B. While the effect on the $U(1)_A \times U(1)_B$ field strength tensors is to eliminate the kinetic mixing term, at the level of the potential the transformation becomes, to first order in ε

$$\begin{aligned} A_\mu &\to A_\mu \ , \\ B_\mu &\to B_\mu - \varepsilon A_\mu \ . \end{aligned} \tag{1.12}$$

Thus the field redefinition to eliminate the kinetic mixing term has introduced the new interaction

$$\mathcal{L} \supset \varepsilon g_B \bar{\psi}_B \ \not{A} \psi_B \ . \tag{1.13}$$

To summarize, the renormalization of this theory has produced an ε-suppressed "millicharge" for the fermion ψ_B under the boson A, while there is no such charge for ψ_A under B. In passing from this toy model to a phenomenological study of the dark sector we will identify A with a new dark sector boson we call the "dark photon", and B with the SM hypercharge boson. Similarly we will identify the dark matter with ψ_A and replace ψ_B with SM fermions.

In the following chapters we will explore new ways of testing this theory of dark matter. In Chapters 2, 3, and 4 we realize that the coupling of the dark photon to matter enables the capture of dark matter in the Earth and the Sun. The captured dark matter will annihilate to produce dark photons radiating outwards from the center of astrophysical bodies, and the dark photons will decay to charged particles that can be found with existing experiments. We examine the sensitivity of the IceCube detector at the South Pole and the AMS-02 spectrometer on the ISS to these dark photon decays. In Chapter 5 we will take a closer look at the thermal history of the dark sector. We will see how the presence of a resonant dark photon may allow dark matter to achieve the correct thermal relic abundance while sharply reducing its coupling to the SM, and consider the implications for current and near-future experimental sensitivities.

Chapter 2

Dark Photons from the Center of the Earth

The following is based on a previously published paper by the author, Jonathan L. Feng, and Philip Tanedo [7].

2.1 Introduction

As explained above, dark matter may live in a dark sector with its own forces. If the dark sector contains an Abelian gauge symmetry, dark electromagnetism, the dark photon and the Standard Model (SM) photon will generically mix kinetically. The idea of a separate sector with its own photon [33, 34] and the further possibility of kinetic mixing between these two photons [29, 30] were first explored long ago, and the myriad implications for dark matter detection have recently attracted widespread interest [35, 36].

In this framework, dark matter will collect in the center of the Earth and annihilate to dark photons $XX \to A'A'$. These dark photons may then travel to near the surface of the Earth and decay to SM particles, which may be detected in a variety of experiments, from under-ice/underwater/underground experiments, such as the current experiments IceCube, SuperK, and ANTARES, and future ones, such as KM3NeT, IceCube II, DUNE, and HyperK, to space-based cosmic ray detectors, such as the current experiments Fermi-LAT and AMS-02, and future ones, such as CALET, ISS-CREAM, and others. The resulting signals of electrons, muons, photons, and hadrons that point back to the center of the Earth are potentially striking signals of dark matter.

The possibility of dark matter signals from the centers of large astrophysical bodies was first proposed and investigated many years ago [37, 38, 39, 40, 41, 42, 43, 44, 45, 46], and there have been important advances for the particular case of the Earth in recent years [47, 48, 49, 50, 51, 52, 53, 54, 55]. Typically these signals rely on annihilation to neutrinos, resulting in single-particle signals with a continuum of energies. In contrast, dark photons decay into two charged particles, which may be seen at the same time in a single experiment, and the total energy of these charged particles is equal to the dark matter particle's mass, producing potentially spectacular results.

A schematic picture of this chain of events is given in Fig. 2.1. A number of processes must

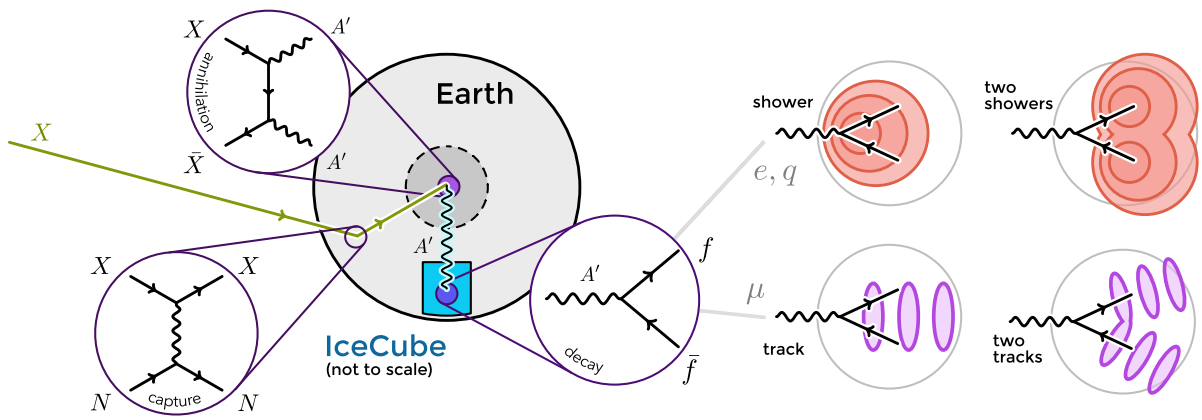

Figure 2.1: Dark matter is captured by elastic $XN \to XN$ scattering off nuclei, collects in the center of the Earth, and annihilates to dark photons, $XX \to A'A'$. These dark photons then travel to near the surface of the Earth and decay to SM particles, which may be detected by a variety of experiments, including neutrino telescopes and space-based cosmic ray detectors. As an example, we show IceCube and various signatures there resulting from A' decays to electrons, muons, and hadrons. We discuss the possibility that double tracks (showers) may be resolved spatially (temporally) in the detector.

be evaluated to determine the resulting signal. For the specific case of dark photons, it is tempting to simplify the analysis by making a number of assumptions. For example, one may assume that the dark matter capture and annihilation processes have reached equilibrium in the Earth and that the capture cross section has some fixed value, such as the maximal value consistent with current direct detection bounds. Alternatively, the calculations simplify immensely for dark matter masses large compared to all relevant nuclear masses, $m_X \gg m_N$, or dark photon masses $m_{A'}$ large compared to the characteristic momentum transfer so that the interaction is point-like. We show that none of these assumptions are valid in the regions of parameter space of greatest interest; the large m_X approximation may lead to errors of an order of magnitude for $m_X \approx 100$ GeV, and the large $m_{A'}$ approximation may also lead to mis-estimates of factors of a few for very light $m_{A'} \sim$ MeV. To accurately determine the sensitivity of experiments to probe the relevant parameter space, we carry out a general analysis, without making these simplifying assumptions. An early exploration of dark matter accumulation on the Earth mediated by massless dark photons is Ref. [30]. For previous work exploring the case of massive dark photons, see Ref. [56] for the case of dark matter capturing

in the Earth and annihilating into neutrinos, Refs. [57, 58, 59] for early work on celestial body capture of dark matter annihilating into dark photons, and in particular Ref. [60] for a description of the general framework of annihilation to light mediators that highlights the specific case of solar capture and gamma ray signatures, which were later searched for by the Fermi-LAT collaboration [61]. Finally, recent work has highlighted the effect of self-capture [62, 63] and boosted dark matter [64].

These results are timely for several reasons. Dark photons have attracted significant interest and are probed in many ways, including direct detection experiments, accelerator and beam dump experiments, and astrophysical observables [35, 36]. The signals we discuss are detectable for dark photon masses $m_{A'} \sim \mathrm{MeV} - \mathrm{GeV}$ and mixing parameters $\varepsilon \sim 10^{-10} - 10^{-8}$, an interesting and large region of parameter space that includes territory that has not yet been probed. These values of $m_{A'}$ can also produce dark matter self-interactions that have been suggested to solve small-scale structure anomalies [65, 66, 67, 68, 31]. The range of ε values are naturally induced, for example, by degenerate bi-fundamentals in grand unified theories [32]. It was recently pointed out that combining kinetic mixings of this size with the self-interacting models for small-scale structure can also explain the excess of gamma rays from the galactic center recently observed by Fermi-LAT [69].

At the same time, this work motivates a new class of searches for current indirect detection experiments to discover dark matter. At present there are a number of landmark experiments, including those mentioned above, that are transforming the field of indirect detection with high precision measurements and increasingly large statistics. In many cases, however, their sensitivities for dark matter searches are clouded by uncertainties in astrophysical backgrounds. The signals we highlight here come from a specific direction (the center of the Earth), cannot be mimicked by astrophysics and, in many cases, are essentially background-free. As a result, the processes discussed here provide an opportunity for both current and future experiments to detect a smoking-gun signal of dark matter.

2.2 Dark Photons

We consider the simplest model of dark matter interacting through dark photons. The low-energy Lagrangian is

$$\begin{aligned}\mathcal{L} &= -\frac{1}{4}\widetilde{F}_{\mu\nu}\widetilde{F}^{\mu\nu} - \frac{1}{4}\widetilde{F}'_{\mu\nu}\widetilde{F}'^{\mu\nu} + \frac{\epsilon}{2}\widetilde{F}_{\mu\nu}\widetilde{F}'^{\mu\nu} - \frac{1}{2}m^2_{\widetilde{A}'}\widetilde{A}'^2 \\ &\quad + \sum_f \bar{f}(i\partial\!\!\!/ - q_f e\widetilde{A}\!\!\!/ - m_f)f + \bar{X}(i\partial\!\!\!/ - g_X\widetilde{A}\!\!\!/' - m_X)X \ , \end{aligned} \tag{2.1}$$

where X is the Dirac fermion dark matter, and $\widetilde{A}$ and $\widetilde{A}'$ are the SM and dark sector gauge fields with field strengths $\widetilde{F}$ and $\widetilde{F}'$ and fine-structure constants $\alpha = e^2/(4\pi)$ and $\alpha_X = g_X^2/(4\pi)$, respectively. The sum is over SM fermions f with SM electric charges q_f. Dark electromagnetism is broken and the mass $m_{\widetilde{A}'}$ is generated by some mechanism, such as the Higgs or Stueckelberg mechanisms, which we assume otherwise plays a negligible role in the signals discussed here. Note that the dark matter particles X are stabilized not by some *ad hoc* discrete parity symmetry or even by dark charge conservation (which is broken), but by Lorentz symmetry, since X is the lightest fermion in the dark sector.

After diagonalizing the gauge kinetic and mass terms, the physical states are the usual massless photon A, which does not couple to X, and the dark photon A' with mass $m_{A'} = m_{\widetilde{A}'}/\sqrt{1-\epsilon^2}$, which couples both to X and to SM fermions with charge $\varepsilon q_f e$, where $\varepsilon \equiv \epsilon/\sqrt{1-\epsilon^2}$. We take the independent parameters of the theory to be

$$m_X \ , \ m_{A'} \ , \ \varepsilon \ , \ \alpha_X \ . \tag{2.2}$$

We typically fix α_X by requiring X to saturate the observed dark matter density through thermal freeze out, so $\alpha_X = \alpha_X^{\rm th} \simeq 0.035(m_X/\text{TeV})$. Alternatively, the maximum allowed coupling is set by bounds on distortions to the cosmic microwave background [70, 71, 72]. Fitting the results from Ref. [73], we find $\alpha_X^{\rm max} \simeq 0.17(m_X/\text{TeV})^{1.61}$. With a choice of α_X

the model is completely determined by the first 3 parameters.

Dark photons decay to SM fermions with width

$$\Gamma(A' \to f\bar{f}) = \frac{N_C \varepsilon^2 q_f^2 \alpha (m_{A'}^2 + 2m_f^2)}{3m_{A'}} \sqrt{1 - \frac{4m_f^2}{m_{A'}^2}} \ , \tag{2.3}$$

where N_C is the number of colors of fermion f. The dark photons we consider are produced from the annihilation of extremely non-relativistic X particles, and so have energy m_X. For $m_{A'} \gg m_e$, the dark photon decay length is therefore

$$L = R_\oplus B_e \left(\frac{3.6 \times 10^{-9}}{\varepsilon}\right)^2 \left(\frac{m_X/m_{A'}}{1000}\right) \left(\frac{\text{GeV}}{m_{A'}}\right), \tag{2.4}$$

where $R_\oplus \simeq 6370$ km is the radius of the Earth, and $B_e \equiv B(A' \to e^+e^-)$ is the branching fraction to electrons. The A' branching fractions can be determined from hadron production at e^+e^- colliders [74]. For $m_{A'} < 2m_\mu$, $B_e = 100\%$. As $m_{A'}$ increases above $2m_\mu$, the $A' \to \mu^+\mu^-$ decay mode opens up rapidly, and B_e drops to 50% at $m_{A'} \sim 300$ MeV. For 500 MeV $\lesssim m_{A'} \lesssim$ 3 GeV, B_e and B_μ are nearly identical and typically vary between 15% and 40%, with the rest made up by decays to hadrons, which also produce photons and neutrinos from meson decays. For m_X at the weak-scale and $m_{A'} \sim 100$ MeV $-$ GeV, the requirement $L \sim R_\oplus$ implies $\varepsilon \sim 10^{-10} - 10^{-8}$, and we will see that this is indeed the range of kinetic mixing parameters that gives the most promising signals.

2.3 Dark Matter Accumulation in the Earth

Dark matter interacting through dark photons is captured and annihilates at the center of the Earth. The number N_X of dark matter particles in the Earth obeys the equation

$$\frac{dN_X}{dt} = C_{\rm cap} - C_{\rm ann} N_X^2 \ , \tag{2.5}$$

where $C_{\rm cap}$ and $\Gamma_{\rm ann} = \frac{1}{2} C_{\rm ann} N_X^2$ are the rates for the capture and annihilation processes. We ignore dark matter evaporation, which is negligible for weak-scale dark matter masses [41, 42]. We also ignore self-capture from dark matter–dark matter self-interactions. The impact of self-capture for the Earth is suppressed by the fact that the escape velocity is low compared to typical galactic dark matter velocities, and so typical dark matter self-scatterings simply replace one captured dark matter particle with another [75].

The solution to Eq. (2.5) is

$$\Gamma_{\rm ann} = \frac{1}{2} C_{\rm cap} \tanh^2 \left(\frac{\tau_\oplus}{\tau} \right) \ , \tag{2.6}$$

where $\tau_\oplus \simeq 4.5$ Gyr is the age of the Earth, and $\tau = (C_{\rm cap} C_{\rm ann})^{-1/2}$ is the timescale for the competing processes of capture and annihilation to reach equilibrium. To evaluate $\Gamma_{\rm ann}$, we must therefore evaluate both $C_{\rm cap}$ and $C_{\rm ann}$, which we now do in turn.

2.3.1 Dark Matter Capture

Dark matter particles are captured when elastic scattering off nuclei N in the Earth reduces their velocity below the escape velocity. The elastic scattering process $XN \to XN$ is mediated by t-channel A' exchange. The most relevant scattering targets, N, are iron and nickel; these and other elements are listed in Table 2.1. In the center-of-mass frame, the

cross section is

$$\left.\frac{d\sigma_N}{d\Omega}\right|_{\rm CM} = \frac{1}{(E_X+E_N)^2}\frac{2\varepsilon^2\alpha_X\alpha Z_N^2}{[2\boldsymbol{p}^2(1-\cos\theta_{\rm CM})+m_{A'}^2]^2}|F_N|^2 \times \left[(E_XE_N+\boldsymbol{p}^2)^2+(E_XE_N+\boldsymbol{p}^2\cos\theta_{\rm CM})^2-(m_X^2+m_N^2)\boldsymbol{p}^2(1-\cos\theta_{\rm CM})\right] \quad (2.7)$$

where E_N, Z_N, m_N, and F_N are the energy, electric charge, mass, and nuclear form factor of target nucleus N, and $\boldsymbol{p}$ is the center-of-mass 3-momentum of the dark matter. Since the collision is non-relativistic, $\boldsymbol{p}$ is negligible everywhere in Eq. (2.7), except possibly the denominator. The cross section may then be simplified to

$$\left.\frac{d\sigma_N}{d\Omega}\right|_{\rm CM} \approx 4\varepsilon^2\alpha_X\alpha Z_N^2\frac{\mu_N^2}{(2\boldsymbol{p}^2(1-\cos\theta_{\rm CM})+m_{A'}^2)^2}|F_N|^2 \ . \quad (2.8)$$

where $\mu_N \equiv m_N m_X/(m_N+m_X)$ is the reduced mass of the X–N system.

It is tempting to simplify the denominator by neglecting $\boldsymbol{p}$, and reducing the A' exchange to a contact interaction. However, it is not always true that $m_{A'}^2 \gg \boldsymbol{p}^2$ so that the latter term may be neglected. The typical size of the momentum is $\boldsymbol{p}^2 \sim \mu_N^2 w^2$, where w is the X velocity in the lab frame. Since capture typically occurs only for very small asymptotic dark matter velocities, a reasonable choice would be $w = v_\oplus(r_N) \approx 5\times10^{-5}$, the escape velocity at the radius r_N that maximizes the radial number density $n_N(r)r^2$ of target nucleus N. With these values, the contact interaction limit fails for $m_{A'} \lesssim 3$ MeV. Rather than neglecting the momentum term altogether, a slightly more sophisticated approach would be to make the substitution $\boldsymbol{p}^2(1-\cos\theta_{\rm CM}) \to \mu_N^2 w^2$. In this work, however, we keep the full $\boldsymbol{p}$ dependence in the propagator and evaluate the capture rate numerically so that our results are valid throughout parameter space. We have confirmed that our results reproduce those in the literature in the corners of parameter space where simplifying assumptions are valid. For example, they match Ref. [76] in the large-$m_{A'}$, point-like cross section limit.

To determine capture rates, it is convenient to re-express the differential cross section as a

function of recoil energy $E_R = \mu_N^2 w^2(1-\cos\theta_{\rm CM})/m_N$ in the lab frame. In the non-relativistic limit the expression simplifies to [77]

$$\frac{d\sigma_N}{dE_R} \approx 8\pi\varepsilon^2\alpha_X\alpha Z_N^2 \frac{m_N}{w^2(2m_N E_R + m_{A'}^2)^2}|F_N|^2 \ . \tag{2.9}$$

For F_N, we adopt the Helm form factor [78],

$$|F_N(E_R)|^2 = \exp\left[-E_R/E_N\right] \ , \tag{2.10}$$

where $E_N \equiv 0.114\ \text{GeV}/A_N^{5/3}$ is a characteristic energy scale for a target nucleus with atomic mass number A_N.

From this fundamental cross section we can determine the capture rate. The differential rate of dark matter particles scattering off nuclei with incident velocity w at radius r from the center of the Earth and imparting recoil energy between E_R and $E_R + dE_R$ is given by

$$dC_{\rm cap} = n_X \sum_N n_N(r) \frac{d\sigma_N}{dE_R} w\, f_\oplus(w,r)\, d^3w\, d^3r\, dE_R \ , \tag{2.11}$$

where $n_X = (0.3\ \text{GeV/cm}^3)/m_X$ and $n_N(r)$ are the dark matter and target nucleus number densities, respectively, and $f_\oplus(w,r)$ is the velocity distribution of incident dark matter at radius r, which is distorted from the free-space Maxwell–Boltzmann distribution, $f(u)$, by the Earth's motion and gravitational potential. We follow the velocity notation introduced by Gould [43, 44, 46] where $v_\oplus(r)$ is the escape velocity at radius r and u is the dark matter velocity asymptotically far from the Earth.

The total capture rate is obtained by integrating Eq. (2.11) over the region of parameter space where the final state dark matter particle has energy less than $m_X v_\oplus^2(r)/2$ and is thus gravitationally captured. The escape velocity $v_\oplus(r)$ and number densities $n_N(r)$ are determined straightforwardly from the density data enumerated in the Preliminary Reference

Table 2.1: Mass fractions of the Earth's core and mantle for the elements most relevant for dark matter capture [80, 50]. Also shown for each element is the capture rate $C^N_{\rm cap}$ for $m_X = 1$ TeV, $m_{A'} = 1$ GeV, $\varepsilon = 10^{-8}$, and $\alpha_X = \alpha_X^{\rm th} \simeq 0.035$ as a measure of the relevance of the nuclear target for dark matter capture.

Element	Core MF	Mantle MF	$C^N_{\rm cap}({\rm s}^{-1})$	Element	Core MF	Mantle MF	$C^N_{\rm cap}({\rm s}^{-1})$
Fe	0.855	0.0626	9.43×10^7	Cr	0.009	0.0026	8.98×10^5
Ni	0.052	0.00196	7.10×10^6	O	0	0.440	4.03×10^5
Si	0.06	0.210	2.24×10^6	S	0.019	0.00025	2.41×10^5
Mg	0	0.228	1.05×10^6	Al	0	0.0235	1.62×10^5
Ca	0	0.0253	9.06×10^5	P	0.002	0.00009	2.04×10^4

Earth Model [79]. Following Edsjö and Lundberg [50], the target number densities are modeled by dividing the Earth into two layers, the core and the mantle, with constant densities and elemental compositions given in Table 2.1. The capture rate is then $C_{\rm cap} = \sum_N C^N_{\rm cap}$, where the rate on target N is

$$C^N_{\rm cap} = n_X \int_0^{R_\oplus} dr\, 4\pi r^2 n_N(r) \int_0^\infty dw\, 4\pi w^3 f_\oplus(w,r) \int_{E_{\rm min}}^{E_{\rm max}} dE_R \frac{d\sigma_N}{dE_R}\, \Theta(\Delta E)\ . \tag{2.12}$$

Here $\Theta(\Delta E) = \Theta(E_{\rm max} - E_{\rm min})$ imposes the constraint that capture is kinematically possible by enforcing that the minimum energy transfer, $E_{\rm min}$, to gravitationally capture the dark matter particle is smaller than the maximum recoil energy kinematically allowed, $E_{\rm max}$, corresponding to $\cos\theta_{\rm CM} = -1$. Explicitly, these energies are

$$E_{\rm min} = \frac{1}{2} m_X \left[w^2 - v_\oplus^2(r)\right] \qquad\qquad E_{\rm max} = \frac{2\mu_N^2}{m_N} w^2\ . \tag{2.13}$$

To make further progress, we must determine the distribution $f_\oplus(w,r)$. A simple approach is to only include the effect of the Earth's gravitational potential. However, the Earth is within the gravitational influence of the Sun, and one might expect the acceleration of dark matter by the sun to suppress or eliminate the capture of heavy dark matter particles by the Earth. In 1991, however, Gould argued that the interactions of dark matter with other

planets leads to diffusion of the dark matter population between bound and unbound orbits and one could thus ignore the impact of the Sun's gravitational field and treat the Earth in the "free-space" approximation to reasonable accuracy [81].

More recently, however, this simple picture has been refined with both potentially positive and negative implications. In numerical work, both Lundberg and Edsjö [50] and Peter [51, 52, 53] have investigated the influence of the Sun, Earth, Jupiter, and Venus in more detail, tracking the possibility that the Earth's dark matter population is suppressed when particles are kicked out of the solar system or captured by the Sun. For the case of supersymmetric WIMPs—that is, dark matter with weak-scale mediators—they have found that these effects can reduce the Earth's capture rate by one order of magnitude or more, depending on the dark matter mass. On the other hand, simulations of galaxies with baryons have shown that dark matter substructures may be pulled into the disk and create a significant and relatively cold enhancement of the local dark matter density known as a "dark disk" [82, 83]. For the case of WIMP dark matter, this population may enhance indirect detection signals from the Earth by up to three orders of magnitude [54, 84]. Note that the dark disk has a velocity relative to our solar system that is $\sim 1/5$ that of the ordinary dark matter halo [85]. It is thus plausible that the dark disk populates a region in phase space more amenable to Earth capture without significantly enhancing the direct detection rate.

As we show below, the dark photon case differs significantly from WIMPs, because both the capture and annihilation rates are highly velocity dependent. One consequence of this is that $\tau_\oplus$ is typically larger than τ in Eq. (2.6), as opposed to the conventional wisdom that the Earth has not reached its WIMP capacity. It is therefore not possible to simply extrapolate the conclusions of WIMP studies to the present framework. In addition, as our analysis is valid for general dark matter and dark photon masses, inaccuracies in the particle physics modeling are greatly reduced, and the astrophysical uncertainties from dark disk and other effects are very likely the dominant uncertainties entering the signal rate derivation. These

astrophysical phenomena are therefore clearly interesting and important, but are beyond the scope of the present work. Here, we use the free-space approximation, not because it is the last word, but because it provides a simple "middle ground" estimate, with both suppressions and enhancements possible.

With the free-space assumption, we proceed as follows. By energy conservation, w and u, the incident dark matter particle's velocities in the Earth's and galactic frame, respectively, are related by

$$w^2 = u^2 + v_\oplus^2(r) \ . \tag{2.14}$$

The capture rate for a general $d\sigma_N/dE_R$ can then be rewritten as

$$C_{\rm cap}^N = n_X \int_0^{R_\oplus} dr\, 4\pi r^2 n_N(r) \int_0^\infty du\, 4\pi u^2 f_\oplus(u) \frac{u^2 + v_\oplus^2(r)}{u} \int_{E_{\rm min}}^{E_{\rm max}} dE_R \frac{d\sigma_N}{dE_R}\, \Theta(\Delta E) \ . \tag{2.15}$$

Here $f_\oplus(u)$ is defined to be the angular-averaged and annual-averaged velocity distribution in the rest frame of the Earth [86],

$$f_\oplus(u) = \frac{1}{4} \iint_{-1}^{1} d\cos\theta\, d\cos\phi\, f\left[\left(u^2 + (V_\odot + V_\oplus \cos\gamma \cos\phi)^2 + 2u(V_\odot + V_\oplus \cos\gamma\cos\phi)\cos\theta\right)^{1/2}\right] , \tag{2.16}$$

where $V_\odot \simeq 220$ km/s is the velocity of the Sun relative to the galactic center, $V_\oplus \simeq 29.8$ km/s is the velocity of the Earth relative to the Sun, and $\cos\gamma \approx 0.51$ is the angle of inclination of the Earth's orbital plane relative to the Sun's orbit. Many-body simulations and other considerations suggest a dark matter velocity distribution in the galactic rest frame of the form [87, 88, 89, 90, 91, 92]

$$f(u) = N_0 \left[\exp\left(\frac{v_{\rm gal}^2 - u^2}{k u_0^2}\right) - 1\right]^k \Theta(v_{\rm gal} - u) \ , \tag{2.17}$$

where N_0 is a normalization constant, $v_{\rm gal}$ is the escape velocity from the galaxy, and the

parameters describing the distribution have typical values in the ranges [76, 93]

$$220 \text{ km/s} < u_0 < 270 \text{ km/s} \qquad 450 \text{ km/s} < v_{\text{gal}} < 650 \text{ km/s} \qquad 1.5 < k < 3.5 \ . \tag{2.18}$$

We use the midpoint values of each of these, namely, $u_0 = 245$ km/s, $v_{\text{gal}} = 550$ km/s, and $k = 2.5$. The truncated Maxwell–Boltzmann distribution is recovered for $k = 0$.

Upon inserting Eq. (2.9), the dE_R integral in Eq. (2.15) evaluates to

$$\int_{E_{\min}}^{E_{\max}} dE_R \frac{d\sigma_N}{dE_R} = \frac{2\pi\varepsilon^2\alpha_X\alpha Z_N^2}{w^2 m_N E_N} e^{\frac{m_{A'}^2}{2m_N E_N}} \left[\frac{e^{-x_N}}{x_N} + \text{Ei}(-x_N)\right]_{x_N^{\max}}^{x_N^{\min}} \ , \tag{2.19}$$

where we use the substitution variable x_N and exponential integral function [94],

$$x_N = \frac{2m_N E_R + m_{A'}^2}{2m_N E_N} \qquad\qquad \text{Ei}(z) \equiv -\int_{-z}^{\infty} dt \frac{e^{-t}}{t} \ . \tag{2.20}$$

The total rate is $C_{\text{cap}} = \sum C_{\text{cap}}^N = 32\pi^3\varepsilon^2\alpha_X\alpha n_X \sum_N Z_N^2 (m_N E_N)^{-1} \exp\left(\frac{m_{A'}^2}{2m_N E_N}\right) c_{\text{cap}}^N$, where

$$c_{\text{cap}}^N = \int_0^{R_\oplus} dr\, r^2 n_N(r) \int_0^{\infty} du\, u f_\oplus(u) \Theta(\Delta x_N) \left[\frac{e^{-x_N}}{x_N} + \text{Ei}(-x_N)\right]_{x_N^{\max}}^{x_N^{\min}} \ . \tag{2.21}$$

The capture rates C_{cap}^N for various nuclei N at a representative point in parameter space are shown in Table 2.1.

2.3.2 Dark Matter Annihilation

Once a dark matter particle is captured by the Earth, it repeatedly re-scatters, drops to the center of the Earth, and eventually thermalizes with the surrounding matter. In the case of the Sun, the dark matter thermalizes within the age of the Sun for X–proton spin-independent scattering cross sections greater than 10^{-51}, 10^{-50}, and 10^{-47} cm^2 for $m_X =$

100 GeV, 1 TeV, and 10 TeV, respectively [53]. Similar studies of Earth capture are not available. However, we will find that, for the range of parameters where an observable indirect signal is possible, the direct detection X–proton cross sections are at least $\sigma_p \sim 10^{-48}$ cm^2, corresponding to X–iron cross sections of $\sigma_{\rm Fe} \sim Z_{\rm Fe}^2 (m_{\rm Fe}/m_p)^2 \sigma_p \sim 10^{-42}$ cm^2, many orders of magnitude larger than required for thermalization in the Sun. We therefore expect dark matter to be thermalized in the Earth to an excellent approximation.

For thermalized dark matter, the annihilation rate parameter $C_{\rm ann}$ is [76]

$$C_{\rm ann} = \langle \sigma_{\rm ann} v \rangle \left[\frac{G_N m_X \rho_\oplus}{3 T_\oplus} \right]^{3/2} , \tag{2.22}$$

where $\rho_\oplus \approx 13$ g/cm^3 and $T_\oplus \approx 5700$ K are the matter density and temperature at the center of the Earth, respectively, $\sigma_{\rm ann}$ is the cross section for $XX \to A'A'$, and v is the relative velocity of the interacting particles, which is double the velocity of either interacting particle in the center-of-mass frame.

The thermally-averaged cross section is

$$\langle \sigma_{\rm ann} v \rangle = (\sigma_{\rm ann} v)_{\rm tree} \langle S_S \rangle , \tag{2.23}$$

where

$$(\sigma_{\rm ann} v)_{\rm tree} = \frac{\pi \alpha_X^2}{m_X^2} \frac{[1 - m_{A'}^2/m_X^2]^{3/2}}{[1 - m_{A'}^2/(2m_X^2)]^2} \tag{2.24}$$

is the tree-level cross section [95], and $\langle S_S \rangle$ is the thermal average of the S-wave Sommerfeld enhancement factor. This Sommerfeld enhancement factor [96] has been determined with various degrees of refinement. An analytic expression that includes the resonance behavior present for non-zero $m_{A'}$ can be derived by approximating the Yukawa potential by the

Hulthén potential [97, 98, 99]. The resulting Sommerfeld factor is

$$S_S = \frac{\pi}{a} \frac{\sinh(2\pi a c)}{\cosh(2\pi a c) - \cos(2\pi\sqrt{c - a^2 c^2})} \ , \tag{2.25}$$

where $a = v/(2\alpha_X)$ and $c = 6\alpha_X m_X/(\pi^2 m_{A'})$. The thermal average is, then,

$$\langle S_S \rangle = \int \frac{d^3 v}{(2\pi v_0^2)^{3/2}} \, e^{-\frac{1}{2}v^2/v_0^2} \, S_S \ , \tag{2.26}$$

where $v_0 = \sqrt{2T_\oplus/m_X}$.

2.3.3 Equilibrium Time Scales

In Fig. 2.2 we present results for the equilibrium timescale $\tau = (C_{\rm cap} C_{\rm ann})^{-1/2}$ in the $(m_{A'}, \varepsilon)$ plane for $m_X = 100$ GeV without Sommerfeld enhancement, and $m_X = 100$ GeV, 1 TeV, 10 TeV with Sommerfeld enhancement. The dark coupling α_X is fixed by the thermal relic density. For $m_{A'} \ll m_X$, the parametric dependence of τ on ε and $m_{A'}$ enters dominantly through $C_{\rm ann}$ and is $\tau \sim C_{\rm ann}^{-1/2} \sim m_{A'}^2/\varepsilon$. This can be seen in the baseline values of the contours in Fig. 2.2. The bumps in the contours reflect the resonance structure of the Sommerfeld enhancement factor $\langle S_S \rangle$.

In the shaded green (upper left) parts of the figures, the Earth's dark matter population has reached its maximal (equilibrium) value, and so the annihilation rate is essentially determined by the capture rate, with $\Gamma_{\rm ann} \approx \frac{1}{2} C_{\rm cap}$. As one moves down and to the right, however, the equilibrium timescale grows, and the population is eventually not maximal. We will see that when the population is not at its maximal value, the signal quickly becomes undetectable.

The Sommerfeld enhancement plays an essential role in reducing the equilibrium timescale and making the signal detectable in large regions of the $(m_{A'}, \varepsilon)$ plane. For capture, the typical velocity that enters has an irreducible contribution from the gravitational potential

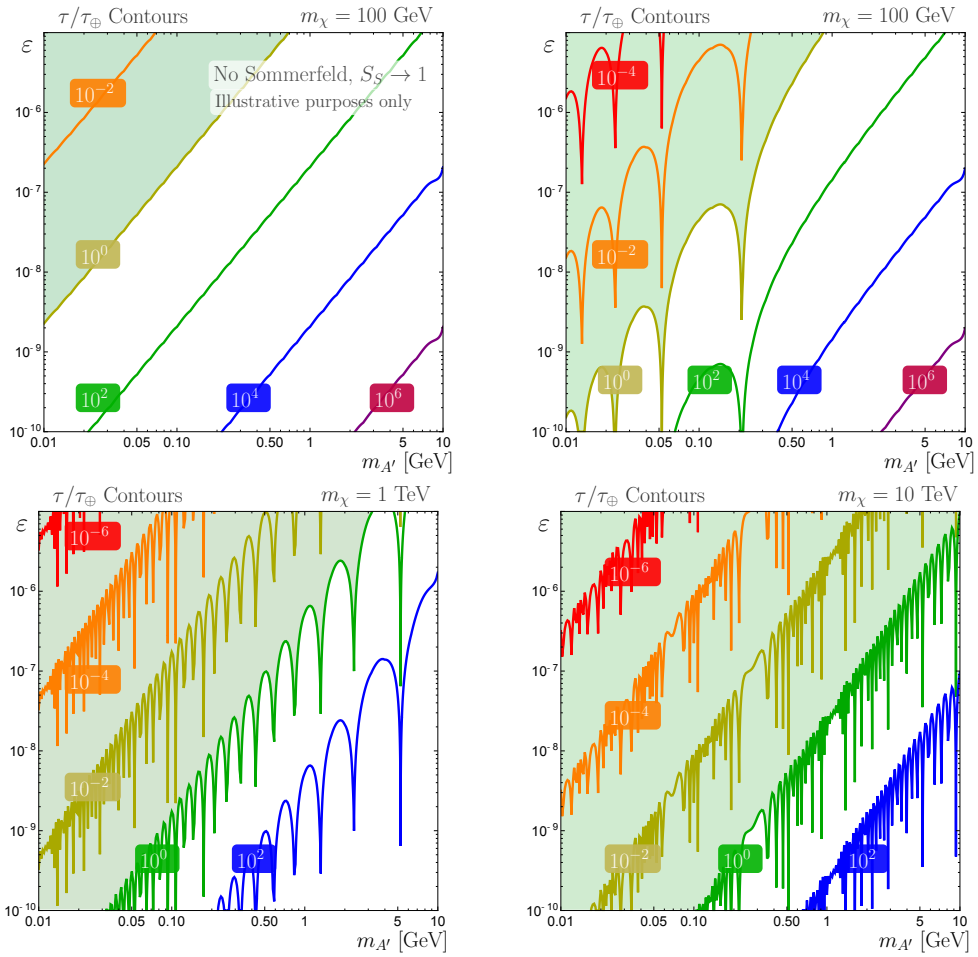

Figure 2.2: Contours of constant $\tau/\tau_\oplus$, the equilibrium timescale in units of the Earth's lifetime, in the $(m_{A'}, \varepsilon)$ plane for $m_X = 100$ GeV without (top left) and with (top right) the Sommerfeld enhancement factor, $m_X = 1$ TeV with the Sommerfeld factor (bottom left), and $m_X = 10$ TeV with the Sommerfeld factor (bottom right). The dark sector fine-structure constant α_X is set by requiring $\Omega_X \simeq 0.23$. In the green shaded regions, the Earth's lifetime is greater than the equilibrium timescale, $\tau_\oplus > \tau$.

that accelerates dark matter as it falls into the Earth. Capture interactions, therefore, occur at the typical escape velocity in the Earth's core, $v_{\rm esc} \approx 5.0 \times 10^{-5}$. However, after the dark matter particles are captured, they sink to the core, and come into thermal equilibrium with the normal matter. As a result, the population of dark matter particles at the center of the Earth is even colder, with relative velocities $v_0 \approx 1.0 \times 10^{-6}\,[\text{TeV}/m_X]^{1/2}$. In the

$m_{A'} \ll \alpha_X m_X$ limit, the Sommerfeld factor of Eq. (2.25) becomes

$$S_0 = \frac{2\pi\, \alpha_X/v}{1 - e^{-2\pi\alpha_X/v}} \ . \tag{2.27}$$

For thermal relics, S_0 is therefore typically $\sim 2\pi\alpha_X/v \sim 10^4 - 10^6$. Sommerfeld enhancement therefore reduces the equilibrium timescale by factors of ~ 100 for $m_X \sim 100$ GeV, as can be seen in Fig. 2.2 by comparing the top right and top left panels. This reduction on τ goes to ~ 1000 for $m_X \sim 10$ TeV. The Sommerfeld factor therefore plays an essential role in boosting the current Earth's dark matter population and the dark matter signal [56].

2.4 Signal Rates and Characteristics

After dark matter accumulates in the center of the Earth and annihilates to dark photons, the dark photons propagate outwards with essentially no interactions with matter. The characteristic radius of the thermalized dark matter distribution in the Earth is [76]

$$r_X = \left(\frac{3T_\oplus}{2\pi G_N \rho_\oplus m_X}\right)^{1/2} \approx 150 \text{ km}\sqrt{\frac{\text{TeV}}{m_X}} \ . \tag{2.28}$$

An observer at the surface of the Earth or in low Earth orbit therefore sees the majority of dark matter annihilations take place within $1.3^\circ\sqrt{\text{TeV}/m_X}$ of straight down.

The dark photons are highly boosted with energy m_X. In the decay $A' \to f\bar{f}$, the characteristic angle between the direction of a parent A' and its decay products in the Earth's rest frame is

$$\theta \sim \tan^{-1}\left(\frac{m_{A'}^2 - 4m_f^2}{m_X^2 - m_{A'}^2}\right)^{1/2} \approx \frac{\sqrt{m_{A'}^2 - 4m_f^2}}{m_X} \ , \tag{2.29}$$

assuming $m_{A'} \ll m_X$. Much larger opening angles are possible, however, as discussed in detail in the Appendix.

The indirect detection signal is therefore two highly collimated leptons or jets that point back to the center of the Earth within a few degrees. As we will discuss, in some cases, the two leptons or jets may be simultaneously detected, and possibly even seen as two different particles, in contrast to the standard neutrino-based indirect detection signals, where there is only one primary particle. In any case, the signal of high-energy particles from the center of the Earth distinguishes the signal from all possible astrophysical backgrounds, potentially providing a smoking-gun signal of dark matter if the event rates are large enough.

We now determine the event rates and characteristics for two classes of experiments: under-ice/underground/underwater detectors, represented by IceCube, and space-based experiments, represented by Fermi-LAT and AMS-02.

2.4.1 IceCube

Dark photons may be detected in IceCube if they decay in IceCube or just below it. Decays $A' \to e^+e^-, q\bar{q}$ will be seen as showers, and for $m_{A'} \gtrsim 300$ MeV, typically 15% – 40% of the decays will be to muons [74] and be seen as tracks. The number of dark photon decays that can be detected by IceCube is

$$N_{\rm sig} = 2\,\Gamma_{\rm ann}\,\frac{A_{\rm eff}}{4\pi R_\oplus^2}\,\epsilon_{\rm decay}\,T\ , \tag{2.30}$$

where the factor of 2 results from the fact that each annihilation produces two dark photons, $A_{\rm eff}$ is the effective area of detector,

$$\epsilon_{\rm decay} = e^{-R_\oplus/L} - e^{-(R_\oplus+D)/L} \tag{2.31}$$

is the probability that the dark photon decays after traveling a distance between $R_\oplus$ and $R_\oplus + D$, where D is the effective depth of the detector, and T is the live time of the

experiment.

To very roughly estimate the detection rates for IceCube, we expect that for $m_X \sim 1$ TeV, all dark photons that decay within the instrumented volume of IceCube are detected, and so we take $A_{\rm eff} \approx 1$ km^2 and $D \approx 1$ km. For lighter dark matter, say, $m_X \sim 100$ GeV, the decay products may be lost between the photomultiplier strings of IceCube. But these should be seen with high efficiency in DeepCore [100], the subset of IceCube with finer string spacings and lower threshold, and so we also present results for the instrumented volume of DeepCore, with $A_{\rm eff} \approx 0.067$ km^2 and $D \approx 0.55$ km.

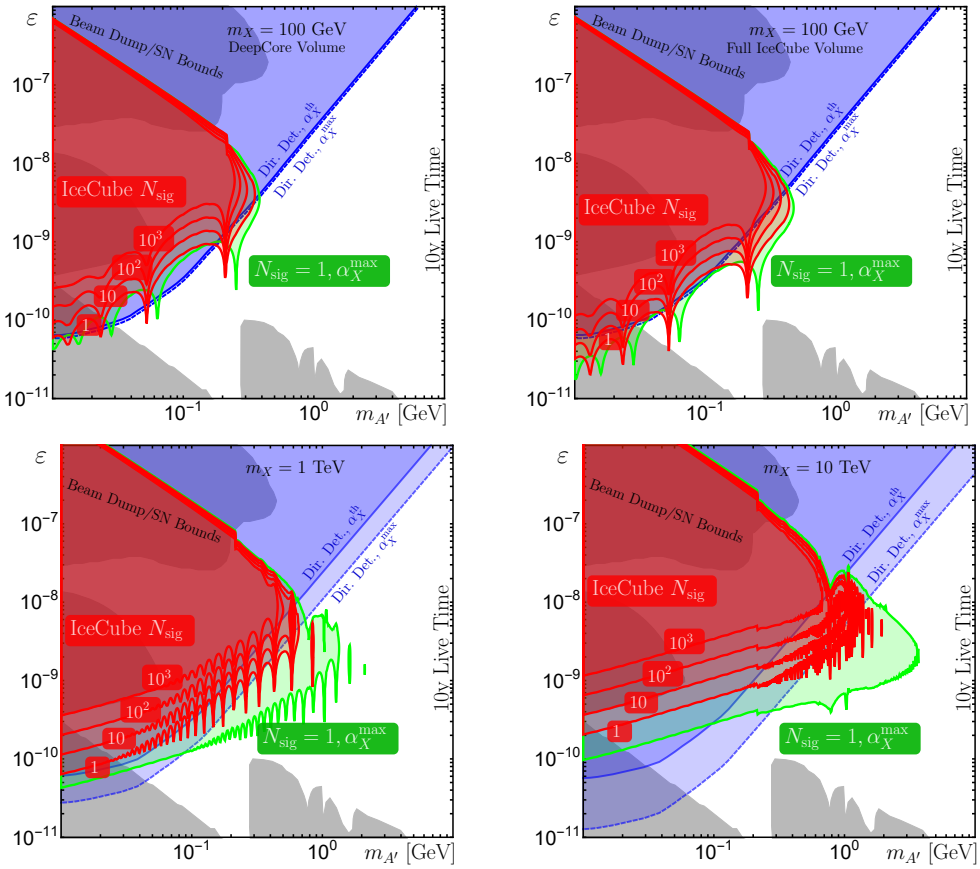

Figure 2.3: **Red:** IceCube event rates for $T = 10$ years live time in the $(m_{A'}, \varepsilon)$ plane for $m_X = 100$ GeV in DeepCore (top left) and IceCube (top right), $m_X = 1$ TeV in IceCube (bottom left), and $m_X = 10$ TeV in IceCube (bottom right). The dark sector fine-structure constant is set to the value $\alpha_X^{\rm th}$ which realizes $\Omega_X \simeq 0.23$. **Green:** Single event reach for the maximal dark fine-structure constant $\alpha_X^{\rm max}$ allowed by cosmic microwave background distortion bounds [73]. **Blue:** current bounds from direct detection [101]. **Gray:** regions probed by beam dump and supernovae constraints [102, 103, 35, 104, 105].

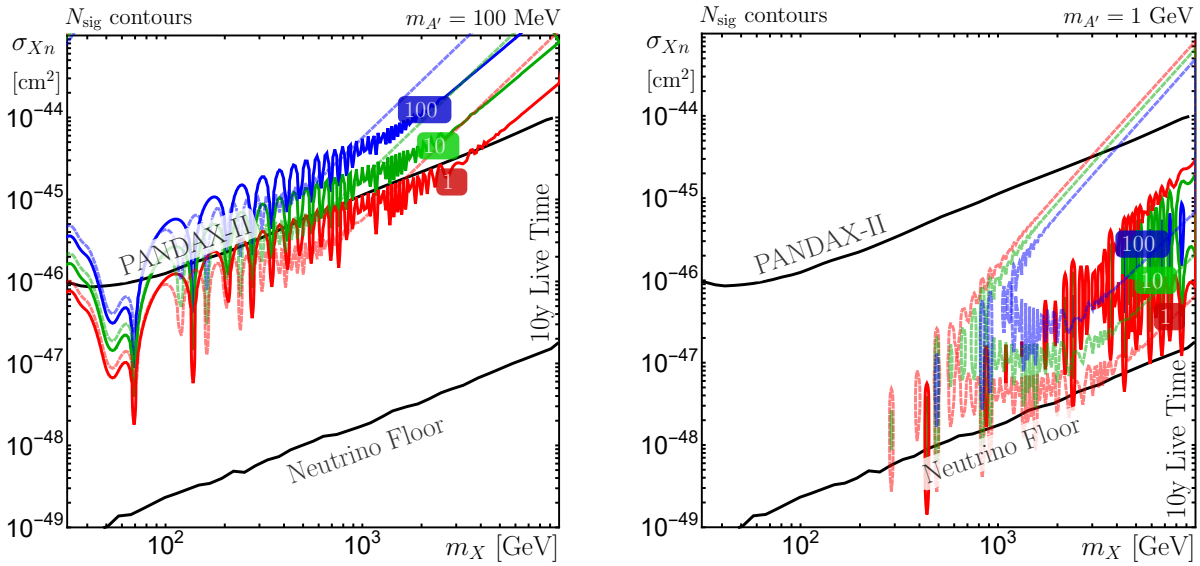

Figure 2.4: Comparison of indirect and direct detection sensitivities in the (m_X, σ_{Xn}) plane for $m_{A'} = 100$ MeV (left) and 1 GeV (right). The direct detection bounds are from the LUX collaboration [108]. In this regime the interaction is effective point-like in contrast to the low $m_{A'}$ region [109, 110, 101] in Fig. 2.3, where the direct detection bounds become independent of $m_{A'}$ for low $m_{A'}$. Also shown is the 'neutrino floor,' where coherent neutrino scattering affects direct detection experiments [111]; the dashed line is an extrapolation.

In Fig. 2.3 we present the number of signal events for $m_X = 100$ GeV, 1 TeV, and 10 TeV in the $(m_{A'}, \varepsilon)$ plane. The bumpy features and closed contours are real physical features resulting from Sommerfeld enhancement resonances. Also shown are the regions of parameter space disfavored by existing bounds on dark-photon-mediated $XN \to XN$ scattering from direct detection experiments, such as PANDAX-II [101, 106], and X-independent bounds on dark photons from beam dump experiments and supernovae [102, 103, 35, 104, 105, 107]. We use the recently updated supernova cooling bounds in Ref. [107].

We see that the indirect detection signal discussed here probes regions of parameter space that are so far inaccessible by other methods. As anticipated in Sec. 2.2, the indirect detection signal is largest for $\varepsilon \sim 10^{-10} - 10^{-8}$, where the A' decay length is comparable to $R_\oplus$. For $m_X \sim 10$ TeV and $\varepsilon \sim 10^{-8}$, for example, $N_{\rm sig} \sim 1,000$ events over 10 years are possible in regions of parameter space that are otherwise currently viable. IceCube has collected roughly 7 years of data already, and so detailed analyses will either exclude large new regions of the

$(m_{A'}, \varepsilon)$ parameter space or discover dark matter.

For $m_X \sim 100$ GeV, the indirect and direct detection sensitivities are comparable for α_X between $\alpha_X^{\rm th}$ and $\alpha_X^{\rm max}$. The indirect and direct detection sensitivities are shown in the conventional (m_X, σ_{Xn}) plane in Fig. 2.4, where σ_{Xn} is the spin-independent X–nucleon cross section: $\mu_T^2 A_T^2 \sigma_{Xn} = \mu_n^2 \sigma_{XT}$ with $T = \text{Xe}$. The indirect detection signal is suppressed for both large σ_{Xn} (large ε, dark photons decay too soon) and small σ_{Xn} (small ε, dark matter capture is too slow and the captive population does not equilibrate). Of course, the large σ_{Xn} are already excluded by direct detection experiments. Focusing on the small σ_{Xn} region, for $m_X > 100$ GeV, the indirect detection signals probe cross sections as much as three orders of magnitude below the current bounds from direct detection experiments, such as XENON and LUX.

Since $\sigma_{Xn} \sim \alpha_X \varepsilon^2$, a given σ_{Xn} corresponds to a larger value of ε when assuming the thermal $\alpha_X^{\rm th}$ versus maximal $\alpha_X^{\rm max}$ dark sector coupling. For this reason, the dashed $\alpha_X^{\rm max}$ curves on the left-hand plot in Fig. 2.4 are sometimes above the solid $\alpha_X^{\rm th}$ curves on the (m_X, σ_{Xn}) plane. This is because when going from $\alpha_X^{\rm th}$ to $\alpha_X^{\rm max}$, the additional ε reach gained in indirect detection experiments is less than that in direct detection experiments. The reason for this is straightforward: the lower bound on the IceCube reach is set by the condition that the $\tanh^2(\tau_\oplus/\tau)$ in Eq. (2.6) is 'saturated' near unity, i.e. that dark matter capture and annihilation are in equilibrium. This is why the lower contours of Fig. 2.3 display the same resonances as Fig. 2.2. Since this condition is set by the geometric mean of the capture and annihilation rates, it scales differently from direct detection experiments which has the same parametric dependence as the capture rate.

The detector's effective area $A_{\rm eff}$ and depth D are, of course, dependent on the energy and type of the dark photon decay products, and a more detailed study of detector response is required to estimate these more accurately. This is beyond the scope of the present work, but we note here some basic considerations. Muons with energies $E_\mu \sim 100$ GeV $-$ TeV lose

energy primarily through ionization and travel a distance

$$L_\mu = \frac{1}{\rho\beta} \ln \left[\frac{\alpha + \beta E_\mu}{\alpha + \beta E_{\rm th}} \right] \tag{2.32}$$

before their energy drops below a threshold energy $E_{\rm th}$, where $\rho = 1$ g/cm^3, $\alpha \simeq 2.0$ MeV cm^2/g, and $\beta \simeq 4.2 \times 10^{-6}$ cm^2/g [112]. For $E_\mu = 1$ TeV and $E_{\rm th} = 50$ GeV, on average muons travel a distance $L_\mu = 2.5$ km. Dark photons that decay to muons a km or two below IceCube may therefore be detected in IceCube, and so the effective depth of IceCube is a bit larger than 1 km. For $m_X \sim 10$ TeV, the effective depth is larger still, although less than a naive application of Eq. (2.32) would indicate, as such high energy muons lose energy primarily through radiative processes. At TeV energies, the experimental angular resolution for muon tracks is less than a degree, providing a powerful handle to reduce background. For the case of showers from electrons or hadrons, the angular resolution is worse, but still sufficient to identify showers as up-going to within tens of degrees. In addition, because dark photons decay completely to visible particles, contained events are mono-energetic, with the total energy equal to m_X. The angle and energy distributions of tracks and showers are therefore completely different from astrophysical sources, and provide powerful handles for differentiating signal from background.

The dark photon signal has two primaries, which could in principle be identified as a smoking-gun signal for the dark sector. In Figs. 2.5 and 2.6 we show histograms of the velocity difference (time delay) and opening angle (track separation) of the two muons produced in a dark photon decay. Details of the distributions are presented in the Appendix. Parallel tracks have been considered previously in the context of slepton production from high energy neutrinos in Refs. [113, 114] and have recently been searched for by IceCube [115]. As a benchmark for IceCube reach, the parameters $m_X = 1$ TeV, $m_{A'} = 500$ MeV, and $\varepsilon = 5 \times 10^{-9}$ gives an expected 40 muon events in 10 live years. The center panels of Figs. 2.5 and 2.6 then show that over ~ 2.5 km between the A' decay point and the maximal detection

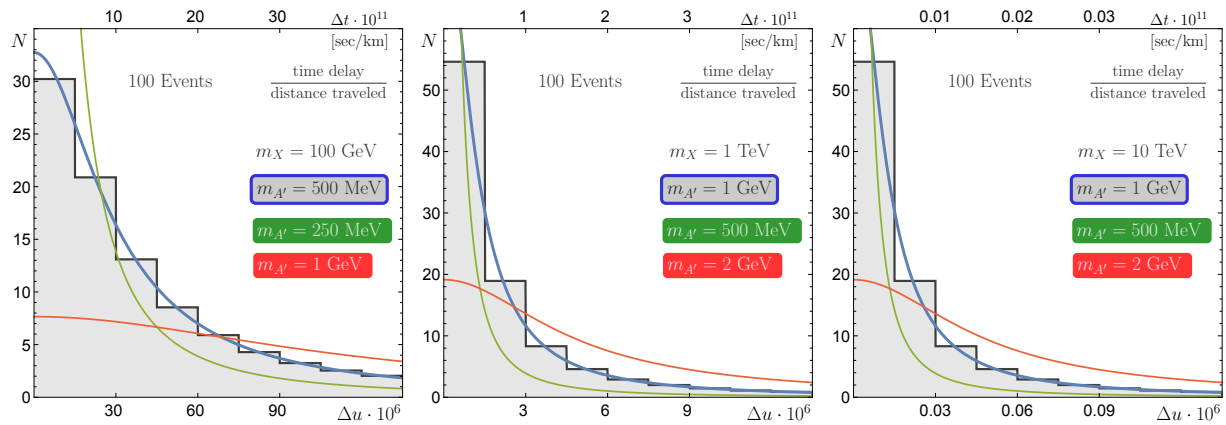

Figure 2.5: Lab-frame muon velocity differences for $A' \to \mu^+\mu^-$ and $(m_X, m_{A'}) = (100$ GeV, 500 MeV) (left), (1 TeV, 1 GeV) (center), and (10 TeV, 1 GeV) (right). Distributions are normalized to 100 events and different values of $m_{A'}$ are shown for comparison. The top axes measure the time delay between the two final states per km between the decay and observation positions.

distance, one expects a few events with timing separation of ~ 0.03 ns and ~ 20 m track separation.

The timing separation is below the IceCube Digital Optical Module timing resolution of ~ 5 ns [116]. The track separations are less than the ~ 100 m separations probed by current analyses [115], but they are also much larger than the ~ 1 m separations from SM neutrino-induced charm production. These results motivate looking for parallel muon tracks with $\mathcal{O}(10\text{ m})$ separations, which would be an unambiguous signal of physics beyond the SM, and a spectacular signal of dark photons and dark matter. One step in this direction is the proposed PINGU upgrade which would densely instrument a subset of the IceCube/DeepCore detector [117]. However, for the proposed dark photon search, this comes at a large cost in available volume and propagation distance. A possible alternative direction to improve sensitivity to these parallel muon signals is to increase the detector density of the IceTop surface array.

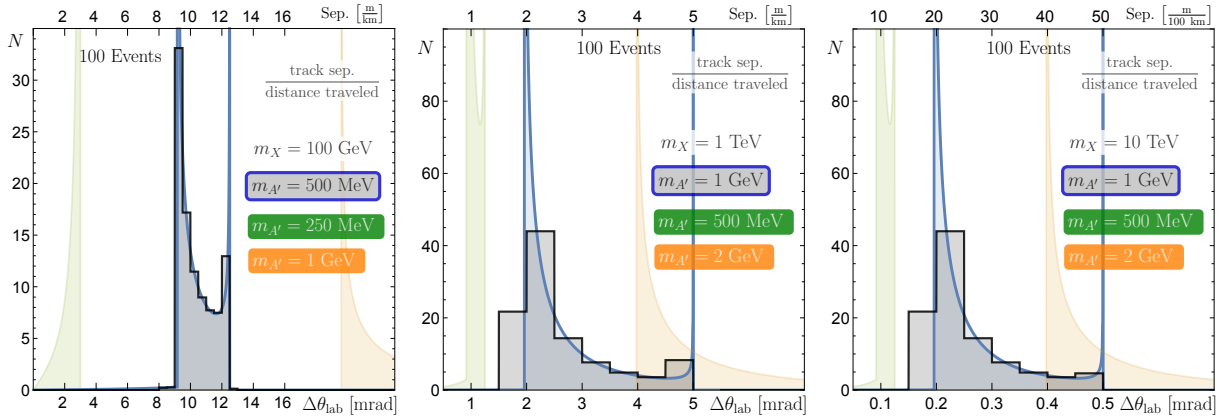

Figure 2.6: Lab-frame muon opening angles (bottom axis)/track separation (top axis) for $A' \to \mu^+\mu^-$ and the same m_X values as Fig. 2.5. Different values of $m_{A'}$ are shown for comparison.

2.4.2 Fermi-LAT/AMS-02

The dark photon decay products may also be detected by space-based cosmic ray detectors, such as Fermi-LAT and AMS-02. Though these are far smaller than IceCube, the dark photon may decay anywhere between the Earth's surface and the detector, providing a partially-compensating enhancement to the rate. For Fermi and AMS, we follow the formalism described above, but now use $A_{\rm eff} = 1$ m^2. Both Fermi and AMS are in low Earth orbit, flying 550 and 400 km above the ground, respectively. We choose $D = 550$ km in Eq. (2.31). Note that, after the dark photon decays, the resulting charged particles are bent in the Earth's magnetic field by an angle

$$\theta = 0.5^\circ \frac{\text{TeV}}{p} \frac{L}{550 \text{ km}} \frac{B}{0.5 \text{ G}} , \tag{2.33}$$

where p is the particle's momentum, L is the distance it travels, and we have normalized the Earth's magnetic field B to an average value at the surface of the Earth. For $m_X \gtrsim$ TeV, this deflection is less than the dispersion from the dark matter's spatial distribution at the center of the Earth given in Eq. (2.28), but for $m_X \sim 100$ GeV, this deflection may be significant, and the signal may arrive at an angle as large as 5° relative to straight down.

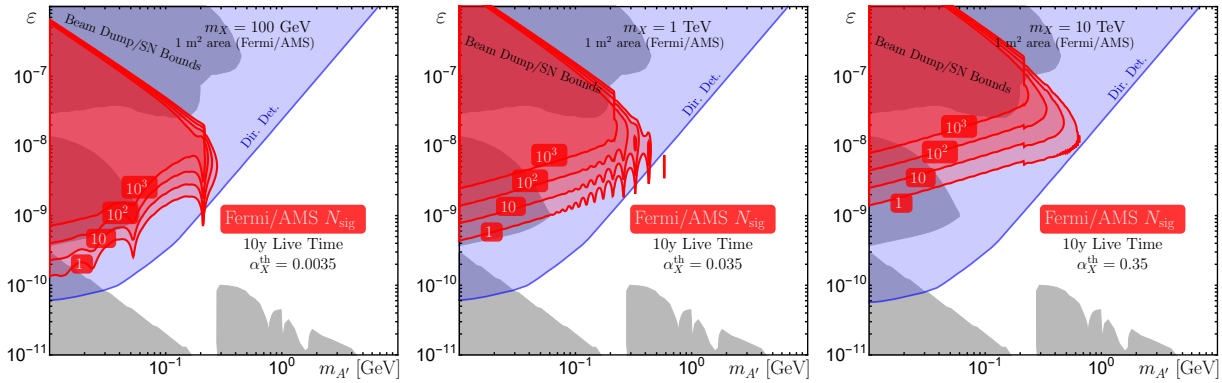

Figure 2.7: 10 year signal event rates for a space-based detector in low Earth orbit, such as Fermi/AMS. Colors and bounds are the same as Fig. 2.3.

The resulting event rates for such space-based detectors are given in Fig. 2.7 for a live time of 10 years. The parameter space that can be probed largely overlaps with that already probed by direct detection, but Fermi and AMS may set bounds complementary to the existing direct detection experiments. As a benchmark, consider the parameters $m_X = 1$ TeV, $m_{A'} = 400$ MeV, and $\varepsilon = 10^{-8}$, for which one expects $N_{\rm sig} = 10$ signal events in 10 live years. The velocity difference and opening angle distributions are shown in the center panels of Figs. 2.5 and 2.6. For a primary propagation distance of ~ 300 km, this yields timing separations of up to tens of nanoseconds and separations of up to a kilometer. We therefore do not expect to see both primary particles from dark photon decay in Fermi or AMS. Of course, this is still possible: the A' may decay near Fermi or AMS; secondary photons from hadronic final states my happen to have little transverse momentum; or the A' may decay far from the detectors to two charged particles, which are both bent by the magnetic field into the detectors. Although possible, all of these are highly improbable, and two-particle events are a small fraction of the total number of single-particle signal events. An alternative possibility is when there is a small splitting between $m_{A'}$ and $2m_f$. In this case the decay products have small transverse momentum by Eq. (2.29), at the cost of a reduced branching ratio.

Last, the number of signal events $N_{\rm sig}$ does not take into account experimental efficiencies associated with each apparatus. For example, we have assumed that the volume of the

International Space Station between the Earth and AMS does not affect the dark photon primaries, and, further, that the hadronic products of the dark photons are detectable. A more complete analysis of the Fermi/AMS reach will require more realistic modeling and different triggers.

2.5 Conclusions

We have presented a novel method to discover dark matter that interacts with the known particles through dark photons that kinetically mix with the SM photon. The dark matter is captured by the Earth and thermalized in the Earth's center, and then annihilates to dark photons. The dark photons then travel to near the surface of the Earth and decay. We have determined the signal rates without simplifying assumptions concerning the dark matter and dark photon masses. In viable regions of the model parameter space, thousands of such dark photon decays are possible in IceCube, and smaller, but still detectable, signals in space-based detectors such as Fermi and AMS are also possible.

As with traditional indirect detection signals that rely on annihilation to neutrinos, the dark photon signal points back to the center of the Earth, differentiating it from astrophysical backgrounds. In contrast to the neutrino signal, however, the dark photon decays to two visible particles. The dark photon signal is therefore even more striking, as it is monoenergetic if fully contained. In addition, in principle both particles could be detected simultaneously yielding, for example, parallel muon tracks in IceCube with separations of $\sim \mathcal{O}(10\text{ m})$. We have shown distributions of these separations for representative points in model parameter space.

As discussed in Sec. 2.3.1, the leading uncertainty in the signal rate predictions is from the capture rate analysis. The escape velocity of the Earth is not large, and so this capture rate

is subject to detailed modeling, including the effects of the Earth, Sun, Jupiter, and Venus. In addition, a cold "dark disk" population of dark matter may significantly enhance the capture rates. The implications of these effects for WIMP dark matter have been considered in Refs. [50, 51, 52, 53, 54, 84]; it would be interesting to determine their effects on dark matter with dark photon-mediated interactions.

In this study, we have assumed the dark matter X is a Dirac fermion and the mediator is a dark photon that mixes only with the SM photon, and so couples only to charged particles. It would be interesting to consider cases where X is a pseudo-Dirac fermion or a scalar, and cases where the dark photon mixes with the Z (and so couples to neutrinos, for example), or is replaced by a scalar (for which the dark matter may also be Majorana). Dark matter that collects and annihilates at the center of the Sun is also a promising source of decaying dark photons and will probe different regions of parameter space [6].

Finally, the experiments have been modeled very roughly here; detailed analyses, preferably by the experimental collaborations themselves, are required to evaluate the accuracy of the signal rate estimates. However, our conclusion that there are viable regions of parameter space that predict thousands of signal events indicates that there are certainly regions of parameter space where the indirect detection signals discussed here are the most sensitive probes, surpassing direct detection detectors, beam dump experiments, and cosmological probes. The possibility of discovering signals of dark matter that, unlike so many other indirect detection signals, are essentially free of difficult-to-quantify astrophysical backgrounds, provides a strong motivation for these searches.

Chapter 3

Dark Photons from the Center of the Sun

The following is based on a previously published paper by the author, Jonathan L. Feng, and Philip Tanedo [6].

3.1 Introduction

As previously discussed, the kinetic mixing portal predicts a novel class of indirect detection signals. In this framework, dark matter is captured by large gravitating bodies and annihilates into dark photons. The decay products of these dark photons can be detected if they escape the gravitating object. The formalism for dark matter capture and annihilation was developed many years ago for the case of dark matter annihilating in the Sun or Earth to neutrinos [37, 38, 39, 40, 41, 42, 43, 44, 45, 46]. In the past few years, studies have begun to explore the case of annihilation into new, light SM singlet particles [60], including the specific case of dark photons [57, 58, 59].

In Ref. [7], we carried out a detailed examination of dark matter annihilating to dark photons in the center of the Earth. We found that this could result in spectacular signals in the IceCube Neutrino Observatory and possibly also space-based detectors such as the Fermi Large Area Telescope (LAT) and the Alpha Magnetic Spectrometer (AMS). As an example, in currently unconstrained regions of parameter space with dark matter masses 100 GeV $\lesssim m_X \lesssim$ 10 TeV, dark photon masses $m_{A'} \sim$ MeV $-$ GeV, and kinetic mixing parameters $10^{-10} \lesssim \varepsilon \lesssim 10^{-8}$, this scenario predicts up to thousands of TeV-energy e^+/e^-, μ^+/μ^-, and hadron pairs from the center of the Earth streaming through the IceCube detector each year. Experimental searches for this signal will therefore either exclude new regions of parameter space or provide the first unambiguous signal of dark matter. Additionally, in contrast to the standard case of indirect detection of neutrinos, in the dark photon case, all of the annihilation products from a single dark matter particle can be detected, allowing one to reconstruct the dark matter mass from a few clean signal events.

In this work we examine the complementary possibility that dark matter accumulates not in the Earth, but in the Sun, annihilating to dark photons ("dark sunshine") which decays to SM particles. The complete process is shown schematically in Fig. 3.1.

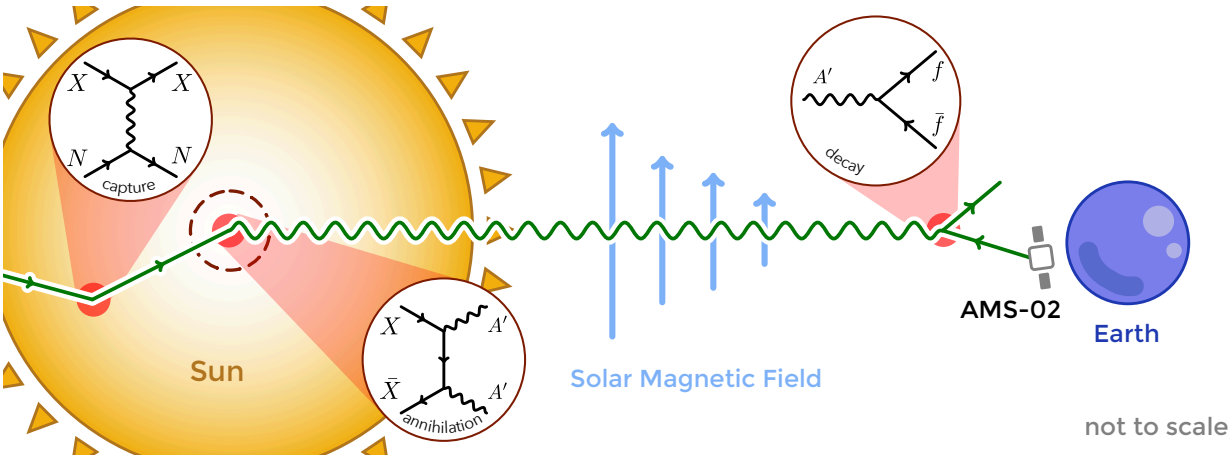

Figure 3.1: Dark matter is captured by elastic $XN \to XN$ scattering off nuclei, collects in the center of the Sun, and annihilates to dark photons, $XX \to A'A'$. These dark photons then leave the Sun and decay to SM particles, including positrons that may be detected by the Alpha Magnetic Spectrometer on the International Space Station.

At first sight, replacing the Earth with the Sun may appear to be a simple substitution, but this is far from the case. There are some obvious differences: the longer propagation distance required for dark photons to escape the Sun compared to the Earth implies that searches for solar dark photons probe smaller kinetic mixing parameters ε. In addition, the Sun's size provides more targets and a bigger gravitational potential to assist dark matter capture, and the solar capture rate is more reliably calculated than the Earth's. There is also a very significant new complication, however: for dark photons from the Sun, the magnetic fields of the Sun and Earth deflect the dark photon decay products, potentially ruining the directionality of the signal. Cuts to define the signal region and optimize the signal above background must, therefore, be very carefully defined.

In this work, we perform a complete, systematic analysis of solar capture of dark matter and its subsequent annihilation into dark photons. We go beyond prior analyses by including the effect of non-perturbative Sommerfeld enhancements of the annihilation rate. We also consider self-capture in the Sun [75], which we find to be a subleading effect in the regions of parameter space with significant event rates. In addition, we model the effect of the solar magnetic field on the signal. We focus on the reach of AMS-02 to detect the signal in positrons and optimize the signal over background by defining stringent cuts to reduce the

background to almost negligible levels. The analysis makes essential use of AMS's excellent angular resolution [118], which has not previously been utilized in its dark matter searches.

Including these effects, we show that AMS can discover dark matter through the dark sunshine signal for parameters 100 GeV $\lesssim m_X \lesssim$ 10 TeV, $m_{A'} \sim \mathcal{O}(100)$ MeV, and $10^{-10} \lesssim \varepsilon \lesssim 10^{-8}$. The signal probes a region in parameter space that is unconstrained by beam dump and supernova bounds. This region is also probed by direct detection, and so this suggested search provides a complementary probe. Such values of ε are naturally induced, for example, by degenerate bi-fundamentals in grand unified theories [32]. These values of $m_{A'}$ and ε also produce dark matter self-interactions that have been suggested to solve small scale structure anomalies [31] and may simultaneously explain the excess of gamma rays from the galactic center recently observed by the Fermi Large Area Telescope [69].

The Fermi-LAT collaboration has set investigated the possibility of dark matter captured in the Sun annihilating into on-shell mediators [61]. The approach taken there was to use light mediators as a general motivation for searches for asymmetries, for example, for an excess of positrons from the hemisphere including the Sun over the opposite hemisphere. This study is complementary to that work in that we maximize the search reach by defining more stringent cuts that reduce the background to near-negligible levels. In addition, we consider the dark photon mediator specifically, determine the reach in this model's parameter space, and compare it to the reach of other experimental and observational constraints.

3.2 Dark Matter Interactions Through a Dark Photon

The dark photon A' is the gauge boson of a broken U(1) symmetry that kinetically mixes with the hypercharge boson. The diagonalization of the Hamiltonian from the kinetically mixed gauge–basis states to physical states is detailed in the Appendix. When the dark

photon mass is very light, the mixing with the Z boson is negligible and this system may be treated as a mixing between the photon and the dark photon. The effective Lagrangian for the photon–dark photon system is

$$\mathcal{L} = -\frac{1}{4}F_{\mu\nu}F^{\mu\nu} - \frac{1}{4}F'_{\mu\nu}F'^{\mu\nu} + \frac{1}{2}m_{A'}^2 A'^2 - \sum_f q_f e(A_\mu + \varepsilon A'_\mu)\bar{f}\gamma^\mu f - g_X A'_\mu \bar{X}\gamma^\mu X \ , \quad (3.1)$$

where we sum over SM fermions f with electric charge q_f, ε is the kinetic mixing parameter in the physical basis, and g_X is the dark U(1) gauge coupling. We present our results in terms of the electromagnetic and dark fine structure constants, $\alpha = e^2/(4\pi)$ and $\alpha_X = g_X^2/(4\pi)$.

In the limit where $m_X \gg m_{A'} \gg m_e$, the dark photon decay length is

$$L = R_\odot \, \mathrm{Br}(A' \to e^+e^-) \left(\frac{1.1 \times 10^{-9}}{\varepsilon}\right)^2 \left(\frac{m_X/m_{A'}}{1000}\right) \left(\frac{100 \text{ MeV}}{m_{A'}}\right), \quad (3.2)$$

where $R_\odot = 7.0 \times 10^{10}$ cm $= 4.6 \times 10^{-3}$ au is the radius of the Sun, and the branching ratio to e^+e^- can be determined from hadron production at colliders and is between 40% and 100% for the range 1 MeV $\lesssim m_{A'} \lesssim$ 500 MeV [74].

We consider two choices for the dark photon couplings. First, we consider the case where the present dark matter abundance is set by thermal freeze out with respect to the annihilation process $X\bar{X} \to A'A'$. The Born approximation cross section valid at freeze out is [95]

$$\langle \sigma_{\text{ann}} v \rangle^{\text{Born}} = \frac{\pi \alpha_X^2}{m_X^2} \frac{\left(1 - m_{A'}^2/m_X^2\right)^{3/2}}{\left[1 - m_{A'}^2/(2m_X^2)\right]^2} \ . \quad (3.3)$$

Obtaining the observed $\Omega_X h^2 = 0.12$ from thermal freeze out requires $\langle \sigma_{\text{ann}} v \rangle = 2.2 \times 10^{-26}$ cm^3/s [119], so that

$$\alpha_X^{\text{th}} = 0.035 \left(\frac{m_X}{\text{TeV}}\right) \ . \quad (3.4)$$

Alternatively, one may assume that the dark matter abundance is set by non-thermal dynamics and allow α_X to take its maximal experimentally-allowed value. The most stringent bounds come from the imprint of dark matter annihilation products on the cosmic microwave background (CMB) [70, 71, 72, 73]. We fit the results of Ref. [73] and find that the maximum coupling allowed by the CMB is

$$\alpha_X^{\max} = 0.17 \left(\frac{m_X}{\text{TeV}}\right)^{1.61} \tag{3.5}$$

in the range of phenomenologically relevant masses.

3.3 Experimental Bounds on Dark Photon Mediators

Here we briefly review the bounds on dark photons that are most relevant in the parameter space relevant to this work.

3.3.1 Direct Detection

Direct detection experiments bound dark photon mediated interactions with weak-scale dark matter. These were recently examined in Ref. [101], which highlighted that the exclusion contour in the (m_A, ε) plane becomes independent of m_X for small m_A when the contact-interaction limit breaks down. This is easy to understand: in the $m_A \ll m_X$ limit, the X–nucleon cross section and annihilation rate scale as

$$\sigma_{Xn} \sim \alpha_X \rho_0 \sim \frac{\alpha_X}{m_X} \qquad\qquad \langle \sigma_{\text{ann}} v \rangle \sim \frac{\alpha_X^2}{m_X^2} \ . \tag{3.6}$$

Fixing α_X to yield the thermal relic cross section $\langle \sigma_{\text{ann}} v \rangle = 2.2 \times 10^{-26}$ cm^3/s gives $\alpha_X \sim m_X$, and so the direct detection bounds are constant in m_X for a thermal relic.

3.3.2 Colliders and Fixed-Target Experiments

Direct searches for dark photons production at colliders and beam dump experiments are reviewed in Ref. [35]. These searches do not make use of the dark photon–dark matter coupling and can thus be plotted in the $(m_{A'}, \varepsilon)$ plane independently of the dark matter mass. In the mass range probed by this study, MeV $< \mathrm{m}_{A'} <$ GeV and $10^{-12} < \varepsilon < 10^{-7}$, the most relevant bounds are from the E137 beam dump experiment [120, 121], the LSND neutrino experiment [122, 123, 124], and the CHARM fixed target experiment [125, 126]. For the dark matter mass range where AMS is sensitive to solar dark photons, these collider experiments are less sensitive than the direct detection bounds from LUX presented in Ref. [101].

3.3.3 Indirect Detection

Bounds on dark matter annihilation into dark photons in the present day coming from the diffuse positron spectrum constrain the dark sector coupling, α_X [59, 57, 60]. These bounds do not reach the thermal coupling and are weaker than the CMB bounds that define our maximal coupling in Eq. (3.4).

3.3.4 Supernova Bounds

Independent of the dark matter properties, light mediators are constrained by the cooling of supernova by mediator emission [102, 103, 35, 104, 105, 107]. In particular, Ref. [107] recently refined the analysis of supernova cooling and found that the bounds on dark photons are nearly an order of magnitude weaker than previously published limits. Separately, the absence of a prompt MeV γ-ray signal from supernova 1987A sets additional bounds on the $(\varepsilon, m_{A'})$ plane [104]. Ref. [127] pointed out that dark matter interactions may weaken these bounds when the dark matter is light ($m_X \lesssim$ GeV).

3.3.5 Cosmology

The cosmic microwave background sets bounds on dark matter annihilation products in the early universe [70, 71, 72]. In addition to the CMB bounds from Ref. [73] that set the maximum phenomenologically allowed α_X in Eq. (3.5), the impact of late dark photon decays on big bang nucleosynthesis and the CMB constrains the $(m_{A'}, \varepsilon)$ plane for $m_{A'} \lesssim$ GeV [128].

3.4 Dark Matter Accumulation in the Sun

Similar to capture in the Earth, dark matter is captured in the Sun if elastic collisions with solar nuclei transfer enough energy that the dark matter's velocity falls below the Sun's escape velocity. Dark matter may also be self-captured by scattering off of already-captured dark matter [75]. The captured dark matter accumulates in the solar core and thermalizes. This accumulation is balanced by annihilation into pairs of dark photons. Due to the low temperature at the core of the Sun, this annihilation rate is Sommerfeld enhanced from dark photon-mediated interactions at low relative velocity.

The number of dark matter particles in the Sun, N_X, satisfies the rate equation

$$\dot{N}_X = C_{\text{cap}} + C_{\text{self}} N_X - C_{\text{ann}} N_X^2 \ , \tag{3.7}$$

where the C coefficients encode the capture rate, self-capture rate, and annihilation rate. We ignore the effect of dark matter evaporation, which is negligible for dark matter masses above $\mathcal{O}(10)$ GeV [41, 42]. The equilibrium time scale for this expression is

$$\tau = \frac{1}{\sqrt{C_{\text{cap}} C_{\text{ann}} + \frac{1}{4} C_{\text{self}}^2}} \ . \tag{3.8}$$

Below we show that the self-capture effect on the equilibrium time is negligible for our parameter range of interest. The solution to the rate equation in the relevant limit $C_{\rm self}^2 \ll C_{\rm cap} C_{\rm ann}$ is

$$N_X = \sqrt{\frac{C_{\rm cap}}{C_{\rm ann}}} \tanh \frac{t}{\tau} \qquad\qquad \Gamma_{\rm ann} \equiv \frac{1}{2} C_{\rm ann} N_X^2 = \frac{1}{2} C_{\rm cap} \tanh^2 \frac{t}{\tau} \ . \tag{3.9}$$

The factor of 1/2 accounts for the fact that two dark matter particles are removed in each annihilation. When the age of the Sun is greater than the equilibrium time, $\tau_\odot \simeq 4.5$ Gyr $> \tau$, the Sun is saturated with dark matter and the annihilation rate is maximized and matches the accumulation rate. For $\tau_\odot < \tau$, the dark matter population in the Sun is still growing and the $\tanh^2(\tau_\odot/\tau)$ factor suppresses the annihilation rate relative to the capture rate.

We now examine each term in Eq. (3.7).

3.4.1 Dark Matter Capture

The capture rate for dark matter scattering off of a particular nuclear species N in the Sun is the integral of the differential cross section over the volume of the Sun; the incident dark matter velocity, w; and the nuclear recoil energies, E_R, for which capture occurs:

$$C_{\rm cap}^N = n_X \int_0^{R_\odot} dr\, 4\pi r^2 n_N(r) \int_0^\infty dw\, 4\pi w^3 f_\odot(w,r) \int dE_R \frac{d\sigma_N}{dE_R}\bigg|_{\rm capture} \ , \tag{3.10}$$

where $n_X = \rho_X/m_X$ is the local dark matter number density, $n_N(r)$ is the N number density at a distance r from the solar center, $f_\odot(w,r)$ is the dark matter velocity distribution at that position, and $d\sigma_N/dE_R$ is the elastic scattering cross section. The full capture rate is the sum over all nuclear species in the Sun, $C_{\rm cap} = \sum_N C_{\rm cap}^N$.

The velocity of dark matter asymptotically far from the Sun, u, is distributed according to a Maxwell–Boltzmann-like velocity distribution. In the neighborhood of the Sun, this

distribution is distorted due to the solar gravitational potential. Taking this acceleration into account and invoking energy conservation, the incoming dark matter velocity w for an interaction with a nucleus in the Sun is

$$w^2 = u^2 + v_\odot^2(r) \ , \tag{3.11}$$

where $v_\odot(r)$ is the escape velocity at a distance r from the solar center. The dark matter velocity distribution, $f_\odot(w, r)$, thus satisfies

$$w^3 f_\odot(w, r)\, dw = u \left[u^2 + v_\odot^2(r)\right] f(u)\, du \ . \tag{3.12}$$

This may then be substituted directly into Eq. (3.10). We use the asymptotic velocity distribution in the solar rest frame,

$$f_\odot(u) = \frac{1}{2} \int_{-1}^{1} dc\, f\left(\sqrt{u^2 + u_\odot^2 + 2uu_\odot c}\right) , \tag{3.13}$$

where $u_\odot = 233$ km/s is the solar velocity in the galactic rest frame, and

$$f(u) = N \left[\exp\left(\frac{v_{\rm gal}^2 - u^2}{k u_0^2}\right) - 1\right]^k \Theta(v_{\rm gal} - u) \ , \tag{3.14}$$

where $v_{\rm gal}$ is the galactic escape velocity and N is chosen to normalize the distribution to integrate to unity. The Maxwell–Boltzmann distribution is recovered for $k = 0$ and $v_{\rm gal} \to \infty$. The astrophysically favored range of parameters is [76]

$$220 \text{ km/s} < u_0 < 270 \text{ km/s} \qquad 450 \text{ km/s} < v_{\rm gal} < 650 \text{ km/s} \qquad 1.5 < k < 3.5 \ . \tag{3.15}$$

In this analysis we use the central values of these ranges. We confirm that varying these parameters in this range does not perceptibly alter the dark matter capture rate in the Sun [93].

The differential elastic scattering cross section in the non-relativistic limit is

$$\frac{d\sigma_N}{dE_R} = 8\pi\varepsilon^2\alpha_X\alpha Z_N^2 \frac{m_N}{w^2(2m_N E_R + m_{A'}^2)^2}|F_N|^2 \ , \tag{3.16}$$

where the Helm form factor is

$$|F_N|^2 = \exp\left(-\frac{E_R}{E_N}\right) \qquad\qquad E_N = \frac{0.114 \text{ GeV}}{A_N^{5/3}} \ , \tag{3.17}$$

for a target nucleus N with mass m_N and atomic number A_N. Dark matter captures in the Sun when the outgoing X velocity is less than the escape velocity $v_\odot(r)$ at distance r from the solar center. This occurs if sufficient energy, E_R, is transferred to the nucleus. The minimum energy transfer from an incident X with velocity w to the nucleus at distance r from the Sun in order for the dark matter to be captured is

$$E_{\text{min}} = \frac{1}{2}m_X\left[w^2 - v_\odot^2(r)\right] . \tag{3.18}$$

The range of allowed recoil energies is determined by kinematics. Writing the dark matter–nucleus reduced mass as μ_N, the lab frame recoil energy is

$$E_R = \frac{1}{2}E_{\text{max}}(1 - \cos\theta_{\text{CM}}) \qquad\qquad E_{\text{max}} = \frac{2\mu_N^2 w^2}{m_N} \ , \tag{3.19}$$

where we have identified the maximum kinematically permitted recoil energy, E_{max}. Capture occurs when $E_{\text{max}} > E_R > E_{\text{min}}$. It is convenient to write this as

$$\int dE_R \frac{d\sigma_N}{dE_R}\bigg|_{\text{capture}} = \int_{E_{\text{min}}}^{E_{\text{max}}} dE_R \frac{d\sigma_N}{dE_R}\Theta(\Delta E) \qquad\qquad \Delta E = E_{\text{max}} - E_{\text{min}} \ . \tag{3.20}$$

One may then substitute the results of Eqs. (3.12), (3.16), (3.20) into Eq. (3.10). In Ref. [7]

we showed that the resulting capture rate may be succinctly written as

$$C_{\rm cap} = 32\pi^3\varepsilon^2\alpha_X\alpha n_X \sum_N \frac{Z_N^2}{m_N E_N} \exp\left(\frac{m_{A'}^2}{2m_N E_N}\right) c_{\rm cap}^N \tag{3.21}$$

$$c_{\rm cap}^N = \int_0^{R_\odot} dr\, r^2 n_N(r) \int_0^\infty du\, u f_\odot(u)\Theta(\Delta x_N) \left[\frac{e^{-x_N}}{x_N} + {\rm Ei}(-x_N)\right]_{x_N^{\rm max}}^{x_N^{\rm min}} , \tag{3.22}$$

where we use the substitution variable x_N and exponential integral function [94],

$$x_N = \frac{2m_N E_R + m_{A'}^2}{2m_N E_N} \qquad\qquad {\rm Ei}(z) \equiv -\int_{-z}^\infty dt \frac{e^{-t}}{t} . \tag{3.23}$$

We use the AGSS09 solar composition model to extract the $n_N(r)$ [129, 130, 131]. Ref. [76] tabulated the elements that give the largest contributions to dark matter capture: O, Fe, Si, Ne, Mg, He, S, and N. These are given in decreasing order of importance, but they are all significant, with the nitrogen contribution just a factor of 5 below that of oxygen in the $m_X \gg m_N$ limit. Hydrogen, the most abundant nucleus in the Sun, is a subdominant target, since the capture rate is proportional to $\mu_N^2 m_N Z_N^2$.

3.4.2 Dark Matter Annihilation

Captured dark matter thermalizes in the Sun for X–proton spin-independent scattering cross sections above 10^{-51}, 10^{-50}, and 10^{-47} cm^2 for $m_X = 100$ GeV, 1 TeV, and 10 TeV, respectively [53]. As we will see below, these values are greatly exceeded here. The dark matter, then, thermalizes and is Boltzmann distributed in a core near the center of the Sun, with number density

$$n_X(r) = n_0 e^{-r^2/r_X^2} \qquad r_X = \sqrt{\frac{3T_\odot}{2\pi G_N \rho_\odot m_X}} \approx 0.03\, R_\odot \left(\frac{100\ {\rm GeV}}{m_X}\right)^{1/2} . \tag{3.24}$$

Writing $\Gamma_{\rm ann} = \frac{1}{2}\int d^3\mathbf{x}\, n_X^2(\mathbf{x})\langle\sigma_{\rm ann}v\rangle$ and using the definition for $C_{\rm ann}$ in Eq. (3.9) gives

$$C_{\rm ann} = \langle\sigma_{\rm ann}v\rangle \left(\frac{G_N m_X \rho_\odot}{3T_\odot}\right)^{3/2} , \tag{3.25}$$

where the solar density and temperature are $\rho_\odot = 151$ g/cm^3 and $T_\odot = 15.5 \times 10^6$ K.

The captured dark matter is extremely cold, with typical velocity

$$v_0 = \sqrt{2T_\odot/m_X} = 5.1 \times 10^{-5}\sqrt{\text{TeV}/m_X} \ . \tag{3.26}$$

The thermally–averaged $XX \to A'A'$ cross section for annihilation is therefore significantly modified from the tree-level expression given in Eq. (3.3) to

$$\langle\sigma_{\rm ann}v\rangle = S\ \langle\sigma_{\rm ann}v\rangle^{\rm Born} \ , \tag{3.27}$$

where S is the non-relativistic Sommerfeld enhancement [96] of the Born approximation annihilation rate. An analytic expression for S for the case of $m_{A'} \neq 0$ may be derived by approximating the Yukawa potential with the Hulthén potential [97, 98, 99], giving an enhancement of S-wave processes of

$$S_s = \frac{\pi}{a}\frac{\sinh(2\pi ac)}{\cosh(2\pi ac) - \cos(2\pi\sqrt{c - a^2c^2})} \quad \xrightarrow{c\gg 1} \quad \frac{\pi\,\alpha_X/v}{1 - e^{-\pi\alpha_X/v}} \ , \tag{3.28}$$

where $a = v/(2\alpha_X)$ and $c = 6\alpha_X m_X/(\pi^2 m_{A'})$. The Sommerfeld enhancement, S, is the thermal average of S_s,

$$\langle S_S\rangle = \int \frac{d^3v}{(2\pi v_0^2)^{3/2}}\, e^{-\frac{1}{2}v^2/v_0^2}\, S_S \ . \tag{3.29}$$

The general form of S_s on the left-hand side of Eq. (3.28) encodes the effects of resonances generated by the long-range potential. Ref. [7] showed that these resonances play a crucial

role for dark matter accumulation in smaller bodies such as the Earth which would otherwise not be in thermal equilibrium. In contrast, in the regime of parameter space of interest, the Sun is already in thermal equilibrium so that $\tanh \tau_\odot/\tau \approx 1$ in Eq. (3.9) and the effect of the detailed modeling of enhancements to $C_{\rm ann}$ is negligible.

3.4.3 Dark Matter Self-Capture

The effect of dark matter self-capture in the Sun, parametrized by $C_{\rm self}$ in Eq. (3.7), is studied in detail by Zentner in Ref. [75]. $C_{\rm self}$ becomes relevant in the regime of very large self-interactions relative to the annihilation rate. One may obtain large self-interactions in the limit of a light mediator since a low-velocity self-interaction enhancement analogous to Sommerfeld enhancement may boost the capture rate; indeed, such a scenario is separately of interest as a proposed solution to small-scale structure anomalies in astrophysics [31].

In the dark photon framework discussed here, we find that in the regions of parameter space where a signal is detectable in AMS, the effect of self-capture is negligible. Heuristically, this may be understood as resulting from the fact that, although the self-capture rate is indeed non-perturbatively-enhanced at small velocities, the annihilation rate is Sommerfeld-enhanced even more. This is because the self-scattering occurs with velocities $w \gtrsim v_\odot$, while the annihilation occurs at the much smaller velocities $v_0 \ll v_\odot$ in Eq. (3.29). As a result, as we will show below, the self-capture contribution to the equilibrium time in Eq. (3.8) may be safely ignored.

For completeness, however, we demonstrate how recent self-interacting dark matter results are applied to self-capture. Following Ref. [31], the relevant cross section for self-scattering is the viscosity cross section, $d\sigma_V/d\Omega = \sin^2\theta\, d\sigma/d\Omega$, which regulates forward and backward scattering divergences that do not affect the dark matter phase space evolution. For distinguishable particles, one may approximate this with the transfer cross section,

$d\sigma_T/d\Omega = (1-\cos\theta)d\sigma/d\Omega$. The transfer cross section only regulates the forward divergence, but there is an extensive literature on this cross section in the classical limit ($m_X w/m_{A'} \gg 1$) from the plasma physics literature [132, 133], which may be applied to the present case [134], yielding

$$\sigma_T \simeq \frac{\pi}{m_{A'}^2} \begin{cases} 4\beta^2 \ln(1+\beta^{-1}) & \text{if } \beta \lesssim 10^{-1} \\ 4\beta^2 \left(1+1.5\beta^{1.65}\right)^{-1} & \text{if } 10^{-1} \lesssim \beta \lesssim 10^3 \\ \left(\ln\beta + 1 - \frac{1}{2\ln\beta}\right)^2 & \text{if } \beta \gtrsim 10^3 \end{cases} \qquad \beta \equiv \frac{2\alpha_X m_{A'}}{m_X w^2} \ , \tag{3.30}$$

Over most of the regime for solar dark matter self-capture, $C_{\text{self}} \sim \sigma_T \sim \alpha_X^2$. Parametrically,

$$C_{\text{cap}} C_{\text{ann}} \sim \varepsilon^2 \alpha \alpha_X^3 S \qquad\qquad C_{\text{self}}^2 \sim \alpha_X^4 \ , \tag{3.31}$$

where $S \sim \alpha_X$. Since both terms scale as α_X^4, one cannot tune the dark sector coupling to suppress the ordinary capture rate relative to the self-capture rate. Thus self-capture can only become a dominant effect in the small ε regime. We show below that this only occurs for ε so small that the Sun is not in equilibrium. In the extreme case, when ε is so small that $C_{\text{cap}} C_{\text{ann}} \ll C_{\text{self}}^2$, then $\tau \approx 2/C_{\text{self}}$ in Eq. (3.8) is typically much larger than the age of the Sun, $\tau_\odot$, and the annihilation rate is suppressed.

Beyond the classical regime, Eq. (3.30) must be modified. In the so-called resonant regime where

$$\frac{\alpha_X m_X}{m_{A'}} \gtrsim 1 \qquad \text{and} \qquad \frac{m_X v}{m_{A'}} \lesssim 1 \ , \tag{3.32}$$

one may approximate the Yukawa potential between the dark matter particles with the Hulthén potential which may be solved analytically for S-wave scattering. In the regime of $m_{A'}/m_X \lesssim v$, however, higher partial waves are required and one must perform a full numerical integration of the Schrödinger equation. A detailed investigation of this limit is

beyond the scope of this study.

3.4.4 Equilibrium Time

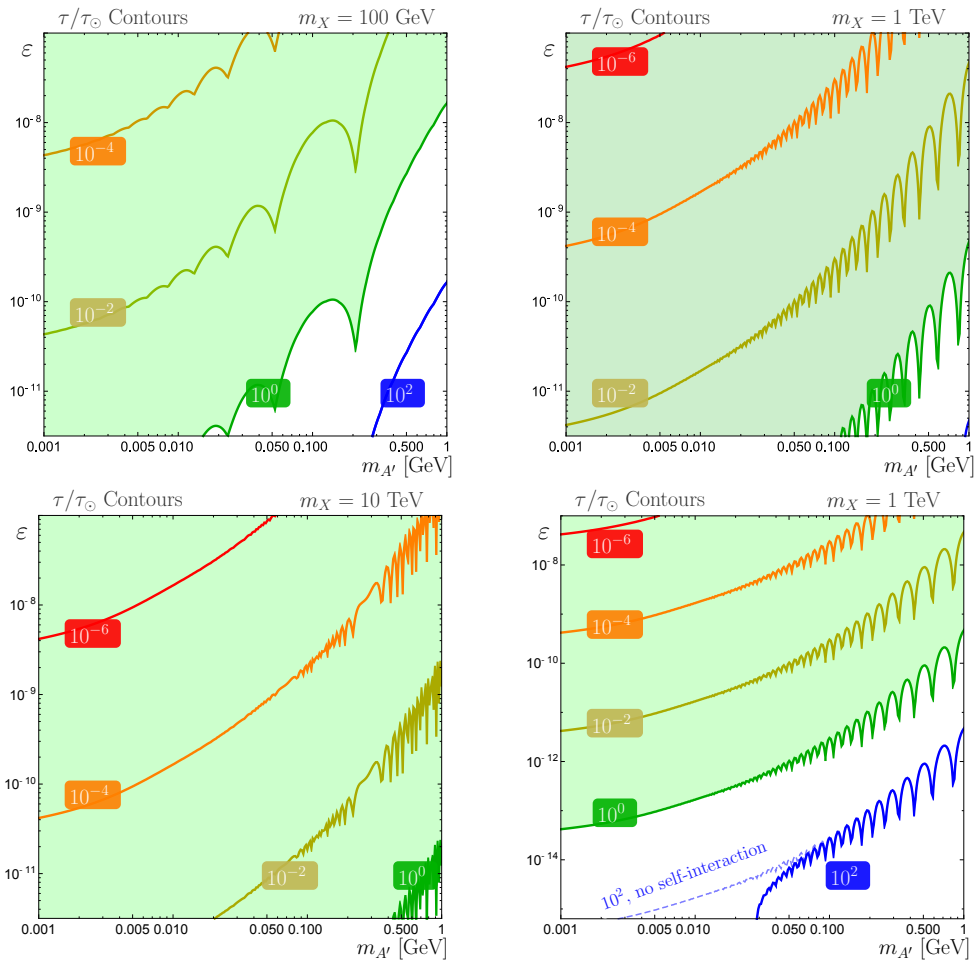

Figure 3.2: Contours of constant $\tau/\tau_\odot$, the equilibrium timescale in units of the Sun's age, in the $(m_{A'}, \varepsilon)$ plane for $m_X = 100$ GeV (top left), 1 TeV (top right), and 10 TeV (bottom left). The dark sector fine-structure constant α_X is set by requiring $\Omega_X \simeq 0.23$. In the green shaded regions, $\tau_\odot < \tau$ and the Sun's dark matter population has reached equilibrium. **Bottom–Right**: contours for $m_X = 1$ TeV, as in the top right, but extending to very low ε. The dashed line shows the case where self-capture has been ignored. The effect of self-capture becomes relevant only for very low ε, where equilibrium times are large and the annihilation signal is highly suppressed.

Fig. 3.2 presents results for the equilibrium time, τ, defined in Eq. (3.8). The region for which τ is less than the age of the Sun, $\tau_\odot$, is shaded in green. The contours in Fig. 3.2 reflect the

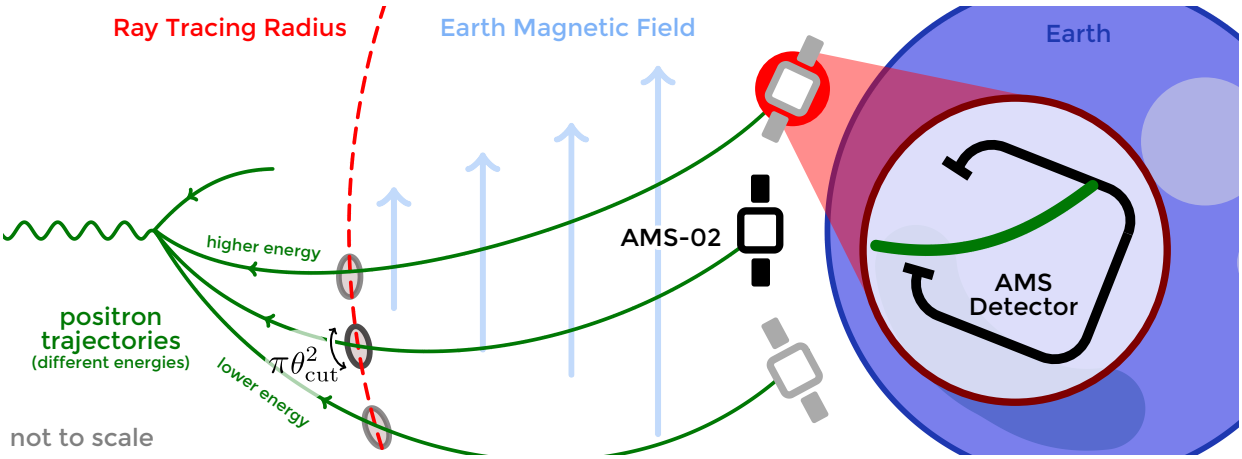

Figure 3.3: Schematic depiction of positron trajectories bending in the Earth's magnetic field. For each positron energy, one considers a solid angle $\pi\theta^2_{\rm cut}$ given by Eq. (3.38). Since the Earth's magnetic field is well known this mapping is well defined. The inset shows the origin of the angular dependence implicit in the Sun exposure in Eq. (3.36).

Sommerfeld resonances from Eq. (3.28). Unlike the case of the Earth studied in Ref. [7], these resonances do not play a major role since, in the region probed by AMS, $\tanh^2 \tau_\odot/\tau \approx 1$ and the annihilation rate in Eq. (3.9) is not affected by further enhancements. The bottom right plot shows the regime where self-interactions are significant and cause a noticeable deviation from the $C_{\rm self} = 0$ limit. As noted above, this only occurs in the region where the Sun is not yet in equilibrium so that the dark matter annihilation rate is suppressed.

3.5 Positron Signal and Background at AMS

The dark photons produced by dark matter annihilation in the Sun decay to all kinematically-accessible charged SM particles, leading to a variety of possible signals (e^+e^-, $\mu^+\mu^-$, $\pi^+\pi^-$, etc.) that can be detected in a number of experiments. We consider the e^+e^- signal for dark photons with $m_{A'} > 2m_e$. We specifically focus only on positrons, since the e^+ and e^- signals have identical properties and the positron background is smaller [135], and we consider the AMS-02 experiment on the International Space Station (ISS), which is optimal for positron detection.

The positron signal and background are very different: the signal has a hard spectrum and points back to the Sun, while the astrophysical background drops rapidly with energy and is effectively isotropic. In principle, it is therefore easy to isolate the signal by considering very energetic positrons that point back to the Sun. In practice, however, the signal is greatly complicated by the magnetic fields of the Sun and Earth, which each significantly deflect even TeV positrons. In the following, we begin by accounting for the Sun's magnetic field, which is not well constrained, and neglecting the Earth's magnetic field, which is relatively well understood.

Our general strategy is the following: for fixed parameters m_X, $m_{A'}$, and ε, and a given experimental live time T, we consider only positrons with energies above $E_{\rm cut}$ that point back to the Sun within an angle $\theta_{\rm cut}$. For a particular choice of $E_{\rm cut}$, we choose $\theta_{\rm cut}(E_{\rm cut})$ so that the number of background positrons is $N_B = 1$. We then determine the number of signal positrons, N_S, that pass these cuts, given a model for the Sun's magnetic field. We then determine the optimal value of the energy cut, $E_{\rm cut}^{\rm opt}$, which maximizes N_S, and we use these maximal values of N_S to determine the reach of AMS.

This procedure neglects the Earth's magnetic field. Since this magnetic field is well mapped, we assume that its effect on the signal may be de-convoluted so that positrons can be ray-traced back to a distance of several $R_\oplus$ from the Earth, where the Earth's magnetic field is negligible. It is at this position that the solid angle of size $\pi\theta_{\rm cut}^2$ should be defined. This is shown schematically in Fig. 3.3.

In the remainder of this section we discuss the number of background events N_B, the bending of positrons in the solar magnetic field, the number of signal events N_S, and the optimization of N_S.

3.5.1 Number of Background Events: Energy and Angular Cuts

We define the signal to be positrons with energies above $E_{\rm cut}$ that point back to the Sun within an angle $\theta_{\rm cut}$. Together, these parameters control the number of background positrons. The background isotropic positron flux has been precisely measured by AMS [135] to be

$$\frac{d\Phi}{dE} \approx \frac{1.5 \times 10^{-9}}{\text{GeV cm}^2 \text{ sr s}} \left(\frac{E}{100 \text{ GeV}}\right)^{-2.8} . \tag{3.33}$$

The number of background events in the signal region is, then,

$$N_B(E_{\rm cut}, \theta_{\rm cut}) = \xi_\odot \, \Omega_\odot(\theta_{\rm cut}) \int_{E_{\rm cut}}^{\infty} \frac{d\Phi}{dE} dE \ , \tag{3.34}$$

where, for small $\theta_{\rm cut}$,

$$\Omega_\odot(\theta_{\rm cut}) = \pi \, \theta_{\rm cut}^2 \text{ sr} \simeq 9.6 \times 10^{-4} \text{ sr} \left(\frac{\theta_{\rm cut}}{1^\circ}\right)^2 \tag{3.35}$$

is the solid angle subtended by $\theta < \theta_{\rm cut}$, and $\xi_\odot$ is the exposure of AMS to the Sun, a function of positron energy, the ISS's orbit, and AMS's fixed orientation on the ISS. For positron energies above 50 GeV, a detailed calculation finds that in 924 days of livetime, AMS's exposure to the Sun was $\xi_\odot \simeq 1.6 \times 10^5$ m^2 s [136]. Assuming uniform operating conditions, then,

$$\xi_\odot = 6.3 \times 10^4 \text{ m}^2 \text{ s} \frac{T}{\text{yr}} \simeq 20 \text{ cm}^2 \ T \ , \tag{3.36}$$

where T is the AMS livetime, that is, its total time in orbit. The "effective area" 20 cm^2 is much smaller than the geometric size of the detector due, in part, to the fact that the Sun is only in the field of view a small fraction of the time. For comparison, if AMS spent 100% of its livetime with the sun at the center of its field of view, the exposure would be about 80 times larger [136].

The resulting number of background events is

$$N_B(E_{\rm cut}, \theta_{\rm cut}) = 0.051 \left(\frac{100\ \text{GeV}}{E_{\rm cut}}\right)^{1.8} \left(\frac{\theta_{\rm cut}}{1^\circ}\right)^2 \left(\frac{T}{\text{yr}}\right) \ . \tag{3.37}$$

Fixing $\theta_{\rm cut}$ as a function of $E_{\rm cut}$ for a given T by requiring only a single background event, $N_B = 1$, yields

$$\theta_{\rm cut}(E_{\rm cut}) = 4.4^\circ \left(\frac{E_{\rm cut}}{100\ \text{GeV}}\right)^{0.9} \left(\frac{\text{yr}}{T}\right)^{1/2} \ . \tag{3.38}$$

3.5.2 Bending of Signal Positrons by the Solar Magnetic Field

Before quantifying the number of signal events, let us examine the bending of a signal positron by the solar magnetic field. In the absence of magnetic fields between the Sun and the Earth, positrons from solar dark photon decays would point back to within a degree (for $m_X > 100$ GeV) of the center of the Sun where the dark matter is concentrated within a core of radius r_X from Eq. (3.24). The AMS electromagnetic calorimeter's angular resolution is parametrized by $\Delta\theta_{68} \simeq \sqrt{5.8^{\circ 2}/(E \text{ in GeV}) + 0.23^{\circ 2}}$ [118]; the angular resolution from the tracker is even better [136]. For the positron energies we will consider, the experimental angular resolution is therefore less than a degree and is negligible.

The signal, however, is smeared out by the solar magnetic field, which bends charged particles as they travel to the Earth. Because of the solar wind, the magnetic field of the Sun differs from a dipole and varies with the 11-year solar cycle. As an approximation, we use the Parker model for the heliospheric magnetic field, which has radial and azimuthal components in heliocentric coordinates [137]; see Refs. [138, 139] for reviews. Since the positrons propagate

in the radial direction, it is sufficient to model the azimuthal part of the magnetic field,

$$B_\phi = \left(\frac{3.3\ \text{nT}}{\sqrt{2}}\right)\frac{\text{au}}{r}\ , \tag{3.39}$$

where we have used the facts that at $R = \text{au}$, $|\mathbf{B}| = 3.3$ nT and the radial and azimuthal components of the field are equal in magnitude. We ignore a subleading r^{-2} piece in B_ϕ which is suppressed by a factor of $R_\odot = 0.005$ au. This model was invoked in Ref. [140] to explain the PAMELA positron excess as the result of increased activity during the solar cycle. With this magnetic field, the bending angle of a positron of energy E produced at a dark photon decay position r_d from the Sun is

$$\theta_{\text{bend}}(r_d, E) = 8.9^\circ \left(\frac{\text{TeV}}{E}\right)\int_{r_d}^{\text{au}} \frac{B_\phi(r')\,dr'}{\text{au}\,(3.3\ \text{nT})} = 6.3^\circ \left(\frac{\text{TeV}}{E}\right)\ln\frac{\text{au}}{r_d}\ . \tag{3.40}$$

3.5.3 Number of Signal Events

The total number of signal events N_S is

$$N_S = N_S^0\,\text{Br}(A' \to e^+e^-)\,P_{\text{det}}\ , \tag{3.41}$$

where

$$N_S^0 = 2\Gamma_{\text{ann}}\,\frac{\xi_\odot}{4\pi(1\ \text{au})^2} \tag{3.42}$$

is the number of dark photons produced when the Sun is in AMS's field of view, $\text{Br}(A' \to e^+e^-)$ is the probability that a dark photon decays to a positron, and P_{det} is the probability that such a positron is detected within the signal region by AMS. In Eq. (3.42), the factor of 2 accounts for the two dark photons produced per dark matter annihilation, and $\xi_\odot$ is the exposure defined in Eq. (3.36). N_S^0 and $\text{Br}(A' \to e^+e^-)$ are completely determined by the

model parameters, while $P_{\rm det}$ depends also on the cut parameters.

We now determine the detection probability $P_{\rm det}$. For a positron to be detected in the AMS signal region, (1) it must be created by a dark photon that decays after traveling a distance between $R_\odot$ and 1 au, and (2) it must not be deflected out of the signal region by the solar magnetic field. Letting r_d be the distance a dark photon travels before it decays. condition (2) implies

$$\theta_{\rm bend}(r_d, E) \leq \theta_{\rm cut}(E_{\rm cut}) \ , \tag{3.43}$$

or, given Eqs. (3.38) and (3.40),

$$r_d \geq r_d^{\rm min}(E, E_{\rm cut}) \equiv \ {\rm au}\ e^{-E/E_0(E_{\rm cut})} \ , \tag{3.44}$$

where

$$E_0(E_{\rm cut}) \equiv 1.5\ {\rm TeV} \left(\frac{100\ {\rm GeV}}{E_{\rm cut}}\right)^{0.9} \left(\frac{T}{\rm yr}\right)^{1/2} \ . \tag{3.45}$$

Positrons that do not satisfy Eq. (3.44) are produced too far from the Earth and are deflected too much to satisfy the angle cut. Given the two constraints on r_d, the signal region in the space of dark photon decay position r_d and positron energy E is bounded by

$$R_\odot \leq r_d \leq {\rm au} \qquad r_d^{\rm min}(E, E_{\rm cut}) \leq r_d \qquad E_{\rm min} \leq E_{\rm cut} \leq E \leq m_X \ , \tag{3.46}$$

where $E_{\rm min} = 50$ GeV is the minimum positron energy cut from AMS. This region is shown in Fig. 3.4.

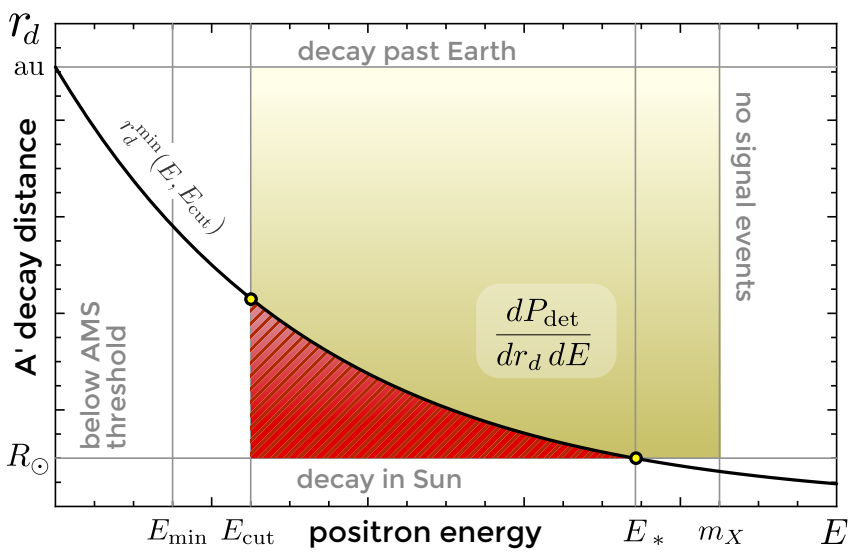

Figure 3.4: Schematic depiction of the signal region of integration, Eq. (3.46), in the plane of A' decay distance r_d and positron energy E. The beige shading represents the magnitude of the integrand, Eq. (3.47). We integrate over the box $R_\odot < r_d <$ au, $E_{\rm cut} < E < m_X$ and then subtract the integral over the red shaded region bounded by $R_\odot$ and $r_d^{\rm min}$.

The probability density for positrons to be produced at position r_d and energy E is

$$\frac{dP_{\rm det}}{dr_d\, dE} = \frac{e^{-r_d/L}}{L}\frac{1}{m_X} \ , \tag{3.47}$$

where the decay length, L, is defined in Eq. (3.2), and we have used the fact that for $m_e \ll m_{A'} \ll m_X$, the positron energies are evenly distributed in the range $0 \leq E \leq m_X$. Ref. [61] confirms that these positrons do not lose appreciable energy propagating to Earth.

The probability for a positron to be detected in the AMS signal region is, then,

$$P_{\rm det} = \int \frac{dP_{\rm det}}{dr_d\, dE}\, dr_d\, dE = \int e^{-r_d/L}\, \frac{dr_d}{L}\frac{dE}{m_X} \equiv P^0_{\rm det} - P^B_{\rm det}\, \Theta(E_* - E_{\rm cut}) \ , \tag{3.48}$$

where the region of integration is defined by Eq. (3.46). $P^0_{\rm det}$ and $P^B_{\rm det}$ are defined to be the integral over the box and the red region, respectively, in Fig. 3.4. $P^0_{\rm det}$ is the probability, in the absence of magnetic fields, that a dark photon will decay after traveling a distance between

$R_\odot$ and 1 au to produce a positron with energy greater than $E_{\rm cut}$. $P^B_{\rm det}$ is the correction to this naïve probability caused by the angular cuts to account for the solar magnetic field. E_* is defined to be the energy for which $r_d^{\rm min}(E_*, E_{\rm cut}) = R_\odot$. Above this energy the condition Eq. (3.44) is trivial since dark photons must decay beyond $R_\odot$ or else their decay products are caught in the Sun. The upper limit of the dE integral in $P^B_{\rm det}$ is

$$E_\times \equiv \min\left(E_*, m_X\right) \qquad \text{where} \qquad E_* = E_0 \log \frac{\rm au}{R_\odot} \ . \tag{3.49}$$

This definition of $E_\times$ is necessary since $E_* > m_X$ for sufficiently small $E_{\rm cut}$. For the Parker model of the solar magnetic field, the integrals can be evaluated exactly:

$$P^0_{\rm det} = \frac{m_X - E_{\rm cut}}{m_X}\left(e^{-\frac{R_\odot}{L}} - e^{-\frac{\rm au}{L}}\right) \tag{3.50}$$

$$P^B_{\rm det} = \frac{E_0}{m_X}\left[{\rm Ei}\left(-\frac{\rm au}{L}e^{-\frac{E_\times}{E_0}}\right) - {\rm Ei}\left(-\frac{\rm au}{L}e^{-\frac{E_{\rm cut}}{E_0}}\right)\right] + \frac{E_\times - E_{\rm cut}}{m_X}e^{-\frac{R_\odot}{L}} \ , \tag{3.51}$$

where the Ei function is defined in Eq. (3.23). The difference of exponentials in Eq. (3.50) determines the shape of the region of dark photon parameter space that can be reached. When $L \ll R_\odot$ this term drops rapidly because few dark photons decay outside the Sun. When $L \gg$ au, one may expand the exponentials so that

$$P^0_{\rm det} \approx \frac{m_X - E_{\rm cut}}{m_X}\frac{\rm au}{L} \propto \varepsilon^2 m_{A'}^2 \ . \tag{3.52}$$

This is illustrated in Fig. **??**, which shows contours of constant decay length L and how these shape the N^0_S and N_S reach. Values of $E_{\rm cut}$ are chosen for each choice of $(m_{A'}, \varepsilon)$ to optimize $P_{\rm det}$. Decreasing the dark matter mass m_X produces lower energy positrons which are subsequently deflected more by the magnetic fields so that the probability decreases. For example, at $m_X = 100$ GeV the maximum probability is reduced by two orders of magnitude relative to $m_X =$ TeV, significantly reducing the reach of AMS.

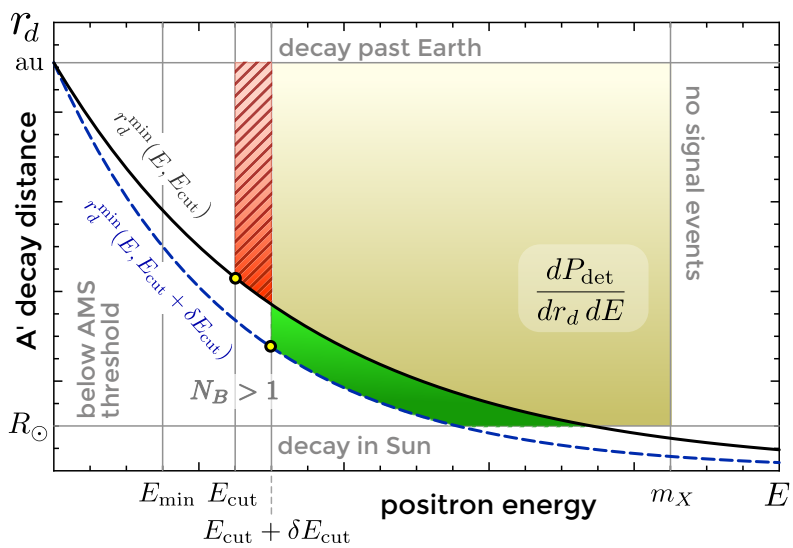

Figure 3.5: Schematic description of the signal region in the plane of decay distance r_d and positron energy E. As one varies $E_{\rm cut}$, the $r_d^{\rm min}$ line shifts downward while the lower limit of the dE integration shifts upward. The optimal $E_{\rm cut}$ is then when the integral over the red and green regions are equivalent. The shading represents the magnitude of the integrand, Eq. (3.47).

3.5.4 Optimizing the Signal

Throughout this study we choose $E_{\rm cut}$ to optimize the signal probability $P_{\rm det}$ while fixing the number of background events, $N_B = 1$. Because the probability is a concave function of $E_{\rm cut}$, the choice of $E_{\rm cut}$ as a function of $m_X, m_{A'}$, and ε is found by solving $dP_{\rm det}/dE_{\rm cut} = 0$, where

$$\frac{dP_{\rm det}}{dE_{\rm cut}} = -\frac{1}{m_X}\left(e^{-\frac{R_\odot}{L}} - e^{-\frac{\rm au}{L}}\right) + \frac{1}{m_X}\Theta(E_* - E_{\rm cut})\Big[\mathcal{F}_1\Theta(m_X - E_*) + \mathcal{F}_2\Big] \tag{3.53}$$

$$\mathcal{F}_1 = \frac{0.9E_0}{E_{\rm cut}}\left[e^{-\frac{R_\odot}{L}} - \exp\left(-\frac{\rm au}{L}e^{-\frac{E_\times}{E_0}}\right)\right]\log\frac{\rm au}{R_\odot} \tag{3.54}$$

$$\mathcal{F}_2 = e^{-\frac{R_\odot}{L}} - \exp\left(-\frac{\rm au}{L}e^{-\frac{E_{\rm cut}}{E_0}}\right) . \tag{3.55}$$

This equation is solved numerically to give the choice $E_{\rm cut}^{\rm opt}$ that optimizes $P_{\rm det}$. To clarify the nature of this optimization, we show the effect of varying $E_{\rm cut}$ in Fig. 3.5. Figure 3.6 shows a set of representative $E_{\rm cut}^{\rm opt}$ contours in the $(m_{A'}, \varepsilon)$ plane for $m_X = 10$ TeV.

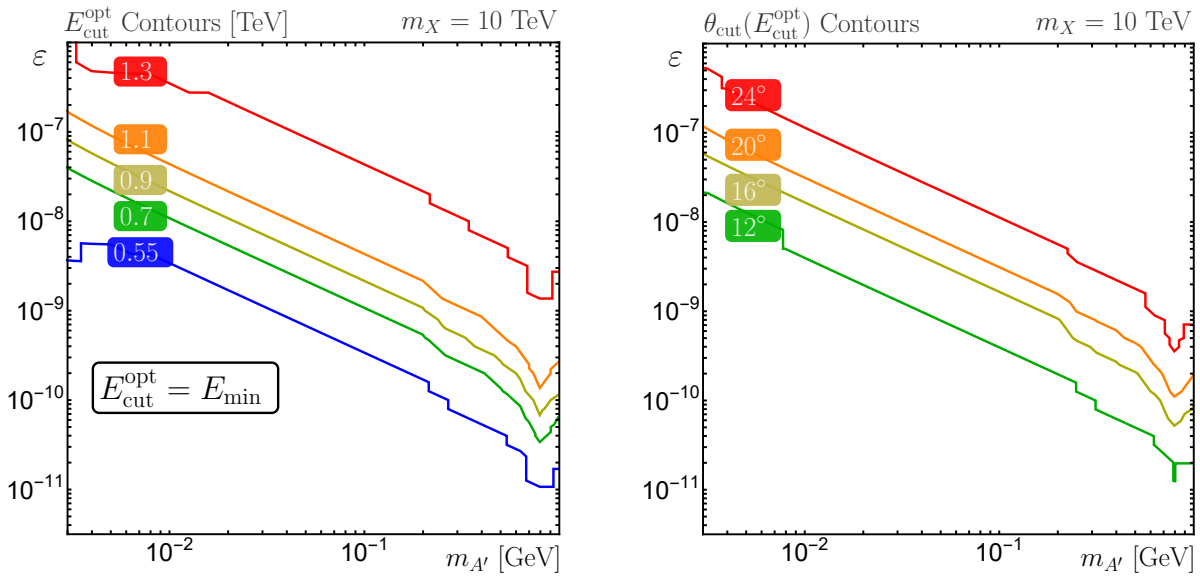

Figure 3.6: **Left:** Contours of $E_{\rm cut}^{\rm opt}$, the value of $E_{\rm cut}$ that maximizes the probability $P_{\rm det}$ in the $(m_{A'}, \varepsilon)$ plane for $m_X = 10$ TeV. In the region below lowest plotted contour, 550 GeV, $E_{\rm cut}^{\rm opt} > E_*$ so that the $P_{\rm det}^B$ term in Eq. (3.48) vanishes—the solar magnetic field does not affect the choice of cuts—and $E_{\rm cut}^{\rm opt} = E_{\rm min}$. **Right:** Contours of the corresponding values of $\theta_{\rm cut}$ from Eq. (3.38).

3.6 Results: AMS Reach

To provide a rough estimate of AMS's discovery potential, in Fig. 3.7 we show results for the number of signal events that pass the optimized cuts detailed in the previous section. Contours of N_S are given in the $(m_{A'}, \varepsilon)$ plane for both thermal ($\alpha_X^{\rm th}$) and maximal ($\alpha_X^{\rm max}$) dark sector couplings and for the benchmark dark matter masses, $m_X = 100$ GeV, TeV, and 10 TeV. These are the same benchmark masses used in our recent analysis of Earth capture of dark matter [7].

The N_S contours are shaped by the signal probability $P_{\rm det}$ shown in Fig. **??** and described in Sec. 3.5.3. This is in contrast to the case of Earth capture where the low-ε portion of the contours were shaped by the equilibrium condition and followed the Sommerfeld resonances analogous to Fig. 3.2. Although the two scenarios are qualitatively similar, their signal reach is limited by different physics. For a fixed m_X, the search for dark photons from the

Sun probes a region in the $(m_{A'}, \varepsilon)$ plane probes a region below that of the Earth capture scenario presented in Ref. [7]. This is as expected: solar dark photons must propagate further to escape the Sun than those from the Earth, and they thus provide sensitivity to a region of longer decay lengths L and smaller ε.

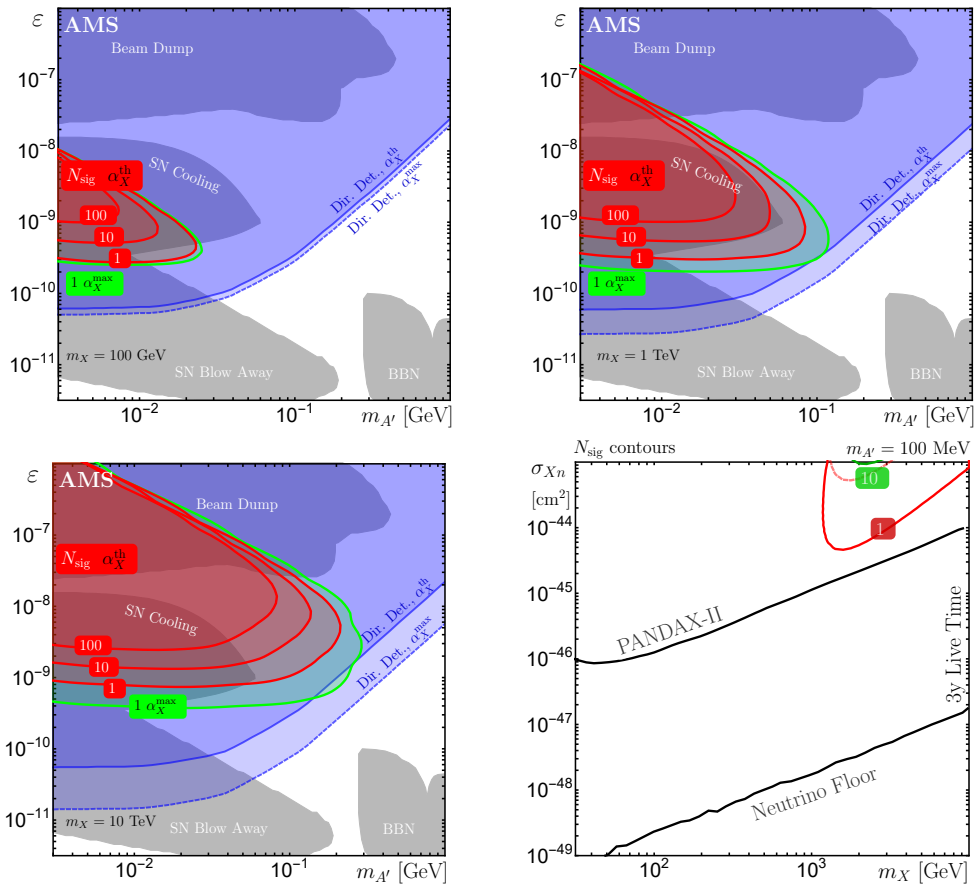

Figure 3.7: **Top** and **Bottom–Left**: Red: Number of AMS signal events N_S for $m_X = 100$ GeV, 1 TeV, 10 TeV, $N_B = 1$ background event, and livetime $T = 3$ years in the $(m_{A'}, \varepsilon)$ plane. The dark sector fine-structure constant α_X is set by requiring $\Omega_X \simeq 0.23$. Green: The $N_S = 1$ reach for $\alpha_X = \alpha_X^{\rm max}$, the maximal allowed coupling from CMB bounds [70, 71, 72], as written in Eq. (3.5). Blue: Current bounds from direct detection [101, 106]. Gray: Regions probed by other dark photon searches discussed in Sec. 3.3. **Bottom–Right**: Comparison of indirect and direct detection sensitivities in the (m_X, σ) plane for $m_{A'} = 100$ MeV. Red: $N_S = 1$ signal event contours for $\alpha_X = \alpha_X^{\rm th}$ (solid) and $\alpha_X^{\rm max}$ (dashed). Green: Same, but for $N_S = 10$. The direct detection bounds are from the PANDAX-II experiment [106]; note that in this regime the point-like interaction limit is valid; this is not the case for the low $m_{A'}$ region [109, 110, 101]. Also shown is the "neutrino floor," where coherent neutrino scattering affects direct detection experiments [111].

The N_S contours are not significance contours. A more detailed analysis is required to obtain significant contours, but we note that, in particular, in looking for an excess of signal positrons, we have treated all positrons with energies above $E_{\rm cut}$ with equal weight. This is a great oversimplification. For example, for models with $m_X = 10$ TeV, the signal is optimized for $E_{\rm cut} \sim 1$ TeV, as seen in Fig. 3.6, and so any positrons from the Sun's direction with energy between around 1 and 10 TeV contributes to N_S. But at the upper end of this range, the background is completely negligible, *even integrated over the whole sky.* If AMS detected just one multi-TeV positron, and it came from the direction of the Sun, this would be quite significant. In this case, the $N_S = 1$ contours may be thought of as characterizing the reach of AMS, whereas in other cases, requiring $N_S = 5$ over a background of $N_B = 1$ might be more reasonable.

With this caveat in mind, we now compare the signal reach to the sensitivities of other probes. In Fig. 5.1, the dark photon bounds from colliders, beam dumps, and cosmology outlined in Sec. 3.3 are shown in gray. For dark matter masses $M_X \gtrsim$ TeV, the search reach extends well beyond these bounds—the latter in part due to the recent reanalysis in Ref. [107] which had found that prior estimates have overestimated the reach of these searches by about an order of magnitude. Even given collider experiment and cosmology bounds, AMS could detect tens or even hundreds of high energy positrons from the Sun.

Direct detection experiments are, however, more sensitive. Current bounds from PANDAX-II are also shown in Fig. 5.1 in blue. For the framework analyzed here, the AMS reach contours probe the same region of parameter space as existing direct detection searches. This is due, in part, to the solar magnetic field deflecting the positrons and smearing out what is otherwise a very clean directional signal for AMS. The severity of this effect can be seen by comparing to Fig. 3.8, which shows the signal contours in the case where the solar magnetic field is ignored.

One may extend the signal reach by increasing the solar exposure. As a benchmark for this,

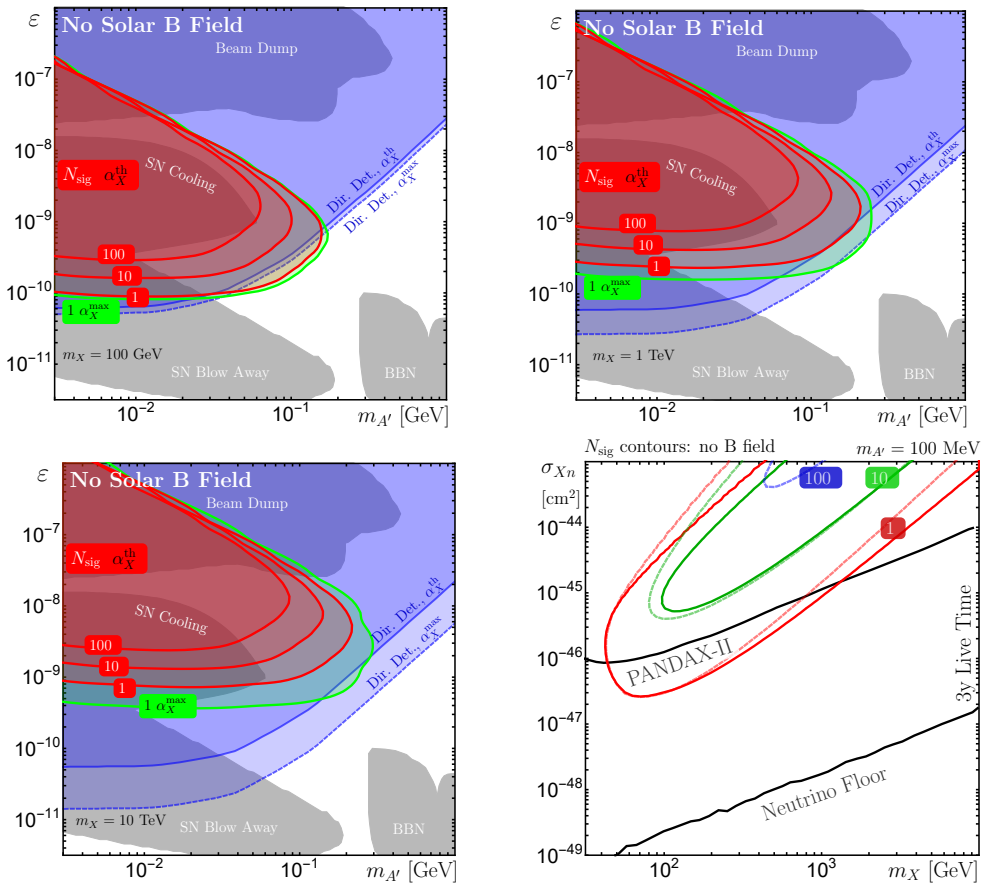

Figure 3.8: Same as Fig. 5.1 but with no solar B field. Comparing to Fig. 5.1, one sees that a large fraction of potential signal positrons are deflected for lighter dark matter masses.

Fig. 3.9 shows the reach of a hypothetical 'high solar exposure' experiment which the same properties as AMS but that points to the sun during its entire livetime. This corresponds to an exposure that is 80 times larger for $T = 3$ years livetime [136].

Direct detection experiments and the indirect detection signal analyzed here are, however, quite complementary. As an example, in this paper we have focused on the case where dark matter scatters elastically. However, the model already has all of the ingredients to introduce a pseudo-Dirac splitting between the dark matter states, if one assumes that the order parameter that controls the dark photon mass also gives a small Majorana mass to the X and $\bar{X}$. This was most recently explored in Ref. [141] for collider searches of dark matter–dark photon systems. As is well known, only a modest splitting is required to suppress the

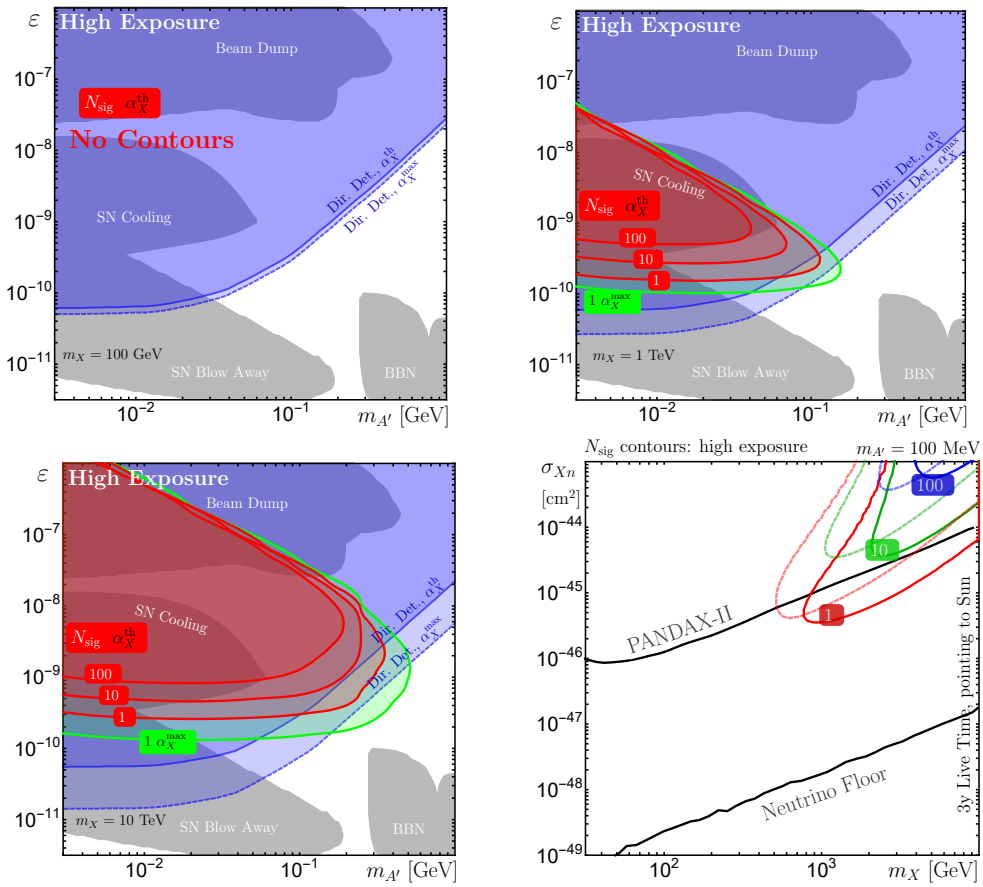

Figure 3.9: Same as Fig. 5.1 but for a hypothetical high-exposure experiment with $\xi_\odot^{\rm high} = 80\xi_\odot$. The condition of a single background event $N_B = 1$ in Eq. (3.38) sets such strong cuts that there are no signal positrons for $m_X \lesssim 500$ GeV.

direct detection signal [142]. In such a case, the solar capture process is largely unchanged. The splitting sets a lower bound on the relative velocity of dark matter–ordinary matter scattering, which sets an upper bound on the Sommerfeld enhancement. However, since the Sun is a large enough target that it is in equilibrium through most of the relevant parameter space, this reduced Sommerfeld enhancement does not have a large effect on the dark matter annihilation rate. Thus it is simple to consider a regime in theory-space where the high-m_X bounds in Fig. 5.1 probe new territory. We emphasize that this regime does not require any new ingredients beyond the assumptions implicit in the benchmark model of this paper. We leave a detailed study of this scenario to future work.

In the bottom–right panels of Figs. 5.1–3.9, we show these results in the usual direct detection

plane (m_X, σ_{Xn}) where σ_{Xn} is the X-nucleon cross section. We fix $m_{A'} = 100$ MeV. The reach of the solar dark photon signal appears to be greater for $\alpha_X^{\rm th}$ than for $\alpha_X^{\rm max}$. This is because $\sigma_{Xn} \sim \alpha_X \varepsilon^2$ so that σ_{Xn} corresponds to a smaller value of ε when assuming the maximal $\alpha_X^{\rm max}$ dark sector coupling versus the thermal value $\alpha_X^{\rm th}$.

3.7 Conclusions

We have presented a novel method to discover dark sectors whose gauge bosons kinetically mix with the SM. Dark matter is captured by the Sun and can yield a smoking gun signature when it annihilates to dark photons that exit the Sun. These dark photons then decay into e^+e^- pairs that may be searched for using directional discrimination from a space-based telescope such as AMS with its fantastic angular resolution. This search is insensitive to difficult-to-quantify astrophysical backgrounds and provides an opportunity for unambiguous dark matter discovery by AMS.

We have presented a complete treatment in the dark photon scenario that includes several effects that had heretofore been neglected. Our analysis incorporates the effect of non-perturbative Sommerfeld enhancements in the dark matter annihilation rate at the center of the Sun, which enlarges the region of parameter space in which dark matter capture and annihilation are in equilibrium. This is a necessary condition for a maximal annihilation rate. We have also addressed the non-perturbative enhancements in dark matter self-scattering at low velocities. These affect the rate of dark matter self-capture. In most of the phenomenologically relevant parameter space, self-capture remains a subdominant effect. We pointed out regimes that may be of interest for self-interacting dark matter models, where there may be significant deviations from our analysis.

We modeled the effects of the solar magnetic field on the experimental reach of the AMS

detector. These magnetic fields smear out the signal, weakening the directionality of the signal, which would otherwise be effectively point-like. Assuming high-energy positrons can be accurately ray-traced back to regions where the Earth's magnetic field is negligible, we defined a set of cuts that optimize the signal probability $P_{\rm det}$ subject to a fixed number of allowed background events, and we estimated the reach for AMS with three years of data. The reach extends beyond regions probed by beam dump and supernova bounds, and is similar to the regions probed by direct detection. These latter bounds, however, are much less stringent if the dark matter section includes even very small pseudo-Dirac mass splittings. Such splittings are generic in our framework and require no additional ingredients. We leave a detailed exploration of this scenario to future work [3]. For comparison, we have also shown results for the case where the signal is not degraded by bending in a solar magnetic field, and for a hypothetical AMS-like experiment that points at the Sun and so has 80 times its exposure. In both of these cases, again requiring negligible background, the number of signal events is improved by an order of magnitude.

In Ref. [7] we showed that the IceCube experiment can be used to search for captured dark matter in the Earth annihilating into dark photons. For dark sunshine leading to positrons and electrons, however, the IceCube signal is suppressed, since these positrons and electrons will be captured in the Earth before entering IceCube. However, if the dark photons decay into muons, these muons may penetrate through kilometers of earth to reach IceCube. Because the amount of earth between the Sun and IceCube is time dependent, this signal would have an annual modulation. Separately, we have shown in the appendix that gauge invariance requires dark photons to have a small coupling to the weak neutral current. For small masses this is suppressed relative to the coupling to the electric current, but such a neutrino signal would not be affected by the solar magnetic fields which afflict the positron signal. It may then be interesting to recast IceCube searches for solar neutrinos in terms of an excess coming from intermediate dark photons that decay to neutrinos.

Chapter 4

Dark Photons from Inelastic Dark Matter at the Center of the Sun

The following is based on a previously published paper by the author and Philip Tanedo [3].

4.1 Introduction

As we have seen, direct detection experiments still place stringent constraints on the simplest kinetic mixing portal theories, and it is natural to ask if variations on these models can avoid direct detection bounds while remaining accessible to other experiments.

Inelastic models were initially invoked for just this purpose: to reconcile the experimental tension between the DAMA modulation signal and null results from CDMS [142, 143], in part because even a small mass splitting $\Delta \sim 100$ keV can weaken upper limits on the spin-independent cross section from nuclear recoils by many orders of magnitude. These models are also appealing for their potential to resolve small scale structure problems if the mass splitting is $\Delta \gtrsim 50$ keV [144].

In this manuscript we focus on a simplified model of a self interacting inelastic dark sector that interacts with the Standard Model by kinetic mixing [29, 30] between a hypothesized massive $U(1)_X$ gauge boson, hereafter referred to as the "dark photon" [33, 34], and the Standard Model photon.

In previous work [7, 6] we investigated a novel indirect detection signal of the elastic limit of this model: dark matter is captured by astrophysical objects and annihilates into dark photons. These dark photons then stream outwards and decay to Standard Model particles that may be detected by existing experiments. We found that dark matter capture and annihilation within the Earth could produce unique signals in the IceCube Neutrino Observatory over a large, currently unconstrained region of parameter space with dark matter masses 100 GeV $\lesssim m_X \lesssim$ 10 TeV. We discovered further that the same process occurring in the Sun, which we term "dark sunshine," may result in energetic positrons detectable by the Alpha Magnetic Spectrometer (AMS-02), providing a probe of the dark sector unconstrained by dark photon exclusions from fixed target experiments and supernova observations, with 100 GeV $\lesssim m_X \lesssim$ 10 TeV, 1 MeV $\lesssim m_{A'} \lesssim$ 100 MeV, and $10^{-10} \lesssim \varepsilon \lesssim 10^{-8}$. This region of

parameter space exhibits a large overlap with the parameter space excluded by large noble liquid direct detection experiments. We now ask whether inelastic models that obviate these exclusions could still be found through dark sunshine.

This is not an obvious question. Inelastic models avoid direct detection constraints due to the kinematics of endothermic scattering. Dark matter that falls into the Earth's gravitational well will typically not be energetic enough to scatter. We may suspect, on the other hand, that the stronger gravitational influence of the Sun will allow these interactions to occur, even at mass splittings that prohibit scattering in terrestrial liquid xenon experiments. In such a case we expect that the solar dark matter capture and annihilation rates are only mildly suppressed by the addition of a mass splitting, rendering a dark sunshine search as potentially the only way to observe dark matter in our solar system.

To answer this question, we perform a complete analysis of dark matter capture and annihilation in the Sun with this model, including kinematic suppression of dark matter capture relative to the elastic case, modification of the annihilation rate due to Sommerfeld enhancement in inelastic models, relaxation of competing limits from direct detection, and the effect of the Sun's magnetic field on the positron signal at AMS-02. We find that even with mass splittings large enough to weaken constraints from LUX by two orders of magnitude, the capture and annihilation processes are only weakly affected. As a result, there exist regions of parameter space untouched by other probes of the dark sector, and favored by small scale structure observations, where AMS-02 is expected to see tens or hundreds of energetic positrons produced by boosted dark photon decays in existing datasets. For the case of dark matter capture by the Earth, we find that in the case when the inelastic mass splitting is small our results are unchanged from earlier analysis, but that the Earth does not capture dark matter efficiently when the mass splitting is large enough to substantially modify direct detection limits on the model.

Dark matter capture and annihilation in gravitating bodies has been examined before [37,

38, 39, 40, 41, 42, 44, 43, 46, 49] with early works considering the production of neutrinos by captured dark matter annihilation in the Sun, while more recent studies have focused on the production of new particles beyond the Standard Model, of which dark photons are one example [60, 57, 58, 59]. The ANTARES neutrino telescope has recently placed limits on a similar scenario to what we have considered, searching for muons and neutrinos coming from mediator decays in a secluded dark matter framework [145]. Kouvaris et al. further examine "darkonium" bound states in the Sun and argue that AMS-02 may be sensitive to dark photons emitted during the formation of these bound states [146]. Inelastic dark matter models have also been previously applied to other astrophysical anomalies [147], collider searches [148, 141], and solar dark matter capture [149].

4.2 Model

The hidden sector we consider in this manuscript consists of two Dirac fermions of nearly identical masses interacting inelastically through the gauge boson of a broken $U(1)_X$ gauge symmetry, called the "dark photon," that kinetically mixes with the Standard Model hypercharge boson. Inelastic couplings may be introduced in the fermion sector by diagonalizing a mass matrix that induces maximal mixing between the two species. A model of an inelastic dark sector consisting of Majorana fermions was given in Ref. [142], and most SUSY-inspired dark sector models share this trait. To comport with our earlier work on dark matter capture and annihilation we have chosen to use a simplified model of inelastic Dirac dark matter. This class of model was first invoked in Ref. [150]. Here we provide an explicit construction to establish notation. Suppose that the dark sector consists of two Dirac fermions, denoted ψ and χ, which carry opposite-sign $U(1)_X$ charges. The relevant dark sector interactions are

$$\mathcal{L}_{\text{dark}} \supset g_X \bar{\psi} \not{A}' \psi - g_X \bar{\chi} \not{A}' \chi - \begin{pmatrix} \bar{\psi} & \bar{\chi} \end{pmatrix} \begin{pmatrix} M & m \\ m & M \end{pmatrix} \begin{pmatrix} \psi \\ \chi \end{pmatrix} . \tag{4.1}$$

We assume $M \gg m$. We can now rewrite the Lagrangian in terms of the mass eigenstates $X_{1,2} = (\psi \mp \chi)/\sqrt{2}$:

$$\mathcal{L}_{\text{dark}} \supset g_X \bar{X}_2 \not{A}' X_1 + g_X \bar{X}_1 \not{A}' X_2 - (M - m)\bar{X}_1 X_1 - (M + m)\bar{X}_2 X_2 \ . \tag{4.2}$$

If the mass matrix is more general both elastic and inelastic couplings may occur, with arbitrary relative strength. We have chosen to consider the simpler case. We emphasize that these inelastic couplings may be accomplished without the introduction of any new fields beyond a second fermion in the dark sector: the mass matrix consists of terms that are either $U(1)_X$ invariant or that may be produced when the $U(1)_X$ is broken by a dark-charged Higgs field. We assume that the Higgs field responsible for the dark photon mass is heavy enough that its dynamics do not affect the phenomena we will examine.

The diagonalization of the dark photon–SM gauge Lagrangian has been detailed elsewhere [151, 152, 6], and results in an effective theory where the dark photon has mixing parameter ε suppressed couplings to the SM electromagnetic current, and coupling to the weak neutral current further suppressed by $m_{A'}^2/m_Z^2$. Because we consider dark photons of mass below 1 GeV, the latter coupling can be safely neglected, and the effective Lagrangian of our simplified model is

$$\begin{aligned}\mathcal{L} = &-\frac{1}{4}F_{\mu\nu}F^{\mu\nu} - \frac{1}{4}F'_{\mu\nu}F'^{\mu\nu} + \frac{1}{2}m_{A'}^2 A'^2 + \sum_f \bar{f}\left[i\not{\partial} - q_f e(\not{A} + \varepsilon \not{A}') - m_f\right] f \\ &+ i\bar{X}_1 \not{\partial} X_1 + i\bar{X}_2 \not{\partial} X_2 + g_X \bar{X}_2 \not{A}' X_1 + g_X \bar{X}_1 \not{A}' X_2 - m_X \bar{X}_1 X_1 \\ &- (m_X + \Delta)\bar{X}_2 X_2 \ .\end{aligned} \tag{4.3}$$

In the above expression we sum over SM fermions f with electric charge q_f, g_X is the hidden $U(1)$ gauge coupling, $m_X \equiv M - m$ is the mass of the lighter of the two hidden sector particles, the dominant component of the dark matter, and $\Delta \equiv 2m$ is the mass splitting between the two species. Henceforth in this manuscript, unless there is ambiguity, we will

omit subscripts and refer to the lighter species as simply X.

This model has five free parameters: m_X, Δ, $m_{A'}$, g_X, and ε. We assume that $m_X > m_{A'}$. We fix g_X by assuming that the dark matter abundance is set by thermal freeze-out of the process $\bar{X}X \to A'A'$, which is the dominant annihilation channel in the case where $\varepsilon \ll g_X$. In the limit where the mass splitting is much smaller than the dark matter mass, which we assume throughout, the thermal relic density is unaffected at the 10% level by the presence of the more massive state [153]. In order to satisfy the observed abundance as a thermal relic we take [119]

$$\alpha_X = 0.035 \left(\frac{m_X}{\text{TeV}}\right) \ . \tag{4.4}$$

The dark photon decay rate is given by

$$\Gamma = \frac{1}{\text{Br}(A' \to e^+e^-)} \frac{\varepsilon^2 \alpha (m_{A'}^2 + 2m_e^2)}{3m_{A'}} \sqrt{1 - \frac{4m_e^2}{m_{A'}^2}} \ . \tag{4.5}$$

Our assumption that $m_X > m_{A'}$ implies that there are no hidden sector states into which the dark photon can decay. The branching ratio to electrons is then 1 when $2m_e < m_{A'} < 2m_\mu$, and at higher masses it is determined from hadron production at colliders [74]. From this we write the boosted dark photon decay length, which determines whether dark photons produced by dark matter annihilation are able to escape the Sun before decaying and thus produce a positron signal at AMS-02:

$$L = \frac{v\gamma}{\Gamma} = R_\odot \ \text{Br}(A' \to e^+e^-) \left(\frac{1.1 \times 10^{-9}}{\varepsilon}\right)^2 \left(\frac{m_X/m_{A'}}{1000}\right) \left(\frac{100 \text{ MeV}}{m_{A'}}\right) \ , \tag{4.6}$$

where $R_\odot = 7 \times 10^{10}$ cm $= 4.6 \times 10^{-3}$ au is the radius of the Sun and we have taken the limit $m_e \ll m_{A'} \ll m_X$.

4.3 Experimental Constraints

The possibility of a hidden $U(1)_X$ boson that kinetically mixes with the photon has been extensively investigated, both as part of an interacting dark sector and as a stand-alone extension of the Standard Model. Here we review those experimental constraints relevant for the region of parameter space accessible to dark sunshine.

4.3.1 Direct Detection Experiments

Direct detection experiments bound the dark matter–nucleon cross section for weak scale dark matter, which in this model is a function of the dark coupling constant, the dark matter and dark photon mass, and the kinetic mixing parameter. The strongest current bounds come from the PANDAX-II experiment [106]. In the inelastic dark matter framework, direct detection bounds are modified and generically produce weaker exclusion limits [142, 154, 155].

Before we proceed it is a good idea to have a general idea of the orders of magnitude involved. In order for the lighter state to scatter at all against a nucleus of mass m_N it must have a lab frame speed $w_{\min}$ of

$$w_{\min} = \sqrt{2\Delta\left(\frac{1}{m_N} + \frac{1}{m_X}\right)} \,. \tag{4.7}$$

We can estimate from this the size of the mass splitting that will forbid scattering. If dark matter has a characteristic velocity of 220 km/s and a mass much higher than that of the nucleus, and we take $m_N \sim 100$ GeV we see that $\Delta \sim 100$ keV. We now make this more precise.

The differential nuclear recoil rate in a detector whose fiducial volume encompasses N_T nuclei with mass m_N, mass number A, and atomic number Z, when the dark matter velocities follow

a Maxwell–Boltzmann distribution, is given by [156]

$$\frac{dR}{dE_R} = \frac{N_T m_N \rho_X}{4 u_0 m_X} F_N^2(E_R) \frac{\sigma_{Xn}}{\mu_n^2} \frac{\left(f_p Z + f_n (A - Z)\right)^2}{f_n^2} \left(\frac{\mathrm{erf}(y_{\min} + \eta) - \mathrm{erf}(y_{\min} - \eta)}{\eta} \right) \ . \quad (4.8)$$

This formula depends on

- The Helm form factor:

$$F_N^2 = \exp\left(-\frac{E_R}{E_N}\right) \qquad\qquad E_N = \frac{0.114 \text{ GeV}}{A_N^{5/3}} \ . \quad (4.9)$$

- The Earth's velocity in the galactic rest frame in units of the velocity of the local standard of rest, u_0:

$$\eta \equiv \frac{u_\oplus}{u_0} = \frac{V_\odot + V_\oplus \cos\gamma \cos(\omega(t - t_0))}{u_0} \ , \quad (4.10)$$

  where $u_0 = 220$ km/s, $V_\odot = u_0 + 12$ km/s, $V_\oplus = 30$ km/s, $\omega = 2\pi/\text{yr}$, $t_0 =$ June 2, and $\cos\gamma = 0.51$ describes the inclination of the Earth's orbital plane relative to the Sun's orbit about the galactic center. Both here and in our later examination of the dark matter capture rate we adhere to the conventions established by Gould [44, 43, 46, 49]: u denotes "asymptotic" velocities far from the gravitational influence of the Sun, v denotes escape velocities, and w denotes lab frame velocities at the point of interaction.

- The speed y of a WIMP incident on the detector in units of u_0. Its lower limit $y_{\min}$ corresponds to the lowest speed the WIMP can have while imparting a recoil energy E_R:

$$y_{\min} \equiv \frac{1}{u_0} \sqrt{\frac{1}{2 m_N E_R}} \left(\frac{m_N E_R}{\mu_N} + \Delta \right) \ , \quad (4.11)$$

  where μ_N is the reduced mass of the WIMP–nucleus system. This is in contrast to μ_n,

which denotes the reduced mass of the WIMP–nucleon system.

We note that direct detection limits are usually derived with the assumption that the dark matter velocities in the galaxy follow a Maxwell–Boltzmann distribution, in contrast to our treatment of dark matter capture. We confirmed in previous work that the capture rate in the Sun is only weakly sensitive to this discrepancy and we therefore expect our results to be valid over all distributions favored by dark matter halo observations and simulations.

Over a given time interval, the expected number of events seen within a window of nuclear recoil energies is given by

$$\frac{N_T m_N \rho_X}{4 u_0 m_X} \frac{\sigma_{Xn}}{\mu_n^2} \frac{(f_p Z + f_n (A - Z))^2}{f_n^2} \int dE_R \; dt \; F_N^2(E_R) \left(\frac{\mathrm{erf}(y_{\min} + \eta) - \mathrm{erf}(y_{\min} - \eta)}{\eta} \right) , \tag{4.12}$$

where the limits of integration are determined by the experiment's nuclear recoil sensitivity and the live time of the experiment. In order to roughly evaluate the effect of a nonzero mass splitting on the PANDAX-II bounds, we notice that only the integral over recoil energy and time is dependent on Δ, through the dependence on $y_{\min}$. For a fixed detector composition and size we see that for each dark matter mass, upper limits on σ_{Xn} scale as

$$\sigma_{Xn}^{\mathrm{upper}} \propto \left[\int dE_R \; dt \; F^2(E_R) \left(\frac{\mathrm{erf}(y_{\min}(\Delta) + \eta) - \mathrm{erf}(y_{\min}(\Delta) - \eta)}{\eta} \right) \right]^{-1} . \tag{4.13}$$

To explicitly evaluate the recoil integral we assume that the fiducial volume of PANDAX-II is composed entirely of nuclei of $Z = 54$ and $A = 131$. We assume that PANDAX-II has a nuclear recoil threshold of 1 keV, and average the Earth's velocity relative to the WIMP wind over a full annual cycle. The results of this scaling on the (m_X, σ_{Xn}) plane are shown in Figure 4.1.

These bounds on the cross section can be translated into bounds on light mediators between

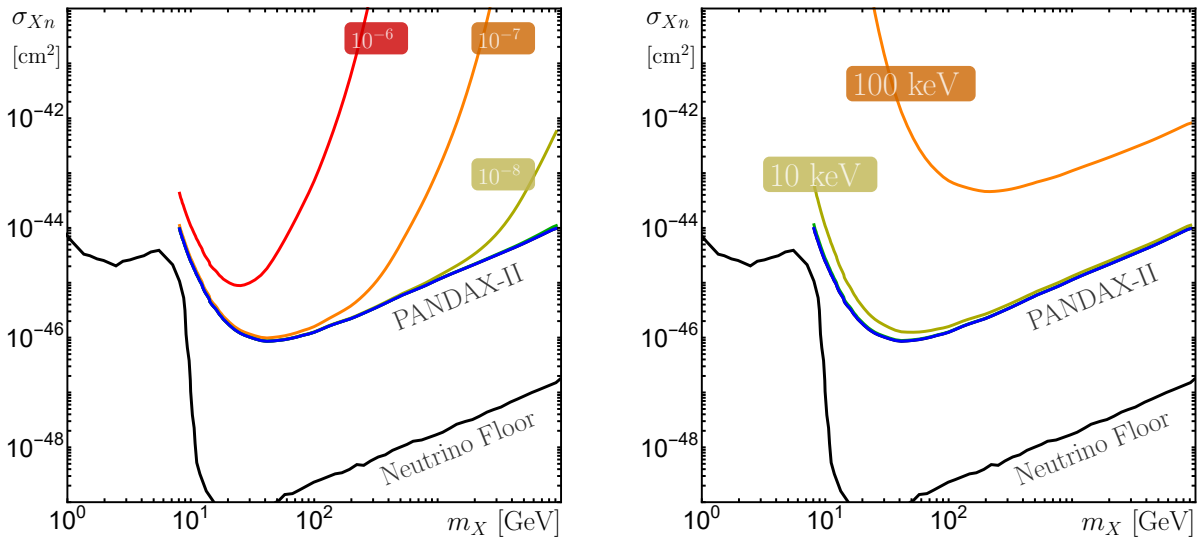

Figure 4.1: **Left:** Rescaling of PANDAX-II limits (Blue) [106] on spin independent WIMP–nucleon scattering for indicated fixed values of $\delta \equiv \Delta/m_X$. Red: $\delta = 10^{-6}$, Orange: $\delta = 10^{-7}$, Yellow: $\delta = 10^{-8}$. **Right:** Same as Left, but for fixed values of Δ. Orange: $\Delta = 100$ keV. Yellow: $\Delta = 10$ keV. Also shown is the neutrino floor, where coherent scattering of solar and atmospheric neutrinos will appear as background in direct detection experiments.

the dark and visible sector [101], and can therefore be shown on the dark photon $(m_{A'}, \varepsilon)$ plane. To see how these bounds change when a dark sector mass splitting is introduced, we notice that the WIMP–nucleon cross section is quadratically dependent on the kinetic mixing parameter, and therefore that bounds on ε will scale like the recoil integral raised to the $-1/2$ power. Representative effects of this scaling will be shown in Sec. **??**.

We caution the reader not to take such a scaling argument too literally. The imposition of a hard cutoff for the nuclear recoil threshold and simple integration over detector livetime ignores details of the PANDAX-II detector response and data analysis as well as the Poissonian nature of direct detection event rates, but this will suffice to give a rough understanding of how direct detection bounds are modified in inelastic models.

4.3.2 Fixed Target Experiments

Fixed target experiments attempt to produce dark photons by bremsstrahlung off of SM beam constituents and search for the decay of these dark photons to SM particles after they have propagated a large distance through shielding material. Because we assume that the dark photon can decay only to SM states, these searches are insensitive to the matter content and coupling of the dark sector. As such we are able to plot the bounds from fixed target dark photon searches in the $(m_{A'}, \varepsilon)$ plane, and these bounds will remain unchanged as we sweep over m_X and Δ. The bounds that most overlap with our proposed search region for dark sunshine come from E137 [120, 121] and LSND [122, 123, 124], which jointly constrain dark photons with 1 MeV $\lesssim m_{A'} \lesssim$ 300 MeV and $10^{-8} \lesssim \varepsilon \lesssim 10^{-5}$. For a review of fixed target dark photon searches see Ref. [35].

4.3.3 Supernova Observations

Light, weakly interacting particles may be emitted from core-collapse supernovae, shortening the resulting burst of energetic neutrinos. Observations of SN1987A constrain the couplings and masses of dark photons for 1 MeV $\lesssim m_{A'} \lesssim$ 100 MeV and $10^{-9} \lesssim \varepsilon \lesssim 10^{-7}$ [102, 103, 104, 105, 107]. These bounds, however, have recently come under scrutiny [105, 157, 158, 107] with special focus placed on the production of dark photons through nucleus–nucleus bremsstrahlung and accounting for effects of the stellar environment. It is always prudent to claim the most conservative exclusion region, and for these purposes we use the exclusions provided by Ref. [107]. Another set of bounds can be placed from the absence of an MeV γ signal from SN1987A [104], though these may also be affected by the treatment of nucleus–nucleus bremsstrahlung in supernovae. In the absence of a more complete published analysis we will continue to show these bounds, which apply for 1 MeV $\lesssim m_{A'} \lesssim$ 100 MeV and $10^{-11} \lesssim \varepsilon \lesssim 10^{-9}$. The bounds from Ref. [103] require that the dark matter is light enough

($m_X \lesssim 100$ MeV) to be produced in the supernova core and are thus not applicable here.

4.3.4 Indirect Detection

Observations of the diffuse positron spectrum constrain the dark sector coupling α_X [60, 57, 58]. These constraints do not conflict with the thermal value of α_X that we use throughout this manuscript.

4.3.5 Cosmology

Cosmic microwave background observations constrain dark matter annihilation in the early universe and thus α_X [70, 71, 72, 73]. Ref. [73] provides the most stringent constraints, but these bounds do not reach the thermal relic value of α_X for the masses we consider. Big bang nucleosynthesis also constrains properties of long-lived dark photons independently of the dark matter characteristics [128]. The relevant bounds to our proposed search come from the observed abundance of ^{4}He and exclude dark photons of mass 300 MeV $\lesssim m_{A'} \lesssim$ 10 GeV and kinetic mixing $10^{-12} \lesssim \varepsilon \lesssim 10^{-10}$.

4.4 Dark Matter in the Sun

Dark matter becomes captured by the Sun if scattering with nuclei results in the final state particle traveling too slowly to escape the Sun's gravity. The captured dark matter sinks to the core and reaches thermal equilibrium with the surrounding matter. As it accumulates in the core the dark matter annihilates into pairs of dark photons. Due to the low temperature of the Sun's core, the tree level annihilation process receives large corrections from Sommerfeld enhancement. A detailed treatment of this process is given in Ref. [6]. In this manuscript

we will highlight the modifications to the calculation resulting from the presence of a mass splitting. We find that the main difference occurs in the capture process, while for the mass splittings we consider the annihilation is unchanged.

For the masses we consider it suffices to examine only capture from dark matter scattering off of nuclei, ignoring the effects of dark matter self-capture [75] and dark matter evaporation [41, 42]. The rate of dark matter annihilation in the Sun is

$$\Gamma_{\rm ann} = \frac{1}{2} C_{\rm cap} \tanh^2 \frac{t}{\tau} \ , \tag{4.14}$$

where $C_{\rm cap}$ is the rate of dark matter capture and τ is the timescale at which the capture and annihilation rates balance so that the total number of dark matter particles in the Sun is roughly constant. As we can see, when the lifetime of the body t is less than the equilibrium timescale τ the annihilation rate drops quickly, while for $t > \tau$ the annihilation rate is approximately constant in time and proportional to the capture rate. The primary impact to our signal rate due to the addition of inelasticity stems from the capture kinematics, to which we now turn.

4.4.1 Dark Matter Capture

The differential rate for dark matter scattering off of nuclei is proportional to the densities of the interacting particles and their velocity distributions. We work in heliocentric coordinates in the Sun's rest frame, and take the nuclei comprising the Sun to be at rest. The differential rate is then

$$d^3r \ d^3w \ dE_R \ n_X \ n_N(r) \ w \ f_\odot(w,r) \frac{d\sigma_N}{dE_R} \ , \tag{4.15}$$

where w is the velocity of the incident dark matter, r is the position, n_X and n_N denote the number densities of dark matter and nuclei, respectively, $f_\odot(w,r)$ is the velocity distribution

of dark matter, and $d\sigma_N/dE_R$ is the differential scattering cross section. Dark matter passing through the solar system will become captured when it scatters off of a nucleus such that the final state dark sector particle has a velocity below the Sun's escape velocity. This requirement imposes a limit on the recoil energies leading to capture. We integrate the above rate over the volume of the body and over the appropriate limits on recoil energy and velocity to find the capture rate for a single species of nucleus N:

$$C_{\rm cap}^N = n_X \int_0^R dr\ 4\pi r^2 n_N(r) \int_{w_{\rm min}}^\infty dw\ 4\pi w^3 f_\odot(w,r) \int_{\rm cap} dE_R\ \frac{d\sigma_N}{dE_R}\ . \tag{4.16}$$

The nontrivial lower limit on the lab frame velocity integral derives from kinematics: in the model provided in Sec. 4.2 the only allowed hidden sector vertex involves a transition from the lighter state to the heavier state or vice versa. If the incident dark matter's kinetic energy is too low to produce the heavier state, scattering simply does not occur. The threshold energy occurs when the heavier state and the nucleus are both at rest in the dark matter–nucleus CM frame after the collision, which implies

$$E_{\rm thresh} = \Delta\left(\frac{m_X}{m_N} + 1\right) \tag{4.17}$$

to leading order in Δ. This lower limit on the incident dark matter's kinetic energy furnishes a lower limit on velocity, in the non-relativistic limit:

$$w_{\rm min} = \sqrt{2\Delta\left(\frac{1}{m_N} + \frac{1}{m_X}\right)}\ . \tag{4.18}$$

The limits on recoil energy are determined in part by the capture requirement and in part by kinematics. The recoil energy is given in terms of the CM frame scattering angle $\theta_{\rm CM}$ by

$$E_R = \frac{\mu_N^2 w^2}{m_N}\left(1 - \cos\theta_{\rm CM}\right)\ . \tag{4.19}$$

The upper limit of E_R then occurs when $\cos\theta_{\rm CM} = -1$:

$$E_R^{\rm max} = \frac{2\mu_N^2 w^2}{m_N} \ . \tag{4.20}$$

The lower limit is set by the requirement that the nucleus carry away enough of the incident energy that the outgoing WIMP is moving too slowly to escape the Sun. Conservation of energy yields

$$E_R^{\rm min} = \frac{1}{2} m_X u^2 - \frac{1}{2}\Delta v_\odot^2(r) \ , \tag{4.21}$$

where $v_\odot$ is the escape velocity of the Sun and u is the asymptotic velocity of the dark matter in the Sun's rest frame. This lower limit represents a cut on the final state phase space of the scattering process, as distinguished from the earlier discussion of the threshold velocity, which determines whether the reaction can occur.

Using the same differential cross section, dark matter velocity distribution [76], and solar model [130, 129, 131] as in Ref. [6], the dark matter capture rate can be written compactly:

$$C_{\rm cap} = 32\pi^3\varepsilon^2\alpha_X\alpha n_X \sum_N \frac{Z_N^2}{m_N E_N} \exp\left(\frac{m_{A'}^2}{2m_N E_N}\right) c_{\rm cap}^N \tag{4.22}$$

$$c_{\rm cap}^N = \int_0^{R_\odot} dr\, r^2 n_N(r) \int_{\sqrt{w_{\rm min}^2 - v_\odot^2(r)}}^\infty du\, u f_\odot(u)\Theta(\Delta x_N) \left[\frac{e^{-x_N}}{x_N} + {\rm Ei}(-x_N)\right]_{x_N^{\rm max}}^{x_N^{\rm min}} \ . \tag{4.23}$$

We have used a substitution variable

$$x_N \equiv \frac{2m_N E_R + m_{A'}^2}{2m_N E_N} \ , \tag{4.24}$$

with E_N

$$E_N = \frac{0.114 \text{ GeV}}{A_N^{5/3}} \ , \tag{4.25}$$

and Ei is the exponential integral function defined by

$$\mathrm{Ei}(z) \equiv -\int_{-z}^{\infty} dt \frac{e^{-t}}{t} \ . \tag{4.26}$$

We take the number density of dark matter in the solar system to be $n_X = 0.3\ \mathrm{GeV/cm^3}/m_X$.

We have verified that the treatment of dark matter capture presented above predicts the same $\mathcal{O}(1)$ suppression of solar capture for $\Delta \sim 100$ keV relative to the elastic case as that presented in Ref. [149], in the contact limit where $m_{A'}$ is large and the differential cross section's dependence on E_R enters only though the Helm form factor. For smaller values of $m_{A'}$ the capture rate is further suppressed.

In our earlier examination of "dark earthshine" at IceCube [7] we found that such a search can probe a large region of parameter space currently inaccessible to direct detection experiments. Given the modification of direct detection bounds in an inelastic framework, it is natural to ask if this virtue persists. The answer to this question is negative. We find numerically that when the dark matter mass splitting is large enough to significantly weaken direct direction constraints, the capture rate for dark matter in the Earth falls as well. This is an obvious result, since the scattering process for dark matter capture in the Earth is identical to that exploited by direct detection experiments. When the mass splitting is large enough that nuclear recoils in direct detection experiments are kinematically disallowed, we expect the capture process to be forbidden as well. For the mass splittings treated here we find that dark matter is simply moving too slowly around the Earth to be captured efficiently. With smaller mass splittings the direct detection exclusions are not qualitatively weakened while the potential signal rate at IceCube remains unchanged. For this reason we omit further discussion of dark matter capture in the Earth from the ensuing analysis and treat only the case of dark matter accumulated in the Sun, detectable by dark sunshine signatures at AMS-02.

4.4.2 Dark Matter Annihilation

The captured dark matter population can be taken to be in thermal equilibrium with the solar core when the WIMP–proton spin independent scattering cross section is greater than 10^{-51} cm^2 for $m_X = 100$ GeV, 10^{-50} cm^2 for $m_X = 1$ TeV, or 10^{-47} cm^2 for $m_X = 10$ TeV [53]. We found in previous work that the cross section is several orders of magnitude larger than this in the relevant regions of parameter space, so that our analysis of dark matter annihilation is consistent. However, there is another wrinkle introduced in the framework of inelastic dark matter that we have already mentioned: in a theory without an elastic vertex slowly traveling dark matter will not scatter, and therefore the dark matter population will not come to thermal equilibrium with the Sun's core if its temperature is lower than the dark matter mass splitting [155]. This obstacle can be circumvented, however, by the presence of a small elastic coupling with strength g'_X. In order for a large enough WIMP–proton SI cross section that allows thermalization we may take $g'_X \sim 10^{-2} g_X$, which is too small to affect our treatment of capture, annihilation, and direct detection constraints in the inelastic framework [159, 155]. Such a coupling arises naturally at the one-loop level from the bare Lagrangian provided in Sec. 4.2.

The annihilation coefficient, encoding the dependence of the captured dark matter annihilation rate on the spatial distribution and thermal cross section, is given by [76]

$$C_{\rm ann} = \langle \sigma_{\rm ann} v \rangle \left[\frac{G_N m_X \rho_\odot}{3 T_\odot} \right]^{3/2} . \tag{4.27}$$

Here $T_\odot = 1.5 \times 10^7$ K ≈ 1.3 keV is the temperature at the center of the Sun, $\rho_\odot = 151$ g/cm^3 is the matter density at the core of the Sun, and G_N is Newton's gravitational constant.

Because of the low temperature of the core of the Sun relative to the dark matter mass, captured and thermalized dark matter will move very slowly and the annihilation process is Sommerfeld enhanced [96]. This modifies the annihilation cross section from the tree level

result to

$$\langle \sigma_{\rm ann} v \rangle = \langle S \rangle \langle \sigma_{\rm ann} v \rangle_{\rm tree} \ , \tag{4.28}$$

where $\langle S \rangle$ is the thermally-averaged Sommerfeld enhancement, given by

$$\langle S \rangle = \int \frac{d^3 v}{(2\pi v_0^2)^{3/2}} e^{-v^2/v_0^2} S \ , \tag{4.29}$$

with v_0

$$v_0 = \sqrt{\frac{2T_\odot}{m_X}} \approx 5.1 \times 10^{-5} \sqrt{\frac{\rm TeV}{m_X}} \ . \tag{4.30}$$

Here S is the Sommerfeld enhancement for a two-body system with definite relative velocity, which we define below.

A semi-analytic approximation for the s-wave Sommerfeld enhancement with a massive mediator coupling non-degenerate states can be found by solving the two-state Schrödinger equation with a matrix-valued potential encoding the mediator exchange diagrams [98]. The result of this analysis is

$$S = \frac{\pi}{\epsilon_v} \sinh\left(\frac{\epsilon_v \pi}{\mu}\right) \begin{cases} \frac{1}{\cosh(\epsilon_v \pi/\mu) - \cos\left(\sqrt{\epsilon_\delta^2 - \epsilon_v^2}\pi/\mu + 2\theta_-\right)} & \epsilon_v < \epsilon_\delta \\ \frac{\cosh\left(\left(\epsilon_v + \sqrt{-\epsilon_\delta^2 + \epsilon_v^2}\right)\pi/2\mu\right) \operatorname{sech}\left(\left(\epsilon_v - \sqrt{-\epsilon_\delta^2 + \epsilon_v^2}\right)\pi/2\mu\right)}{\cosh\left(\left(\epsilon_v + \sqrt{-\epsilon_\delta^2 + \epsilon_v^2}\right)\pi/\mu\right) - \cos(2\theta_-)} & \epsilon_v > \epsilon_\delta \end{cases} \ , \tag{4.31}$$

where $\epsilon_v = v/\alpha_X$, $\epsilon_\delta = \sqrt{2\Delta/m_X}/\alpha_X$, μ is given by

$$\mu = \epsilon_\phi \left(\frac{1}{2} + \frac{1}{2}\sqrt{1 + \frac{4}{\epsilon_\phi r_M}}\right) \ , \tag{4.32}$$

with $\epsilon_\phi = m_{A'}/m_X \alpha_X$, and r_M is defined implicitly by

$$\frac{e^{-\epsilon_\phi r_M}}{r_M} = \max\left[\epsilon_\delta^2/2, \epsilon_\phi^2\right] \ . \tag{4.33}$$

The quantity θ_- is

$$\theta_- = \frac{1}{i}\int_{r_S}^{r_M} \sqrt{\widetilde{\lambda_-}}\, dr - 4z_S^{1/4} - \frac{1}{i}\int_0^{r_M} \sqrt{\lambda_-}\, dr \tag{4.34}$$

where $\widetilde{\lambda_-}$ is given by

$$\widetilde{\lambda_-} = -\epsilon_v^2 + \epsilon_\delta^2/2 - \sqrt{(\epsilon_\delta^2/2)^2 + V_0^2 e^{-2\mu r}}\ , \tag{4.35}$$

with $V_0 \equiv \exp\left[\epsilon_\phi r_M \left(\sqrt{1+4/\epsilon_\phi r_M} - 1\right)/2\right]/r_M$, $z_S = V_0^2 e^{-2\mu r_S}/16\mu^4$ with r_S chosen such that $V_0 e^{-\mu r_S} \gg \epsilon_v^2, \epsilon_\delta^2$, and with λ_- defined

$$\lambda_- = -\epsilon_v^2 + \epsilon_\delta^2/2 - \sqrt{(\epsilon_\delta^2/2)^2 + e^{-2\epsilon_\phi r}/r^2}\ . \tag{4.36}$$

For the mass splittings we consider in this manuscript, with $\Delta/m_X \sim 10^{-9} - 10^{-6}$ this formula is well approximated by sending $\epsilon_\delta \to 0$, recovering the Sommerfeld factor from the elastic case.

4.4.3 Equilibrium Time

The equilibrium time $\tau = 1/\sqrt{C_{\rm cap} C_{\rm ann}}$ for the population of captured dark matter can be evaluated using the results from the two previous sections. We calculate the equilibrium time for the benchmark masses $m_X = 100$ GeV, 1 TeV, and 10 TeV over a range of the dark photon parameter space, for the mass splittings $\Delta = 100$, 10, and 1 keV. The regions of dark photon parameter space over which the Sun is currently in equilibrium are shown in Fig. 4.2. We see that at large masses the equilibrium times are very nearly the same as in the elastic case, and the reduction of the capture rate as the mass splitting increases is reflected most clearly for the 100 GeV case.

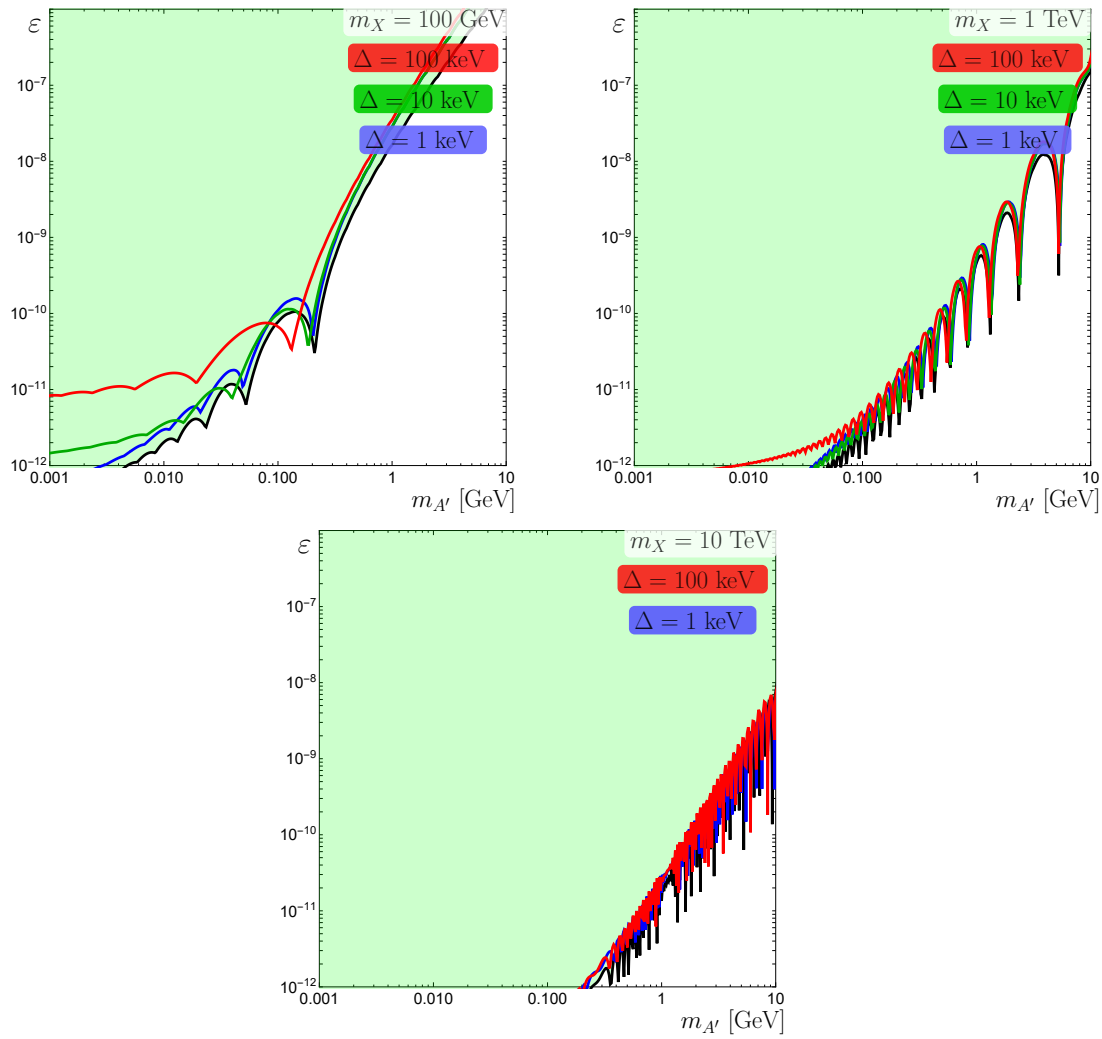

Figure 4.2: Contours of $\tau/\tau_\odot = 1$ in the $(m_{A'}, \varepsilon)$ plane for benchmark values of m_X and Δ, where $\tau_\odot = 4.6 \times 10^9$ yr is the age of the Sun. **Black:** Contours of $\tau/\tau_\odot = 1$ for the elastic case $\Delta = 0$. **Red:** Same, but for $\Delta = 100$ keV. **Green:** Same, but for $\Delta = 10$ keV. **Blue:** Same, but for $\Delta = 1$ keV. The dark sector coupling α_X is fixed by requiring that this dark sector match the observed density of dark matter as a thermal relic. For parameter values lying in the shaded region above and to the left of the given contours the captured dark matter population in the Sun is in equilibrium today.

4.5 Detection

Dark matter annihilations will produce dark photons that travel outwards from the Sun. If those dark photons are massive enough, they will decay to produce highly boosted e^+e^-

pairs. These energetic charged particles will be deflected by the Sun's magnetic field by the time they arrive at Earth. We suggest cuts on the energy and incidence direction of positrons so that the number of background positrons satisfying these cuts is reduced to 1. These cuts are derived in Ref. [6], and their effect is to include a multiplicative factor $P_{\rm det}$ correcting a naïve estimate of the flux of dark photons:

$$N_{\rm sig} = 2\Gamma_{\rm ann}\frac{\xi_\odot}{4\pi\ {\rm au}^2}\ {\rm Br}\left(A' \to e^+e^-\right) P_{\rm det}\ . \tag{4.37}$$

The factor $\xi_\odot$ denotes the "exposure" and has dimensions of area $\times$ time. Assuming uniform operating conditions and accounting for the fact that AMS-02 is only facing the Sun for a fraction of its livetime, its numerical value is [136]

$$\xi_\odot = 6.3 \times 10^4\ {\rm m}^2{\rm s}\ \frac{T}{\rm yr}\ , \tag{4.38}$$

where T is the total time over which AMS-02 has been operating in orbit.

Explicitly, $P_{\rm det}$ is

$$P_{\rm det} = \frac{m_X - E_{\rm cut}}{m_X}\left(e^{-R_\odot/L} - e^{-{\rm au}/L}\right) - P^B_{\rm det}\Theta\left(E_0 \log\frac{\rm au}{R_\odot} - E_{\rm cut}\right)\ , \tag{4.39}$$

where $P^B_{\rm det}$ is given by

$$P^B_{\rm det} = \frac{E_0}{m_X}\left[{\rm Ei}\left(-\frac{\rm au}{L}e^{-E_\times/E_0}\right) - {\rm Ei}\left(-\frac{\rm au}{L}e^{-E_{\rm cut}/E_0}\right)\right] + \frac{E_\times - E_{\rm cut}}{m_X}e^{-R_\odot/L}\ . \tag{4.40}$$

Here E_0 and $E_\times$ are defined

$$E_0(E_{\rm cut}) \equiv 1.5\ {\rm TeV}\left(\frac{100\ {\rm GeV}}{E_{\rm cut}}\right)^{0.9}\sqrt{\frac{T}{\rm yr}}\ , \qquad E_\times \equiv \min\left(E_0 \log\frac{\rm au}{R_\odot}, m_X\right)\ . \tag{4.41}$$

At each point in our scan of parameter space we numerically maximize $P_{\rm det}$ as a function

of $E_{\rm cut}$ with the minimal allowed $E_{\rm cut}^{\rm min} = 50$ GeV corresponding to the energy threshold at AMS-02.

4.6 Results and Discussion

We present here the results of our analysis for the benchmark masses $m_X = 100$ GeV, 1 TeV, and 10 TeV with mass splittings $\Delta = 10$ keV and 100 keV. When the mass splitting is lower than 10 keV we find that the region that can be probed by AMS-02 is qualitatively indistinguishable from that of previous analyses, where the mass splitting was set to zero. An analysis of the current AMS-02 dataset will serve as a complementary probe to the most recent exclusions from the LUX direct detection experiment for dark sectors in which the mass splitting is $\Delta \lesssim 10$ keV. For larger mass splittings, the AMS-02 signal region shrinks only modestly while exclusions from direct detection are relaxed by an order of magnitude or more in ε, leaving a significant window of parameter space that might only ever be probed by this search. The reduction of the AMS-02 signal window is reflective of the mild suppression of the capture rate: these contours do not approach the region of parameter space where the Sun is not presently in equilibrium and therefore the annihilation rate is directly proportional to the capture rate.

The reach of AMS-02 compared to other experimental probes discussed in Sec. 4.3, is shown in Fig. 4.3. For clarity, we have shown only the $N_{\rm sig} = 1$ contours for each value of the mass splitting. Contours corresponding to higher values of $N_{\rm sig}$ are determined by the variation of $P_{\rm det}$ as a function of ε and $m_{A'}$, as discussed in [6]. A rule of thumb for this, visible in our previous analysis, is that starting from the bottom of the $N_{\rm sig} = 1$ contours, an increase of half a decade in ε corresponds to a two decade increase in $N_{\rm sig}$. Accordingly, there are regions outside of the modified direct detection exclusions where the expected $N_{\rm sig}$ at AMS-02 may be of order 100 over the three year livetime. These are not significance contours. A more

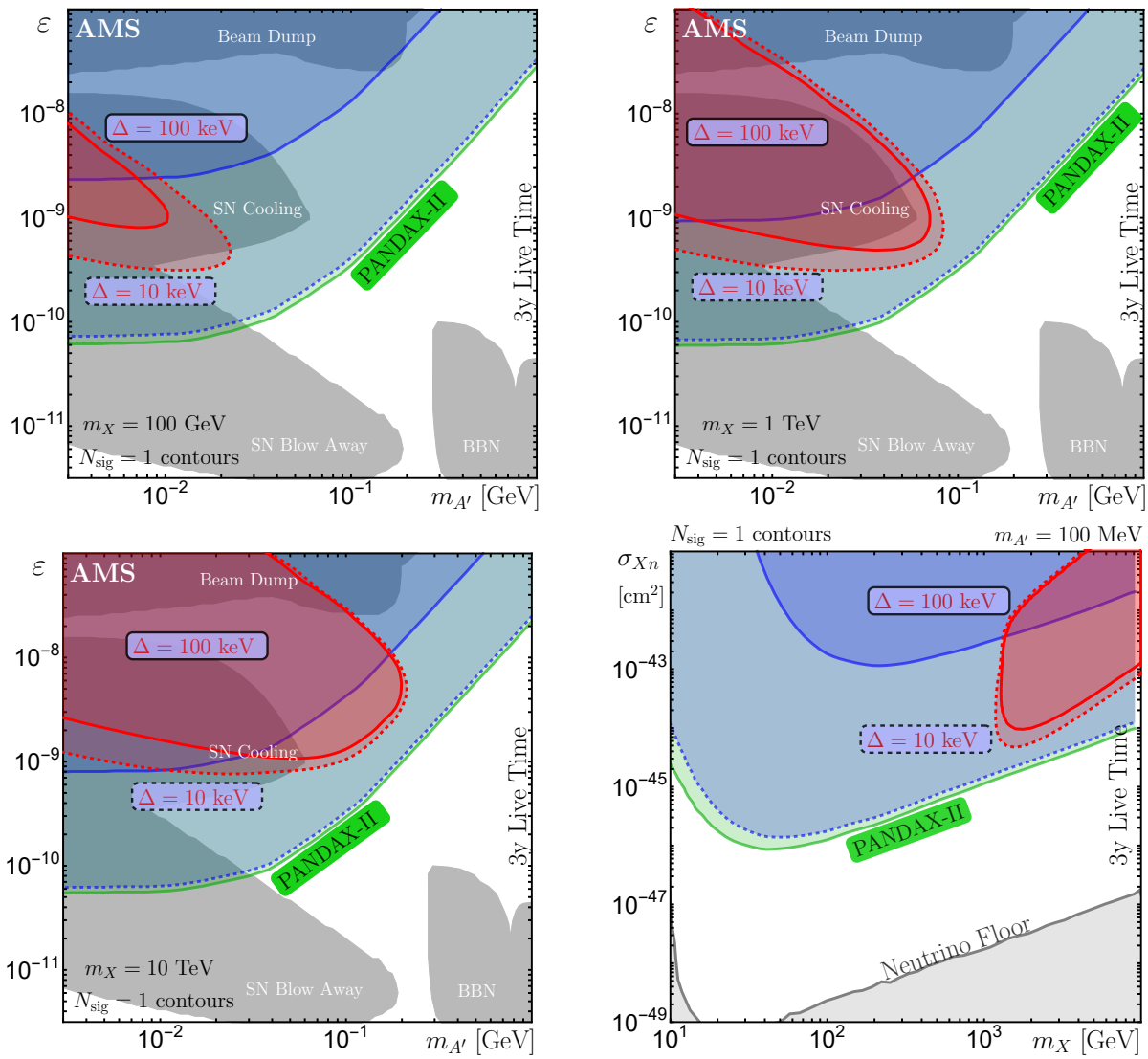

Figure 4.3: **Red:** AMS-02 reach region for $T = 3$ years live time in the $(m_{A'}, \varepsilon)$ plane for $m_X = 100$ GeV (top left), $m_X = 1$ TeV (top right), and $m_X = 10$ TeV (bottom left); and in the (m_X, σ_{Xn}) plane for $m_{A'} = 100$ MeV (bottom right). The dark sector fine-structure constant α_X is set by requiring $\Omega_X \simeq 0.23$. Solid curves are for the dark sector mass splitting $\Delta = 100$ keV, while dashed curves are for $\Delta = 10$ keV. The indirect detection reach is also compared to other probes. **Green:** current bounds from direct detection with $\Delta = 0$ [101, 106]. **Blue:** rescaled bounds from direct detection. Solid curves are for $\Delta = 100$ keV, while dashed curves are for $\Delta = 10$ keV. **Gray:** regions probed by beam dump experiments, supernova observations, and BBN constraints [35, 128] (top and bottom left), and the neutrino floor (bottom right).

detailed analysis will be necessary to determine exactly the region of parameter space excluded by AMS, if indeed no dark sunshine signature is detected. However, these contours still provide useful information for weak scale secluded dark matter searches: the positron

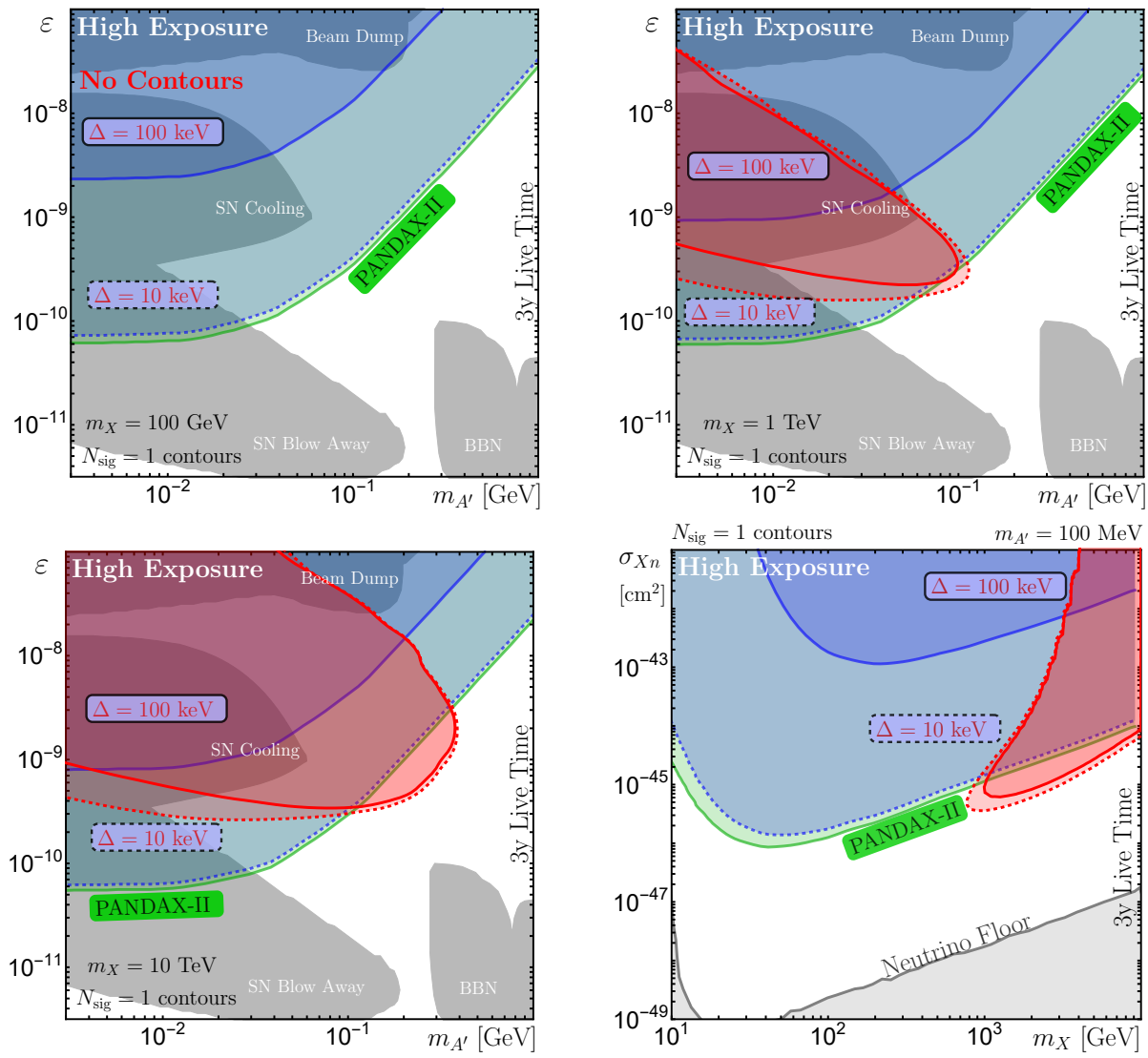

Figure 4.4: Same as Fig. 4.3 but with increased exposure $\xi_\odot^{\rm high} = 80\xi_\odot$. Note that the reach for $m_X = 100$ GeV dark matter vanishes at AMS-02. This is because our angular and energy cuts, set by the condition that we expect only one background event, restrict the amount of signal positrons to be negligibly small. The positron background drops off at higher energies, so that a search for more massive dark matter does not suffer the same reduction in expected signal rate.

background at AMS-02 drops quickly at higher energies, to the extent that the expected number of background positrons of energy greater than 1 TeV is negligible. A single energetic positron observed from the direction of the Sun can therefore be very significant. For $m_X = 10$ TeV then, the $N_{\rm sig} = 1$ contours characterize AMS-02's reach region, while higher event numbers are required to claim discovery at lower energies with accordingly higher

backgrounds.

More charitable assumptions yield accordingly more optimistic results: following our analyses in [6], we present the expected reach region for a hypothetical experiment with a higher exposure than AMS-02 in Fig. 4.4. If a detector with the same technical specifications and livetime as AMS-02 were placed near the Earth in such a fashion as to always face the Sun, perhaps at Lagrange Point 1, its exposure $\xi_{\odot}^{\text{high}}$ would be greater than the current exposure of AMS-02 by a factor of 80 [136]. In the formulae presented in Sec. 4.5 this is accomplished by setting $T = 240$ yr.

We also present the AMS-02 reach regions in the case where the magnetic field deflections are ignored in Fig. 4.5. Such a signal region may be viable with an improved understanding and mapping of the interplanetary magnetic field. Note that while the search regions for $m_X = 100$ GeV and 1 TeV grow substantially as compared to the regions presented in Fig. 4.3, the $m_X = 10$ TeV region does not perceptibly change. This is easy to understand: as the dark matter mass increases, the dark photons produced in dark matter annihilation are accordingly more energetic. These highly boosted dark photons are more likely to decay to produce more energetic positrons, which experience less deflection in the solar magnetic field so that P_{det}^{B} is negligible.

4.7 Conclusions

In previous work, we presented a novel method to discover a self-interacting elastic dark sector whose dark photon kinetically mixes with the SM photon. Dark matter is captured by the Sun and annihilates to dark photons, which furnish an indirect detection signature when they decay to e^+e^- pairs. For dark matter masses above 1 TeV this signature benefits from reduced astrophysical background. In spite of the low background, the signal region from

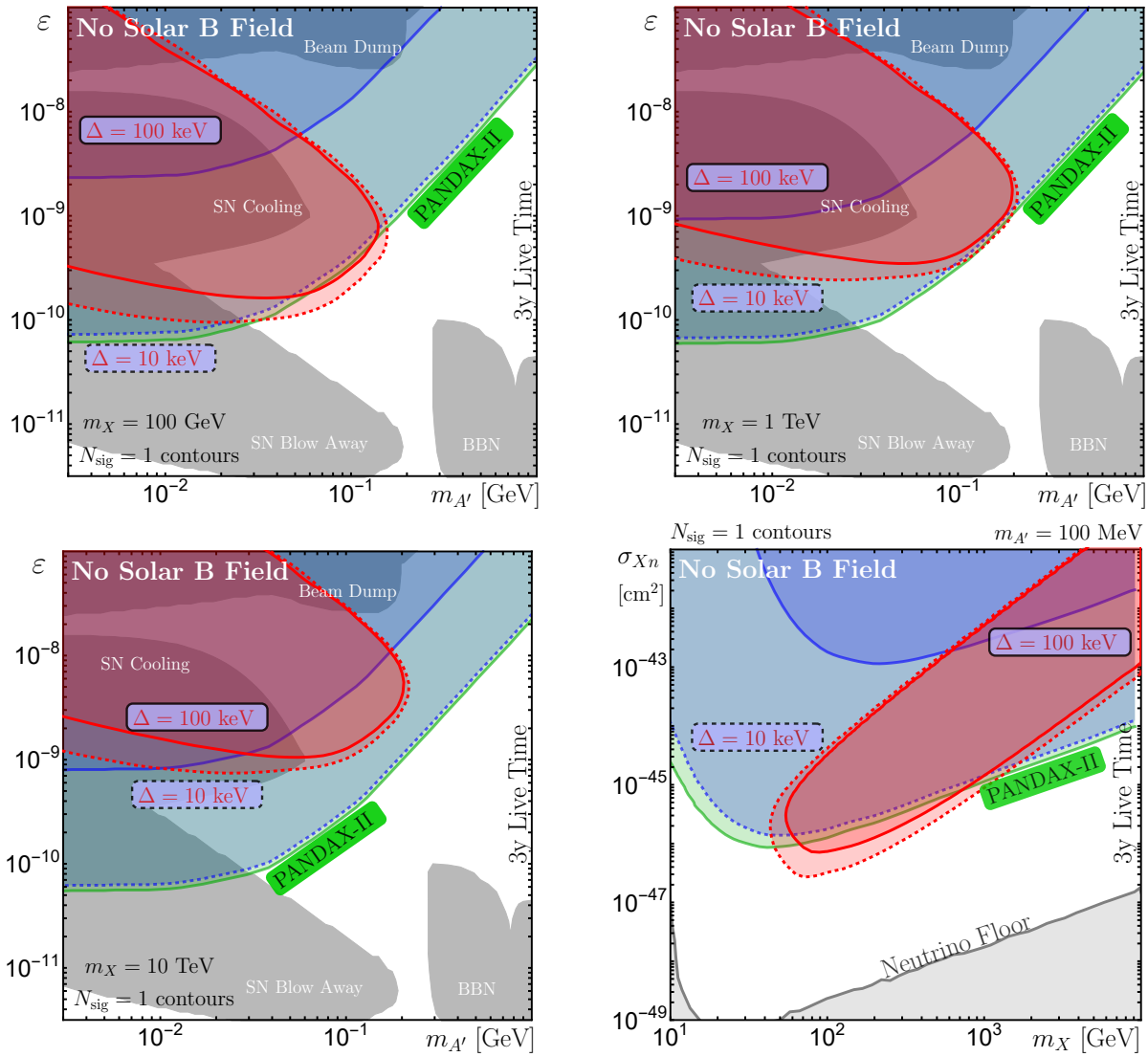

Figure 4.5: Same as Figures Figs. 4.3 and 4.4 but using the naive flux based estimate where magnetic deflections are ignored.

previous analysis was largely excluded by independent bounds from dark matter searches at PANDAX-II.

In this manuscript we have extended our earlier work to examine a dark sector consisting of two nearly-degenerate states coupling inelastically to a dark photon that mediates interactions with the Standard Model. Such a model benefits from weakened direct detection constraints and is well-motivated by small scale structure observations. Relative to the previously considered elastic case, we found that the inelastic dark matter capture rate is

only mildly suppressed and the non-perturbative Sommerfeld enhancement agrees with the elastic case, while the detection efficiencies are completely unchanged. As such, the region of parameter space over which the Sun is in equilibrium shrinks, but the region accessible to a dark sunshine search is largely determined by the detection efficiencies and thus is nearly unaffected. In contrast, direct detection bounds from LUX are relaxed by about an order of magnitude in ε. This leaves a region of parameter space: 1 TeV $\lesssim m_X \lesssim$ 10 TeV, $\Delta \sim$ 100 keV, 10 MeV $\lesssim m_{A'} \lesssim$ 100 MeV, and $10^{-10} \lesssim \varepsilon \lesssim 10^{-8}$, that is unprobed by supernova observations and fixed target dark photon searches, and favored to resolve small scale structure problems [144], where an inelastic dark sector may still be discovered or excluded using existing experiments and data. Finally, we provided estimates of the parameter space accessible to potential future experiments.

Chapter 5

Relic Density of a Resonant Dark Photon

The following is based on a previously published paper by the author and Jonathan L. Feng [2].

Notation change: In this chapter we use ϵ to denote the dimensionless collision energy of a dark matter annihilation reaction. To avoid confusion with the kinetic mixing parameter ε used elsewhere in this text, we will denote the parameter by κ throughout this chapter.

5.1 Introduction

The dark matter relic density is $\Omega_X h^2 = 0.1199 \pm 0.0022$, where Ω_X is the energy density of dark matter in units of the critical density, and $h \simeq 0.67$ is the reduced Hubble parameter [160]. As discussed in Chapter 1, because the relic density is an important quantity and so precisely known, or perhaps because so little else is known about dark matter, scenarios in which dark matter is produced through a simple mechanism that gives the correct Ω_X attract special attention. In particular, dark matter that begins in thermal equilibrium with the standard model and then freezes out with the correct thermal relic density is often considered especially well motivated. Examples include weakly-interacting massive particles (WIMPs), weak-scale particles with weak interactions, and WIMPless dark matter [161], hidden sector particles that are lighter and more weakly-coupled than WIMPs (or heavier and more strongly-coupled than WIMPs), but nevertheless also have the correct thermal relic abundance. For both WIMP and WIMPless dark matter, the region of parameter space that yields the correct thermal relic density, often known as the "thermal target," provides a useful goal for current and proposed experimental searches.

Dark photon models [34, 29, 162, 163] are a simple and elegant realization of the WIMPless possibility. Dark photons A' are light gauge bosons that have coupling g_X to dark matter X in the hidden sector and couplings κq_f to standard model particles f, where κ is the kinetic mixing parameter (elsewhere denoted as ε), and q_f is the electric charge of f. The dark matter's relic density is determined by the annihilation process $XX \to A' \to \text{SM}$, and for particular choices of m_X, $m_{A'}$, g_X, and κ, this annihilation process yields the correct thermal relic density.

Typically, one considers $g_X \sim 1$ and $\kappa \ll 1$, where κ is assumed to be suppressed, because it is generated at loop level. The dark photon scenario then splits into two cases. If $m_{A'} < 2m_X$, dark photons always decay to the visible (standard model) sector. In this case, dark photons

are produced at accelerators through their interactions with standard model particles and decay back to standard model particles. They mediate a new force, a revolutionary discovery in and of itself, but their implications for dark matter are not directly probed by accelerator experiments.

If $m_{A'} > 2m_X$, however, dark photons produced at accelerators typically decay invisibly to the hidden sector through $A' \to XX$. In this case, experiments that produce dark photons also produce dark matter, and the signature is missing mass, energy, or momentum. Of course, there is a long road ahead to identify the missing particle with the dark matter that permeates the universe, but at least in this case, the underlying process involves a dark matter candidate. The number and variety of experiments that are potentially sensitive to invisibly-decaying dark photons is staggering. They include BaBar [164, 165], CRESST II [166], E137 [167, 168], LSND [169, 170, 171, 168], and NA64 [172], which currently bound various regions of parameter space, and BDX [173, 174, 168], Belle II [175], COHERENT [176, 177], DarkLight [178], LDMX [179], MiniBoone [170, 171, 180, 168], MMAPS [181], NA64 [182], PADME [183, 184], SHiP [185, 186], SBNe/SBNπ [187, 188], and VEPP-3 [189], which will probe this scenario in the future. The promise of discovering a portal to the dark sector in these experiments is significant, especially in the case of LDMX, which has been projected to probe all of the thermal target region for MeV $< m_X \lesssim$ GeV, $m_{A'} \gtrsim 3m_X$, and $g_X \sim 1$ [190]. In addition, a large number of direct detection experiments, which we discuss below, although not creating real dark photons, also probe these scenarios through $X\,\mathrm{SM} \to X\,\mathrm{SM}$ mediated by a t-channel A', where the $A'XX$ interaction is the same one that mediates the dark photon's invisible decays.

The invisible decay case with $m_{A'} > 2m_X$ is, however, also the "half" of parameter space in which dark matter annihilation may be resonantly enhanced. This has been noted previously, for example, in Ref. [190] (see, in particular, the supplementary material), but the impact of the A' resonance has not been investigated in detail. For degeneracies $0 < m_{A'} - 2m_X \lesssim T_f$,

where T_f is the temperature at freezeout, the kinetic energy of dark matter particles can put the annihilation process $XX \to A' \to$ SM on resonance. As we will see, for $\sim 10\%$ degeneracies between $m_{A'}$ and $2m_X$, this resonance may have an extraordinary effect. For example, for scalar dark matter, the resonance generically raises the thermally-averaged annihilation cross section by four orders of magnitude. To compensate this kinematic enhancement, the thermal relic density may be corrected by lowering κ^2 by four orders of magnitude, but the resulting thermal target region of parameter space is then beyond the reach of any proposed accelerator experiment. Greater degeneracies move the thermal target to even weaker couplings.

In the following sections, we consider dark photon models with both scalar and pseudo-Dirac dark matter, estimate the effect of the resonance analytically, and present numerical results for the impact of the resonance on the thermal target region for a wide range of mass degeneracies.

5.2 Dark Photon Model

We use the same model of kinetic mixing as in previous chapters, but with more general dark sectors. The SM-dark photon Lagrangian is given by

$$\mathcal{L} = -\frac{1}{4}F_{\mu\nu}F^{\mu\nu} - \frac{1}{4}F'_{\mu\nu}F'^{\mu\nu} + \frac{1}{2}m_{A'}^2 A'^2 + \sum_f \bar{f}(i\,\partial\!\!\!/ - eq_f A\!\!\!/ - \kappa eq_f A\!\!\!/' - m_f)f \ , \tag{5.1}$$

where $F_{\mu\nu}$ and $F'_{\mu\nu}$ are the field strengths of the photon A and dark photon A', respectively, $m_{A'}$ is the dark photon's mass, κ is the kinetic mixing parameter (we reserve ϵ for another quantity below), and f are standard model fermions with electric charges q_f and masses m_f.

The hidden sector also contains the dark matter. We will consider both complex scalar [162] and pseudo-Dirac dark matter [142, 141, 168]. For the scalar case, the dark matter La-

grangian is

$$\mathcal{L}_\phi = \left|(\partial_\mu + i g_X A'_\mu)\phi\right|^2 - m_\phi^2 \left|\phi\right|^2 \ , \tag{5.2}$$

where ϕ is the scalar dark matter particle with mass m_ϕ, and $g_X = \sqrt{4\pi\alpha_X}$ is the hidden sector gauge coupling. In this case, the invisble (hidden sector) decay width is

$$\Gamma_\phi \equiv \Gamma(A' \to \phi\phi) = \frac{g_X^2 m_{A'}}{48\pi}\left[1 - \left(\frac{2m_\phi}{m_{A'}}\right)^2\right]^{3/2} . \tag{5.3}$$

For the pseudo-Dirac case, we consider a dark photon that couples to two hidden Weyl fermions that have a Dirac mass and small, identical Majorana masses. In the mass basis, the resulting dark matter Lagrangian is

$$\mathcal{L}_\chi = \sum_{i=1,2} \bar{\chi}_i (i\,\partial\!\!\!/ - m_i)\chi_i - (g_X \bar{\chi}_2 A\!\!\!/' \chi_1 + \text{h.c.}) \ , \tag{5.4}$$

where the two fermions χ_1 and χ_2 couple non-diagonally to the dark photon and have masses m_1 and m_2, respectively, with a small mass splitting $\Delta \equiv m_2 - m_1$. Below we will typically refer to χ_1 as the dark matter particle X with mass m_X and to χ_2 as the excited state with mass $m_X + \Delta$. In this pseudo-Dirac case, the invisible, hidden sector decay width is

$$\Gamma_\chi \equiv \Gamma(A' \to \chi_1\chi_2) = \frac{g_X^2 m_{A'}}{12\pi}\left[1 - \left(\frac{2m_X + \Delta}{m_{A'}}\right)^2\right]^{1/2}\left[1 + \frac{(2m_X+\Delta)^2}{2m_{A'}^2}\right]\left[1 - \frac{\Delta^2}{m_{A'}^2}\right]^{3/2} . \tag{5.5}$$

5.3 Relic Densities Near Resonance: Analytic Estimate

The formalism for treating dark matter annihilation near a resonance was developed long ago [21, 153]. In this section, we follow the method of Ref. [21] to derive a simple analytic estimate for the effect of a resonance on the thermal relic density for $\sim 10\%$ degeneracies. In Sec. 5.4, we will refine the standard treatment to improve its validity off resonance. We then use these results to derive more precise numerical results for cases with both more and less degeneracy, which we present in Sec. 5.5.

The thermal relic abundance of a dark matter particle X is

$$\Omega_X h^2 = 8.77 \times 10^{-11}\ \mathrm{GeV}^{-2} \left[\overline{g_{\mathrm{eff}}^{1/2}} \int_{x_f}^{x_0} \frac{\langle \sigma v \rangle}{x^2} dx \right]^{-1} , \tag{5.6}$$

where $\langle \sigma v \rangle$ is the thermally-averaged annihilation cross section, $x_0 = m_X/T_0 = 4.26 \times 10^{12}\ (m_X/\mathrm{GeV})$, T_0 is the temperature now, and $x_f = m_X/T_f$, where T_f is the freezeout temperature. The freezeout temperature is found by solving the equation

$$\frac{63 \times 5^{1/2} x_f^{-1/2} e^{-x_f} g}{32\pi^3} \frac{g_{\mathrm{eff}}^{1/2}(x_f)}{h_{\mathrm{eff}}(x_f)} m_X m_{\mathrm{Pl}} \langle \sigma v \rangle = 1 \ . \tag{5.7}$$

In these equations, $g_{\mathrm{eff}}(x)$ and $h_{\mathrm{eff}}(x)$ are the effective numbers of degrees of freedom for energy and entropy density, respectively, $\overline{g_{\mathrm{eff}}^{1/2}}$ is the typical value of $g_{\mathrm{eff}}(x)$ between x_0 and x_f, and g is the number of X spin degrees of freedom.

To determine the thermal relic density, then, we must determine $\langle \sigma v \rangle$. In this section, we consider the simple case where the dark matter annihilates through the dark photon

resonance $XX \to A' \to$ SM. For this case, it is convenient to define

$$s_0 \equiv 4m_X^2 \tag{5.8}$$

$$\epsilon \equiv (s - s_0)/s_0 \tag{5.9}$$

$$\epsilon_R \equiv (m_{A'}^2 - s_0)/s_0 \tag{5.10}$$

$$\gamma_R \equiv m_{A'}\Gamma_{A'}/s_0 \ , \tag{5.11}$$

where ϵ, ϵ_R, and γ_R are dimensionless quantities that represent the kinetic energy of the collision, the kinetic energy required to be on resonance, and the width of the resonance, respectively. With a slight abuse of notation, in cases where it matters, for example, for the very small values of ϵ_R that we will consider below, these definitions should be considered to be in terms of physical quantities rather than Lagrangian parameters, so, for example, loop corrections have been included in the masses in Eqs. (5.8)–(5.11).

In general, $\langle \sigma v \rangle$ must be evaluated numerically, but the formalism simplifies greatly with three approximations. First, if the dark matter freezes out while non-relativistic, $x_f \equiv m_X/T_f \gg 1$, the thermally-averaged annihilation cross section is approximately [21]

$$\langle \sigma v \rangle_{\rm NR} = \frac{2x^{3/2}}{\pi^{1/2}} \int_0^\infty \sigma v_{\rm lab} \epsilon^{1/2} e^{-x\epsilon} d\epsilon \ , \tag{5.12}$$

where σ is the annihilation cross section, and

$$v_{\rm lab} = \frac{2\epsilon^{1/2}(1+\epsilon)^{1/2}}{1+2\epsilon} \tag{5.13}$$

is the relative velocity of the incoming particles in the rest frame of one of them. We have verified that $x_f \sim 15$ and the non-relativistic approximation is valid to $\sim 10\%$ throughout the regions of parameter space we consider.

Second, if we are sufficiently near the A' resonance, so $x_f \epsilon_R \lesssim 1$ or $m_{A'} - 2m_X \lesssim m_X/x_f$,

we may take σ to have the Breit-Wigner form

$$\sigma_{\rm BW} = \frac{4\pi\omega}{p^2} B_i B_f \frac{m_{A'}^2 \Gamma_{A'}^2}{(s - m_{A'}^2)^2 + m_{A'}^2 \Gamma_{A'}^2} = \frac{4\pi\omega}{m_X^2 \epsilon} B_i B_f \frac{\gamma_R^2}{(\epsilon - \epsilon_R)^2 + \gamma_R^2} \ , \tag{5.14}$$

where $\omega = (2S_{A'} + 1)/(2S_X + 1)^2$, $S_{A'} = 1$ is the dark photon's spin, S_X is the dark matter's spin, and $B_i = B(A' \to XX)$ and $B_f = 1 - B_i = B(A' \to \text{SM})$ are the branching fractions to the hidden and visible sectors, respectively.

Third, if the dark photon's couplings are sufficiently weak, so $\gamma_R \ll 1$ or $\Gamma_{A'} \ll m_{A'}$, we may use the narrow width approximation and the Breit-Wigner cross section becomes a delta function. In the numerical analysis described below in Sec. 5.5, we have verified that, even for large $\alpha_X \sim 0.5$, the narrow width approximation gives thermally-averaged cross sections that are in agreement with the full result at the 10% level for $\epsilon_R \sim 0.1$, improving to 1% agreement for $\epsilon_R \lesssim 0.01$.

Given these three simplifications, the thermally-averaged annihilation cross section near a resonance at freezeout is [21]

$$\langle \sigma v \rangle_{\rm res} \approx \frac{16\pi^{3/2}\omega}{m_X^2} x_f^{3/2} \gamma_R B_i B_f \frac{(1+\epsilon_R)^{1/2}}{1+2\epsilon_R} e^{-x_f \epsilon_R} \tag{5.15}$$

$$\approx \frac{16\pi^{3/2}\omega}{m_X^2} x_f^{3/2} \frac{\Gamma_{A'}}{2m_X} B_i B_f e^{-x_f \epsilon_R} \ , \tag{5.16}$$

where in the last step we have used the fact that $x_f \sim 20$, and so the "near resonance" assumption implies $\epsilon_R \ll 1$. Since we are considering invisible decay scenarios, $B_i \approx 1$. We may also write $\Gamma_{A'} B_f = \Gamma_f \equiv N_f \kappa^2 e^2 m_X / 12\pi$, where N_f is the effective number of kinematically accessible standard model decay channels. We then find that

$$\langle \sigma v \rangle_{\rm res} \approx \frac{2\pi^{1/2}\omega}{3m_X^2} x_f^{3/2} \kappa^2 e^2 N_f e^{-x_f \epsilon_R} \ . \tag{5.17}$$

In the absence of resonances, assuming $m_X \sim m_{A'}$, the typical value for the thermally-averaged annihilation cross section is

$$\langle \sigma v \rangle_{\text{non-res}} \sim \frac{\pi \kappa^2 \alpha \alpha_X}{m_X^2} \frac{1}{x_f^L} = \frac{\kappa^2 e^2 g_X^2}{16\pi m_X^2} \frac{1}{x_f^L} \ , \tag{5.18}$$

where $L = 0$ (1) for s-wave (p-wave) annihilation. The nearby resonance therefore enhances the thermally-averaged annihilation cross section by a factor

$$\frac{\langle \sigma v \rangle_{\text{res}}}{\langle \sigma v \rangle_{\text{non-res}}} \sim \frac{32\pi^{3/2} \omega N_f}{3 g_X^2} x_f^{3/2} x_f^L e^{-x_f \epsilon_R} \sim 5{,}000 \ \frac{\omega N_f x_f^L e^{-x_f \epsilon_R}}{g_X^2} \ . \tag{5.19}$$

We see that a resonance may enhance the annihilation cross section (and suppress the thermal relic density) by four (two) orders of magnitude for the case of p-wave (s-wave) annihilators when $m_{A'}$ and $2m_X$ are degenerate to $\sim 10\%$.

This conclusion for the thermal relic density assumes $\Omega_X h^2 \sim \langle \sigma v \rangle^{-1}$, as typically follows from Eq. (5.6). This is valid for the $\sim 10\%$ degeneracies discussed here, but as we will see in Sec. 5.5, for even greater degeneracies $\epsilon_R \ll 0.1$, there are additional effects that enhance the resonance effect further.

5.4 Relic Densities Near Resonance: Numerical Analysis

In this section, we present our method for numerically evaluating the thermal relic density near resonance. Our numerical results assume dark matter is non-relativistic at freezeout, but unlike the analytic estimate of Sec. 5.3, do not assume the resonance is nearby and do not assume the narrow-width approximation. In addition, we present results for both the scalar case and the pseudo-Dirac case. The method is a generalization of the treatment

presented in Ref. [21].

The contribution of an s-channel resonance to the dark matter annihilation cross section can always be written in the form

$$\sigma v_{\rm lab} = F(\epsilon)\frac{m_{A'}\Gamma_{A'}}{(s-m_{A'}^2)^2+m_{A'}^2\Gamma_{A'}^2} \ , \tag{5.20}$$

where $v_{\rm lab}$ is given in Eq. (5.13) and the dimensionless analytic function $F(\epsilon)$ encodes the cross section's dependence on the dimensionless kinetic energy $\epsilon \equiv (s-s_0)/s_0$, where $s_0 = 4m_X^2$ in the scalar case and $s_0 = (2m_X+\Delta)^2$ in the pseudo-Dirac case.

We can then exploit a special function to describe the terms of a partial cross section expansion in a compact and numerically well-described manner. In the non-relativistic thermal average

$$\langle \sigma v\rangle_{\rm NR} = \frac{2x^{3/2}}{\pi^{1/2}}\int_0^\infty \sigma v_{\rm lab}\epsilon^{1/2}e^{-x\epsilon}d\epsilon \ , \tag{5.21}$$

we rewrite the integral as

$$\int_0^\infty \frac{1}{s_0}{\rm Re}\left[\frac{i}{\epsilon_R+i\gamma_R-\epsilon}F(\epsilon)\epsilon^{1/2}e^{-x\epsilon}\right]d\epsilon \ . \tag{5.22}$$

Substituting the Taylor expansion $F(\epsilon) = \sum_{\ell=0}^\infty F^{(\ell)}\epsilon^\ell/\ell!$, we find

$$\langle \sigma v\rangle_{\rm NR} = \frac{2x^{3/2}\pi^{1/2}}{s_0}\sum_{\ell=0}^\infty \frac{F^{(\ell)}}{\ell!}{\rm Re}\left[\frac{i}{\pi}\int_0^\infty \frac{\epsilon^{\ell+1/2}e^{-x\epsilon}}{z_R-\epsilon}d\epsilon\right] \ , \tag{5.23}$$

where $z_R \equiv \epsilon_R + i\gamma_R$. The s- and p-wave terms of the above expansion can be written compactly as

$$\begin{aligned}\langle \sigma v\rangle_{\rm NR} \ \approx \ & \frac{2x^{3/2}\pi^{1/2}}{s_0}\Big\{F^{(0)}{\rm Re}\left[z_R^{1/2}w(x^{1/2}z_R^{1/2})\right] \\ & +F^{(1)}\left(\gamma_R\pi^{-1/2}x^{-1/2}+{\rm Re}\left[z_R^{3/2}w(x^{1/2}z_R^{1/2})\right]\right)\Big\} \ ,\end{aligned} \tag{5.24}$$

where

$$w(z) \equiv \frac{2iz}{\pi} \int_0^\infty \frac{e^{-t^2}}{z^2 - t^2} dt = e^{-z^2} \left(1 + \frac{2i}{\sqrt{\pi}} \int_0^z e^{t^2} dt \right) \tag{5.25}$$

is the Faddeeva function. The first form in Eq. (5.25) is useful to derive Eq. (5.24), and the second form can be used to evaluate the function numerically and efficiently. In this work, numerical calculations were performed with the SciPy library [191] using the method of Ref. [192] to evaluate the Faddeeva function close to the real axis.

We now turn to the specific models we consider in this paper. For the case of scalar X annihilating to standard model final states through $XX \to A' \to \text{SM}$, the cross section takes the form

$$\sigma v_{\text{lab}} = \frac{16\pi\kappa^2\alpha\alpha_X}{3\left((s - m_{A'}^2)^2 + m_{A'}^2\Gamma_{A'}^2\right)} \frac{\epsilon\left[m_e^2 + 2(1+\epsilon)m_X^2\right]\sqrt{1+\epsilon - m_e^2/m_X^2}}{(1+2\epsilon)\sqrt{1+\epsilon}\; B_e(2m_X\sqrt{1+\epsilon})} \;, \tag{5.26}$$

which implies

$$F(\epsilon) = \frac{16\pi\kappa^2\alpha\alpha_X}{3m_{A'}\Gamma_{A'}} \frac{\epsilon\left[m_e^2 + 2(1+\epsilon)m_X^2\right]\sqrt{1+\epsilon - m_e^2/m_X^2}}{(1+2\epsilon)\sqrt{1+\epsilon}\; B_e(2m_X\sqrt{1+\epsilon})} \;. \tag{5.27}$$

This cross section is p-wave suppressed, as indicated by the leading factor of ϵ. We therefore know that $F^{(0)}$ vanishes, and we can verify that

$$F^{(1)} = \frac{16\pi\kappa^2\alpha\alpha_X}{3m_{A'}\Gamma_{A'}} \frac{(m_e^2 + 2m_X^2)\sqrt{1 - m_e^2/m_X^2}}{B_e(2m_X)} \;. \tag{5.28}$$

Given this, the thermally-averaged cross section is given by Eq. (5.24), and the thermal relic density and freezeout temperature can be determined by Eqs. (5.6) and (5.7).

For the pseudo-Dirac case, the cross section for annihilation through $\chi_1\chi_2 \to A' \to \text{SM}$ is

$$\begin{aligned}\sigma v_{\text{lab}} = &\frac{4\pi\kappa^2\alpha\alpha_X}{3s_0\left[(s-m_{A'}^2)^2+m_{A'}^2\Gamma_{A'}^2\right]} \\ &\times \frac{(3+2\epsilon)\left[(1+\epsilon)s_0+2m_e^2\right]\left[s_0(1+\epsilon)-4m_e^2\right]^{1/2}\left[s_0(1+\epsilon)-\Delta^2\right]^{1/2}}{(1+\epsilon)(1+2\epsilon)\ B_e(\sqrt{s_0(1+\epsilon)})}\ ,\end{aligned} \tag{5.29}$$

which implies

$$F(\epsilon) = \frac{4\pi\kappa^2\alpha\alpha_X}{3s_0 m_{A'}\Gamma_{A'}}\frac{(3+2\epsilon)\left[(1+\epsilon)s_0+2m_e^2\right]\left[s_0(1+\epsilon)-4m_e^2\right]^{1/2}\left[s_0(1+\epsilon)-\Delta^2\right]^{1/2}}{(1+\epsilon)(1+2\epsilon)\ B_e(\sqrt{s_0(1+\epsilon)})}\ . \tag{5.30}$$

This is an s-wave cross section, and it is easy to read off the constant term in the Taylor expansion of F:

$$F^{(0)} = \frac{4\pi\kappa^2\alpha\alpha_X}{s_0 m_{A'}\Gamma_{A'}B_e(\sqrt{s_0})}(s_0+2m_e^2)(s_0-4m_e^2)^{1/2}(s_0-\Delta^2)^{1/2}\ . \tag{5.31}$$

This determines the leading contribution to the thermally-averaged cross section through Eq. (5.24).

There is an additional complication in the pseudo-Dirac case: when the dark sector consists of multiple nearly-degenerate species, we must include coannihilation factors in the thermally-averaged cross section [153] and the freezeout condition. The effective thermally-averaged cross section is

$$\langle\sigma v\rangle_{\text{eff}} = \frac{2(1+\Delta/m_X)^{3/2}e^{-x\Delta/m_X}}{\left[1+(1+\Delta/m_X)^{3/2}e^{-x\Delta/m_X}\right]^2}\langle\sigma v\rangle_{\text{NR}}\ . \tag{5.32}$$

The freezeout condition is modified to

$$\frac{63\times 5^{1/2}x_f^{-1/2}e^{-x_f}g}{32\pi^3}\frac{g_{\text{eff}}^{1/2}}{h_{\text{eff}}}m_X m_{\text{Pl}}\left[1+\left(1+\frac{\Delta}{m_X}\right)^{3/2}e^{-x_f\Delta/m_X}\right]\langle\sigma v\rangle_{\text{eff}} = 1\ , \tag{5.33}$$

and the relic abundance is given by

$$\Omega_X h^2 = 8.77 \times 10^{-11}\ \mathrm{GeV}^{-2} \left[\overline{g_{\mathrm{eff}}^{1/2}} \int_{x_f}^{x_0} \frac{\langle \sigma v \rangle_{\mathrm{eff}}}{x^2} dx \right]^{-1} . \tag{5.34}$$

5.5 Results

We present here the results of our analysis using the formalism of Sec. 5.4. Thermal relic contours for the benchmark, near-maximal perturbative value of the dark fine structure constant $\alpha_X = 0.5$ are shown in Fig. 5.1 for various values of ϵ_R. The contours for the non-degenerate case $\mathrm{m}_{A'} = 3m_X$ agree within $\sim 10\%$ with those presented previously for scalar [190] and pseudo-Dirac [168] dark matter, which are shown as dotted curves. The minor discrepancy is due to a $\sim 10\%$ difference between the thermally-averaged cross section in the non-relativistic approximation used here and the relativistic thermally-averaged cross section used in Refs. [190, 168] at freeze-out temperatures near $x_f = 15$. For the degenerate case $\epsilon_R = 0.1$, as expected given the analytic estimate of Sec. 5.3, the thermal targets for scalar (pseudo-Dirac) dark matter move to values of κ^2 that are four (two) orders of magnitude lower, relative to the $\mathrm{m}_{A'} = 3m_X$ non-degenerate case.

The gray shaded regions in Fig. 5.1 are excluded by various combinations of current constraints from BaBar [164, 165], CRESST II [166], E137 [167, 168], LSND [169, 170, 171, 168], and NA64 [172]. The CRESST II bounds are not applicable to pseudo-Dirac dark matter with $\Delta = 0.1\, m_X$, while exclusions from non-observation of excited state decays $\chi_2 \to \chi_1 e^+ e^-$ at E137 and LSND [168] apply only to pseudo-Dirac dark matter with $\Delta > 2m_e$. Observations of the CMB [160] exclude thermal relic Majorana dark matter below the 10 GeV mass range [73], but we include in Fig. 5.1 the resonant thermal targets for $\Delta = 0$ to illustrate the effect of a nonzero mass splitting. Note the thermal targets' stronger dependence on ϵ_R for smaller values of Δ. Also included in Fig. 5.1 are the projected sensitivities of planned

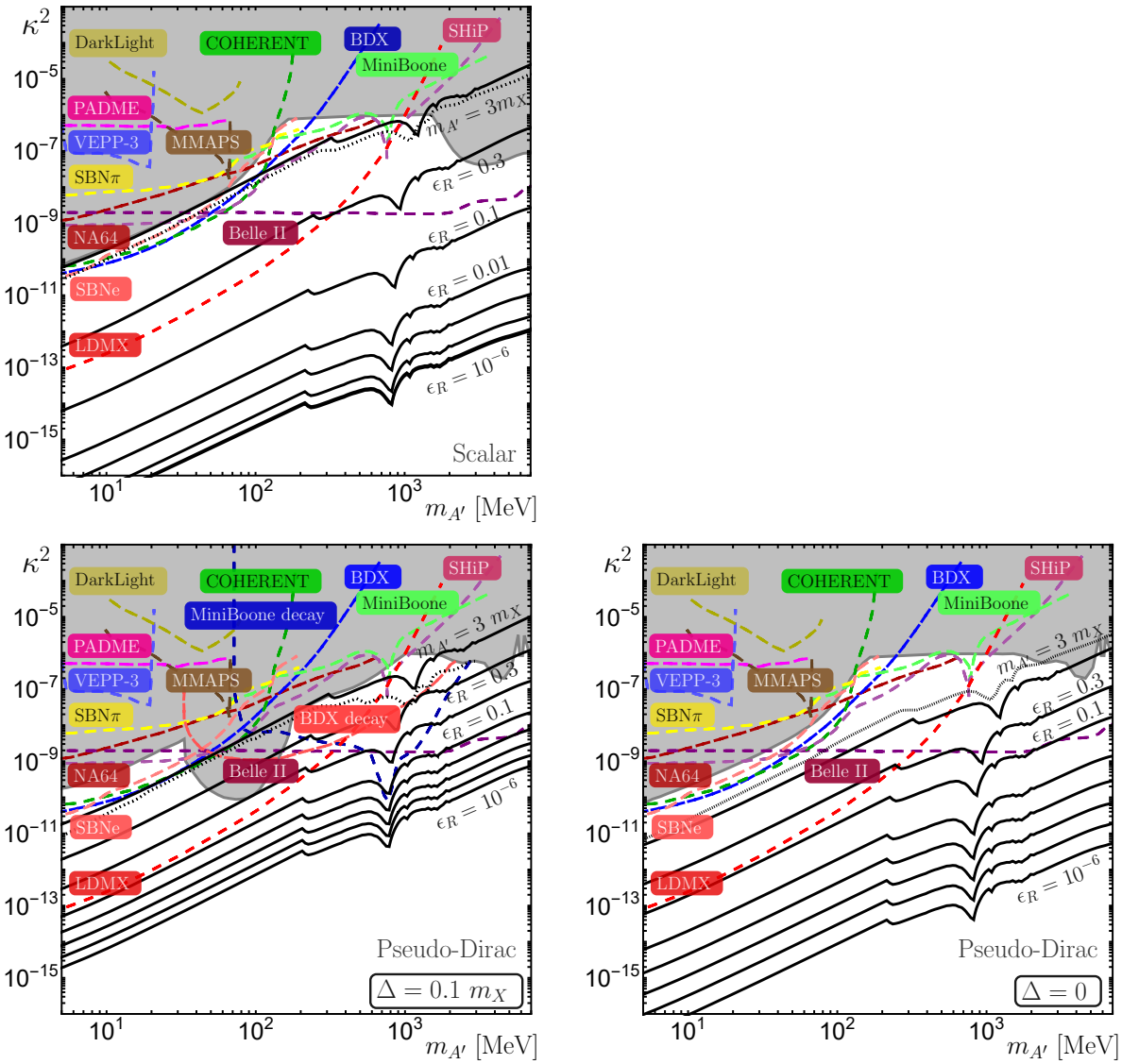

Figure 5.1: **Thermal targets and accelerator search experiments.** SOLID BLACK CONTOURS: Thermal target contours in dark photon parameter space $(m_{A'}, \kappa^2)$ for $\alpha_X = 0.5$ in the non-degenerate cases with $m_{A'} = 3m_X$ and $\epsilon_R \equiv (m_{A'}^2 - 4m_X^2)/(4m_X^2) = 0.3$, and in the degenerate cases with $\epsilon_R = 10^{-n}$, where $n = 1, 2, \ldots 6$. In the scalar case (TOP) the thermal relic contours reach a floor near $\epsilon_R = 10^{-6}$, where the thermal relic abundance requirement becomes inconsistent with the requirement that the dark photon decay is dominantly invisible. The $\epsilon_R = 10^{-5}$ contour is displayed in this plot, but is close enough to the $\epsilon_R = 10^{-6}$ contour that they appear to overlap. In the pseudo-Dirac case (BOTTOM) the thermal relic contours extend to arbitrarily low values of κ^2 with appropriate choice of ϵ_R, but we display only a small number of contours to avoid clutter. In the BOTTOM LEFT panel, the mass splitting is $\Delta = 0.1\, m_X$, and these models evade direct detection bounds. In the BOTTOM RIGHT panel, $\Delta = 0$, which illustrates the effect of decreasing Δ on the thermal target regions. DOTTED BLACK CONTOURS: Thermal target contours for $m_{A'} = 3m_X$ from relativistic treatments of freeze-out for the scalar [190] and pseudo-Dirac [168] cases. GRAY SHADED: Regions excluded by current bounds (see text). DASHED CONTOURS: Projected reaches of proposed dark photon and dark matter accelerator searches (see text).

accelerator-based dark photon and dark matter searches at BDX [173, 174, 168], Belle II [175], COHERENT [176, 177], DarkLight [178], LDMX [179], MiniBoone [170, 171, 180, 168], MMAPS [181], NA64 [182], PADME [183, 184], SHiP [185, 186], SBNe/SBNπ [187, 188], and VEPP-3 [189]. The excluded regions and future sensitivities assume $m_{A'} = 3m_X$. For comparison with the degenerate case contours with $m_{A'} \approx 2m_X$, these contours may be shifted up or down by $\mathcal{O}(1)$ factors. For a comprehensive overview of existing constraints and future experimental sensitivities, see Ref. [12].

Direct detection experiments can also probe these invisible dark photon scenarios. Although not searches for dark photons per se, they probe the $A'XX$ vertex that induces invisible A' decay through its role in inducing $X\,\mathrm{SM} \to X\,\mathrm{SM}$ scattering through a t-channel A'. To facilitate comparison with direct detection experiments, it is convenient [193, 194] to express the thermal relic parameter values in terms of

$$\bar{\sigma}_e = \frac{16\pi\mu_{X,e}^2 \alpha\kappa^2\alpha_X}{(m_{A'}^2 + \alpha^2 m_e^2)^2} \ , \tag{5.35}$$

where $\mu_{X,T}$ denotes the reduced mass of the dark matter-target system with $T = e$, nucleon, or nucleus. For the case of Majorana dark matter, the definition of $\bar{\sigma}_e$ includes an additional factor of $2(\mu_{X,T}^2/m_X^2)v_X^2$, where $v_X = 10^{-3}$ is the characteristic DM halo velocity.

In Fig. 5.2 we show the same thermal targets as in Fig. 5.1, but expressed in the $(m_X, \bar{\sigma}_e)$ parameter space and compared to current and proposed direct detection experiments. Fig. 5.2 includes current exclusions from XENON [195, 196], as well as projected regions of sensitivity [194, 195, 197, 198, 199, 200] for CYGNUS HD-10, DAMIC-1K [201, 202], NEWS, PTOLEMY-G3, SENSEI [203], SuperCDMS [204, 205], UA$'$(1), and future experiments based on GaAs scintillators [197] superconducting aluminum, superfluid helium [206, 207, 208, 209, 210], color center production [211, 212], magnetic bubble chambers [213], scintillating bubble chambers [214], and bremsstrahlung in inelastic DM-nucleus scattering [215, 216].

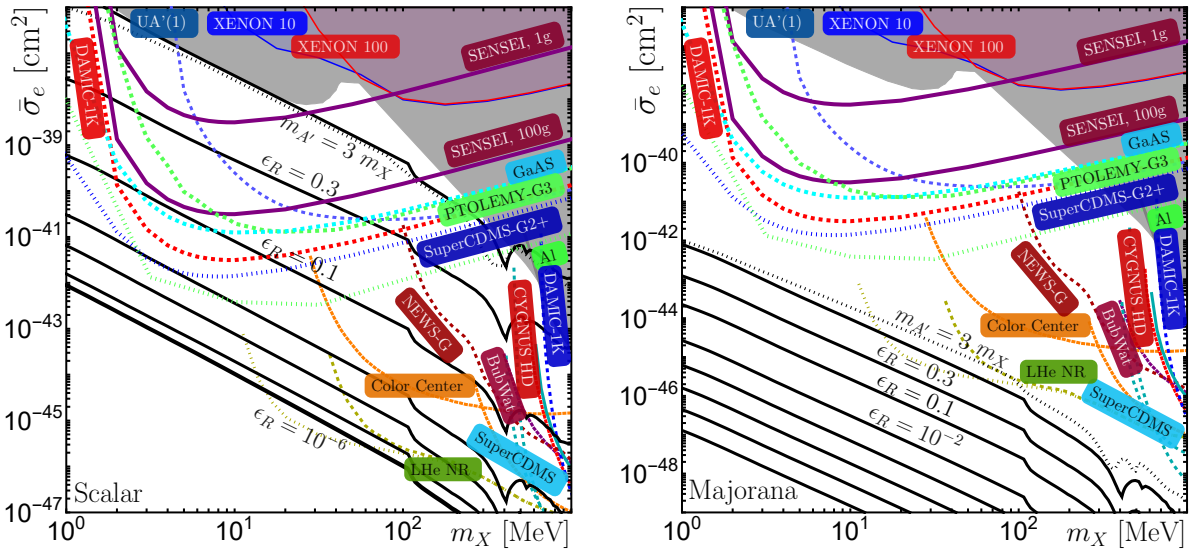

Figure 5.2: **Thermal targets and direct detection search experiments.** SOLID BLACK CONTOURS: Thermal target contours as in Fig. 5.1, but in the direct detection parameter space $(m_X, \bar{\sigma}_e)$, where $\bar{\sigma}_e = (16\pi\mu_{X,e}^2\alpha\kappa^2\alpha_X)/(m_{A'}^2 + \alpha^2 m_e^2)^2$ (see text). In the scalar case (LEFT) a resonantly annihilating thermal relic may still be within reach of future nuclear recoil experiments. In the RIGHT panel we show only the lines for Majorana DM-nuclear scattering, with $m_T = 0.936$ GeV; the thermal targets for DM-electron scattering scale approximately with the target mass squared, placing them far out of reach of current and proposed experiments. DOTTED BLACK CONTOURS: Relativistic thermal relic contours, as in Fig. 5.1. GRAY SHADED: Regions excluded by current bounds (see text). COLORED CONTOURS: Projected reaches of proposed direct detection experiments (see text).

Exclusions and regions of sensitivity for nuclear recoil experiments are converted into limits and projected sensitivities for $\bar{\sigma}_e$ using

$$\bar{\sigma}_e = 4\frac{\mu_{X,e}^2}{\mu_{X,N}^2}\sigma_N \ , \tag{5.36}$$

which makes it possible to compare the thermal targets and sensitivities of both electron and nuclear recoil experiments in the same parameter space. As in Fig. 5.1, the excluded regions and future sensitivities assume $m_{A'} = 3m_X$ and are reviewed in Ref. [12].

Comparing the thermal targets with the existing constraints and projected sensitivities, we see that for the scalar case and $\epsilon_R \sim 10\%$, the thermal target cannot be probed in any proposed accelerator or beam dump experiment. For the fermionic dark matter cases and

$\epsilon_R \sim 10\%$, the thermal target is also beyond the reach of all proposed accelerator-based experiments, with the exception of LDMX, for which it is at the border of sensitivity, and becomes very challenging for smaller mass splittings Δ. For direct detection experiments, the thermal target for moderate degeneracy $\epsilon_R \sim 10\%$ is still within the projected reach of some far future experiments in the scalar case, but is beyond all proposed experiments in the Majorana case.

We also show results for smaller values of ϵ_R in Fig. 5.1. For greater degeneracies, the thermal target region moves to even lower values of κ^2. For $\epsilon_R \sim 10^{-6}$, for example, the thermal targets are essentially beyond all proposed accelerator and direct detection experiments for both the scalar and fermionic dark matter cases.

At first sight, the extreme suppression of the preferred values of κ^2 might be surprising, since the thermally-averaged cross section, for example, in Eq. (5.17), becomes independent of ϵ_R for $x_f \epsilon_R \ll 1$. However, for very small ϵ_R, the dark matter continues to annihilate long after freezeout as the universe cools. This is accounted for by the integral in Eq. (5.6), and that integral is sensitive to ϵ_R, even it is very small.

To understand this behavior, it is convenient to use the narrow width approximation. In the case that $\Gamma_{A'} \ll m_{A'}$ we can write the generic resonant cross section as

$$\sigma v_{\rm lab} \approx \frac{\pi}{s_0} F(\epsilon) \delta(\epsilon - \epsilon_R) \ , \tag{5.37}$$

which yields for the thermal average

$$\langle \sigma v \rangle_{\rm NR} \approx \frac{2\pi^{1/2} x^{3/2}}{s_0} \epsilon_R^{1/2} F(\epsilon_R) e^{-x\epsilon_R} \ . \tag{5.38}$$

We notice that in both the scalar and pseudo-Dirac cases, as long as $\Gamma_{\rm SM} \ll \Gamma_\phi, \Gamma_\chi$ and $\epsilon_R \ll 1$, the quantity $F(\epsilon_R)$ scales like $\epsilon_R^{-1/2}$. Therefore the thermally-averaged cross section's

dependence on ϵ_R is contained entirely in the factor $\exp(-x\epsilon_R)$. This observation implies a simple relation between values of ϵ_R and κ that yield the correct relic abundance:

$$\Omega_X h^2 \propto \left[\int_{x_f}^{x_0} \frac{\kappa^2}{x^{1/2}} e^{-x\epsilon_R}\, dx\right]^{-1} \propto \frac{\sqrt{\epsilon_R}}{\kappa^2} \ . \tag{5.39}$$

We see that as $\epsilon_R \to 0$, a decrease of ϵ_R by an order of magnitude requires κ^2 to decrease by a factor of $\sqrt{10}$ to maintain the correct relic abundance.

What are the smallest possible values of ϵ_R? In the scalar dark matter case, as we lower ϵ_R, eventually the phase-space suppression of hidden sector decays will outweigh the kinetic mixing suppression of standard model decays, so that our assumption of invisible decays fails. Neglecting the electron mass, the requirement that the invisible width dominates implies

$$\Gamma_\phi \approx \frac{\alpha_X m_{A'}}{12} \epsilon_R^{3/2} \gtrsim \frac{\alpha m_{A'}}{3B_e} \kappa^2 \approx \Gamma_{\rm SM} \ . \tag{5.40}$$

It is clear, based on the power law dependence on ϵ_R, that this condition cannot hold simultaneously with the thermal relic constraint over all of parameter space. For a given α_X, there will be a minimum value of ϵ_R below which visible decays dominate the dark photon width. We find this minimum value to be $\epsilon_R^{\rm min} \approx 10^{-6}$ for $\alpha_X = 0.5$.

In contrast, in the pseudo-Dirac case, the invisible width condition is

$$\Gamma_\chi \approx \frac{\alpha_X m_{A'}}{3} \epsilon_R^{1/2} \gtrsim \frac{\alpha m_{A'}}{3B_e} \kappa^2 \approx \Gamma_{\rm SM} \ , \tag{5.41}$$

which follows the same scaling as the thermal relic condition. In the pseudo-Dirac case, then, it is possible to lower the thermal target region to arbitrarily low values of κ^2 by choosing the dark matter to be arbitrarily close to resonance. Put another way, enforcing the thermal relic constraint on a pseudo-Dirac dark sector "accidentally" fixes the ratio between the visible and invisible widths of the dark photon, so that the dual assumptions of mostly invisible

dark photon decays and of thermal relic pseudo-Dirac dark matter may hold concurrently for all values of ϵ_R.

This is a remarkable result. It may be possible, in principle, to construct an experiment that can truly probe all of the thermal relic parameter space for perturbative theories of complex scalar dark matter coupled to a dark photon, but theories of fermionic dark matter may evade any such search by a fine-tuned choice of the dark sector masses.

The interesting behavior for highly degenerate cases may have interesting consequences in other contexts. For example, in the case of Kaluza-Klein dark matter [217, 218], level-1 fermionic dark matter with mass $m_{\rm KK}$ may annihilate through level-2 resonances with masses near $2m_{\rm KK}$, providing a rationale for high degeneracies. These resonances will impact thermal relic density calculations [219], but for extreme degeneracies, our results imply that there may also be interesting astrophysical signals from dark matter annihilation long after freeze out. Other interesting implications of resonances for such TeV-scale dark matter have been explored in Refs. [220, 221, 222].

5.6 Conclusions

The absence of the discovery of WIMPs and other classic dark matter candidates has motivated many new dark matter candidates in recent years. Among those that are often seen as especially motivated are those that are in thermal equilibrium with the standard model at early times, but then freeze out with the correct thermal relic density. The regions of model parameter space that give the desired relic density are "thermal targets" that provide important goals for new experimental searches.

In this study, we considered dark photon scenarios in which the dark photon decays invisibly to dark matter through $A' \to XX$. Such scenarios can be probed by experiments searching

for missing mass, energy, or momentum. For generic A' and X masses, proposed experiments, notably LDMX, are projected to be sensitive to the thermal target parameter space. Direct detection experiments may also be sensitive to these scenarios by searches for $X\,\mathrm{SM} \to X\,\mathrm{SM}$ induced by t-channel A' exchange.

Of course, in such scenarios, since $m_{A'} > 2m_X$, the annihilation process $XX \to A' \to \mathrm{SM}$ can be enhanced by the A' resonance when the initial state dark matter particles have sufficient kinetic energies. In this work, we have found that for $m_{A'} - 2m_X \sim 0.1\, m_X$, the resonance implies a kinematic enhancement of the annihilation rate for scalar (pseudo-Dirac) dark matter of four (two) orders of magnitude, or, alternatively, the thermal target parameter space moves to values of the kinetic mixing κ^2 that are four (two) orders of magnitude smaller. We derived these results using a simple analytic estimate in Sec. 5.3 and through a more accurate numerical analysis in Sec. 5.4.

The resulting thermal targets are shown in Figs. 5.1 and 5.2. Even for the case of a 10% degeneracy $m_{A'} - 2m_X \sim 0.1\, m_X$, we find that the thermal targets are very difficult to probe. For the scalar case, the thermal target is below the projected reach of LDMX and all other proposed accelerator experiments. For the pseudo-Dirac case, the thermal target is also beyond the reach of all proposed accelerator-based experiments, with the exception of LDMX, for which it is at the border of sensitivity, and becomes very challenging for smaller mass splittings. Direct detection experiments do slightly better, as the thermal target for $\epsilon_R \sim 10\%$ is still within the projected reach of some far future experiments in the scalar case, but the thermal targets are still beyond all proposed experiments in the Majorana case.

For even greater degeneracies, with $m_{A'} - 2m_X \ll 0.1\, m_X$, the thermal targets move to even lower values of κ^2. For $\epsilon_R \sim 10^{-6}$, the thermal targets are essentially beyond all proposed accelerator and direct detection experiments for both the scalar and fermionic dark matter cases.

Interestingly, for the case of scalar dark matter, for extreme degeneracies, the condition that the A' decays dominantly invisibly becomes inconsistent with the thermal relic condition. This establishes a floor at $m_{A'} - 2m_X \sim 10^{-6}\, m_X$ that is roughly four orders of magnitude in κ^2 below the projected reach of LDMX, but which is the ultimate goal for an experiment that can probe the entire thermal target region. The floor of the scalar dark matter parameter space may be accessible to future superfluid helium experiments. Unfortunately, for pseudo-Dirac dark matter, there is no such floor for the thermal target. Of course, barring some more fundamental rationale, the fine-tuning required for such degeneracies is extreme, and ultimately other constraints will apply.

Chapter 6

Conclusions

In tackling the dark matter problem we have to do several things. Dark matter presents a unique problem in that it interacts very weakly or not at all with the Standard Model. However, we know that the final theory of nature has to be a quantum field theory and we have some theoretical reasons to expect that there will be a lot of structure in the high energy regime of nature. To simplify that, we shift our focus away from complete models of nature and towards simplified models. This enables us to look at the theory in experiment-driven ways and start by fitting known phenomena with a minimum of encumbering framework.

In this dissertation we have advanced this effort by examining in particular the vector portal and phenomenology of associated dark photons and dark matter. We have studied the process of dark matter capture in astrophysical bodies, and found the rate at which such a captured dark matter population will radiate dark photons, including the nonperturbative Sommerfeld enhancement of the annihilation cross section. We found that experimental searches focused on the decay products of these dark photons will probe the same region of parameter space currently being investigated by direct detection experiments, serving as a complementary probe, and that even small regions outside the scope of direct detection

experiments are amenable to discovery or exclusion by this method. We found further that this search is robust against small mass splittings in the dark sector, while direct detection experiments experience dramatic losses in sensitivity.

In Chapter 5 we examined the thermal relic target of a resonant dark sector, and found that very weak couplings between the dark and visible sectors may still produce the correct abundance of dark matter if compensated by the enhancement of near-resonant annihilation. We found that in the case of a scalar dark sector, there is an absolute lower limit on thermal relic couplings not far out of experimental reach, while a fermionic dark sector may be pushed to arbitrarily low coupling values by pushing the dark photon ever closer to resonance.

Beyond the immediate impact of this work, much of the work in this dissertation may be considered as a case study for more general theories of self interacting dark matter. Similar analyses may for example be carried out for the capture of dark matter through the Higgs portal, or for the annihilation of axion portal dark matter near resonance.

Bibliography

[1] A. Rajaraman and J. Smolinsky, "Self-Interacting Dark Matter Through the Majoron Portal," `arXiv:1811.06619 [hep-ph]`.

[2] J. L. Feng and J. Smolinsky, "Impact of a resonance on thermal targets for invisible dark photon searches," *Phys. Rev.* **D96** no. 9, (2017) 095022, `arXiv:1707.03835 [hep-ph]`.

[3] J. Smolinsky and P. Tanedo, "Dark Photons from Captured Inelastic Dark Matter Annihilation: Charged Particle Signatures," *Phys. Rev.* **D95** no. 7, (2017) 075015, `arXiv:1701.03168 [hep-ph]`. [Erratum: Phys. Rev.D96,no.9,099902(2017)].

[4] J. L. Feng, B. Fornal, I. Galon, S. Gardner, J. Smolinsky, T. M. P. Tait, and P. Tanedo, "Particle physics models for the 17 MeV anomaly in beryllium nuclear decays," *Phys. Rev.* **D95** no. 3, (2017) 035017, `arXiv:1608.03591 [hep-ph]`.

[5] J. L. Feng, B. Fornal, I. Galon, S. Gardner, J. Smolinsky, T. M. P. Tait, and P. Tanedo, "Protophobic Fifth-Force Interpretation of the Observed Anomaly in ^{8}Be Nuclear Transitions," *Phys. Rev. Lett.* **117** no. 7, (2016) 071803, `arXiv:1604.07411 [hep-ph]`.

[6] J. L. Feng, J. Smolinsky, and P. Tanedo, "Detecting dark matter through dark photons from the Sun: Charged particle signatures," *Phys. Rev.* **D93** no. 11, (2016) 115036, `arXiv:1602.01465 [hep-ph]`. [Erratum: Phys. Rev.D96,no.9,099903(2017)].

[7] J. L. Feng, J. Smolinsky, and P. Tanedo, "Dark Photons from the Center of the Earth: Smoking-Gun Signals of Dark Matter," *Phys. Rev.* **D93** no. 1, (2016) 015014, `arXiv:1509.07525 [hep-ph]`. [Erratum: Phys. Rev.D96,no.9,099901(2017)].

[8] A. Rajaraman, J. Smolinsky, and P. Tanedo, "On-Shell Mediators and Top-Charm Dark Matter Models for the Fermi-LAT Galactic Center Excess," `arXiv:1503.05919 [hep-ph]`.

[9] **FASER** Collaboration, A. Ariga *et al.*, "FASER: ForwArd Search ExpeRiment at the LHC," `arXiv:1901.04468 [hep-ex]`.

[10] **FASER** Collaboration, A. Ariga *et al.*, "Technical Proposal for FASER: ForwArd Search ExpeRiment at the LHC," `arXiv:1812.09139 [physics.ins-det]`.

[11] **FASER** Collaboration, A. Ariga *et al.*, "FASER's Physics Reach for Long-Lived Particles," `arXiv:1811.12522 [hep-ph]`.

[12] M. Battaglieri *et al.*, "US Cosmic Visions: New Ideas in Dark Matter 2017: Community Report," `arXiv:1707.04591 [hep-ph]`.

[13] F. Zwicky, "Die Rotverschiebung von extragalaktischen Nebeln," *Helv. Phys. Acta* **6** (1933) 110–127. [Gen. Rel. Grav.41,207(2009)].

[14] V. C. Rubin and W. K. Ford, Jr., "Rotation of the Andromeda Nebula from a Spectroscopic Survey of Emission Regions," *Astrophys. J.* **159** (1970) 379–403.

[15] K. C. Freeman, "On the disks of spiral and SO Galaxies," *Astrophys. J.* **160** (1970) 811.

[16] J. Terning, *Modern supersymmetry: Dynamics and duality.* 2006.

[17] P. Ramond, "Journeys beyond the standard model," *Front. Phys.* **101** (1999) 1–390.

[18] D. Clowe, M. Bradac, A. H. Gonzalez, M. Markevitch, S. W. Randall, C. Jones, and D. Zaritsky, "A direct empirical proof of the existence of dark matter," *Astrophys. J.* **648** (2006) L109–L113, `arXiv:astro-ph/0608407 [astro-ph]`.

[19] **Planck** Collaboration, N. Aghanim *et al.*, "Planck 2018 results. VI. Cosmological parameters," `arXiv:1807.06209 [astro-ph.CO]`.

[20] G. Jungman, M. Kamionkowski, and K. Griest, "Supersymmetric dark matter," *Phys. Rept.* **267** (1996) 195–373, `arXiv:hep-ph/9506380 [hep-ph]`.

[21] P. Gondolo and G. Gelmini, "Cosmic abundances of stable particles: Improved analysis," *Nucl. Phys.* **B360** (1991) 145–179.

[22] D. N. Spergel and P. J. Steinhardt, "Observational evidence for selfinteracting cold dark matter," *Phys. Rev. Lett.* **84** (2000) 3760–3763, `arXiv:astro-ph/9909386 [astro-ph]`.

[23] M. Boylan-Kolchin, J. S. Bullock, and M. Kaplinghat, "Too big to fail? The puzzling darkness of massive Milky Way subhaloes," *Mon. Not. Roy. Astron. Soc.* **415** (2011) L40, `arXiv:1103.0007 [astro-ph.CO]`.

[24] K. A. Oman *et al.*, "The unexpected diversity of dwarf galaxy rotation curves," *Mon. Not. Roy. Astron. Soc.* **452** no. 4, (2015) 3650–3665, `arXiv:1504.01437 [astro-ph.GA]`.

[25] A. Kamada, M. Kaplinghat, A. B. Pace, and H.-B. Yu, "How the Self-Interacting Dark Matter Model Explains the Diverse Galactic Rotation Curves," *Phys. Rev. Lett.* **119** no. 11, (2017) 111102, `arXiv:1611.02716 [astro-ph.GA]`.

[26] B. Patt and F. Wilczek, "Higgs-field portal into hidden sectors," `arXiv:hep-ph/0605188 [hep-ph]`.

[27] M. A. Fedderke, J.-Y. Chen, E. W. Kolb, and L.-T. Wang, "The Fermionic Dark Matter Higgs Portal: an effective field theory approach," *JHEP* **08** (2014) 122, `arXiv:1404.2283 [hep-ph]`.

[28] Y. Nomura and J. Thaler, "Dark Matter through the Axion Portal," *Phys. Rev.* **D79** (2009) 075008, `arXiv:0810.5397 [hep-ph]`.

[29] B. Holdom, "Two U(1)'s and Epsilon Charge Shifts," *Phys. Lett.* **B166** (1986) 196–198.

[30] B. Holdom, "Searching for ϵ Charges and a New U(1)," *Phys. Lett.* **B178** (1986) 65.

[31] S. Tulin, H.-B. Yu, and K. M. Zurek, "Beyond Collisionless Dark Matter: Particle Physics Dynamics for Dark Matter Halo Structure," *Phys. Rev.* **D87** (2013) 115007, `arXiv:1302.3898 [hep-ph]`.

[32] M. Collie and R. Foot, "Neutrino masses in the SU(5) x SU(5)-prime mirror symmetric model," *Phys.Lett.* **B432** (1998) 134–138, `arXiv:hep-ph/9803261 [hep-ph]`.

[33] I. Y. Kobzarev, L. Okun, and I. Y. Pomeranchuk, "On the possibility of experimental observation of mirror particles," *Sov.J.Nucl.Phys.* **3** (1966) 837–841.

[34] L. B. Okun, "Limits of electrodynamics: paraphotons?," *Sov. Phys. JETP* **56** (1982) 502. [Zh. Eksp. Teor. Fiz. 83, 892 (1982)].

[35] R. Essig *et al.*, "Working Group Report: New Light Weakly Coupled Particles," in *Community Summer Study 2013: Snowmass on the Mississippi (CSS2013) Minneapolis, MN, USA, July 29-August 6, 2013*. 2013. `arXiv:1311.0029 [hep-ph]`.

[36] R. Foot, "Mirror dark matter: Cosmology, galaxy structure and direct detection," *Int.J.Mod.Phys.* **A29** (2014) 1430013, `arXiv:1401.3965 [astro-ph.CO]`.

[37] K. Freese, "Can Scalar Neutrinos Or Massive Dirac Neutrinos Be the Missing Mass?," *Phys. Lett.* **B167** (1986) 295.

[38] W. H. Press and D. N. Spergel, "Capture by the Sun of a Galactic Population of Weakly Interacting Massive Particles," *Astrophys.J.* **296** (1985) 679–684.

[39] J. Silk, K. A. Olive, and M. Srednicki, "The Photino, the Sun and High-Energy Neutrinos," *Phys. Rev. Lett.* **55** (1985) 257–259.

[40] L. M. Krauss, M. Srednicki, and F. Wilczek, "Solar System Constraints and Signatures for Dark Matter Candidates," *Phys. Rev.* **D33** (1986) 2079–2083.

[41] K. Griest and D. Seckel, "Cosmic Asymmetry, Neutrinos and the Sun," *Nucl.Phys.* **B283** (1987) 681.

[42] T. K. Gaisser, G. Steigman, and S. Tilav, "Limits on Cold Dark Matter Candidates from Deep Underground Detectors," *Phys. Rev.* **D34** (1986) 2206.

[43] A. Gould, "WIMP Distribution in and Evaporation From the Sun," *Astrophys.J.* **321** (1987) 560.

[44] A. Gould, "Resonant Enhancements in WIMP Capture by the Earth," *Astrophys.J.* **321** (1987) 571.

[45] A. Gould, "Direct and indirect capture of weakly interacting massive particles by the earth," **328** (1988) 919–939.

[46] A. Gould, "Cosmological density of WIMPs from solar and terrestrial annihilations," *Astrophys.J.* **388** (1992) 338–344.

[47] T. Damour and L. M. Krauss, "A New solar system population of WIMP dark matter," *Phys. Rev. Lett.* **81** (1998) 5726–5729, `arXiv:astro-ph/9806165 [astro-ph]`.

[48] T. Damour and L. M. Krauss, "A New WIMP population in the solar system and new signals for dark matter detectors," *Phys. Rev.* **D59** (1999) 063509, `arXiv:astro-ph/9807099 [astro-ph]`.

[49] A. Gould and S. M. Khairul Alam, "Can heavy WIMPs be captured by the earth?," *Astrophys. J.* **549** (2001) 72–75, `arXiv:astro-ph/9911288 [astro-ph]`.

[50] J. Lundberg and J. Edsjo, "WIMP diffusion in the solar system including solar depletion and its effect on earth capture rates," *Phys. Rev.* **D69** (2004) 123505, `arXiv:astro-ph/0401113 [astro-ph]`.

[51] A. H. Peter, "Dark Matter in the Solar System I: the Distribution Function of Wimps at the Earth from Solar Capture," *Phys. Rev.* **D79** (2009) 103531, `arXiv:0902.1344 [astro-ph.HE]`.

[52] A. H. Peter, "Dark Matter in the Solar System II: WIMP Annihilation Rates in the Sun," *Phys. Rev.* **D79** (2009) 103532, `arXiv:0902.1347 [astro-ph.HE]`.

[53] A. H. Peter, "Dark Matter in the Solar System III: the Distribution Function of Wimps at the Earth from Gravitational Capture," *Phys. Rev.* **D79** (2009) 103533, `arXiv:0902.1348 [astro-ph.HE]`.

[54] T. Bruch, A. H. G. Peter, J. Read, L. Baudis, and G. Lake, "Dark Matter Disc Enhanced Neutrino Fluxes from the Sun and Earth," *Phys. Lett.* **B674** (2009) 250–256, `arXiv:0902.4001 [astro-ph.HE]`.

[55] S. M. Koushiappas and M. Kamionkowski, "Galactic Substructure and Energetic Neutrinos from the Sun and the Earth," *Phys. Rev. Lett.* **103** (2009) 121301, `arXiv:0907.4778 [astro-ph.CO]`.

[56] C. Delaunay, P. J. Fox, and G. Perez, "Probing Dark Matter Dynamics via Earthborn Neutrinos at IceCube," *JHEP* **05** (2009) 099, `arXiv:0812.3331 [hep-ph]`.

[57] P. Schuster, N. Toro, and I. Yavin, "Terrestrial and Solar Limits on Long-Lived Particles in a Dark Sector," *Phys. Rev.* **D81** (2010) 016002, `arXiv:0910.1602 [hep-ph]`.

[58] P. Schuster, N. Toro, N. Weiner, and I. Yavin, "High Energy Electron Signals from Dark Matter Annihilation in the Sun," *Phys. Rev.* **D82** (2010) 115012, `arXiv:0910.1839 [hep-ph]`.

[59] P. Meade, S. Nussinov, M. Papucci, and T. Volansky, "Searches for Long Lived Neutral Particles," *JHEP* **06** (2010) 029, `arXiv:0910.4160 [hep-ph]`.

[60] B. Batell, M. Pospelov, A. Ritz, and Y. Shang, "Solar Gamma Rays Powered by Secluded Dark Matter," *Phys. Rev.* **D81** (2010) 075004, `arXiv:0910.1567 [hep-ph]`.

[61] **The Fermi LAT** Collaboration, M. Ajello *et al.*, "Constraints on Dark Matter Models from a Fermi Lat Search for High-Energy Cosmic-Ray Electrons from the Sun," *Phys. Rev.* **D84** (2011) 032007, `arXiv:1107.4272 [astro-ph.HE]`.

[62] I. F. M. Albuquerque, C. Perez de Los Heros, and D. S. Robertson, "Constraints on self interacting dark matter from IceCube results," *JCAP* **1402** (2014) 047, `arXiv:1312.0797 [astro-ph.CO]`.

[63] J. Chen, Z.-L. Liang, Y.-L. Wu, and Y.-F. Zhou, "Long-Range Self-Interacting Dark Matter in the Sun," `arXiv:1505.04031 [hep-ph]`.

[64] J. Berger, Y. Cui, and Y. Zhao, "Detecting Boosted Dark Matter from the Sun with Large Volume Neutrino Detectors," *JCAP* **1502** (2015) 005, `arXiv:1410.2246 [hep-ph]`.

[65] M. Vogelsberger, J. Zavala, and A. Loeb, "Subhaloes in Self-Interacting Galactic Dark Matter Haloes," *Mon. Not. R. Astron. Soc.* **423** (2012) 3740, `arXiv:1201.5892 [astro-ph.CO]`.

[66] M. Rocha, A. H. G. Peter, J. S. Bullock, M. Kaplinghat, S. Garrison-Kimmel, J. Onorbe, and L. A. Moustakas, "Cosmological Simulations with Self-Interacting Dark Matter I: Constant Density Cores and Substructure," *Mon. Not. R. Astron. Soc.* **430** (2013) 81–104, `arXiv:1208.3025 [astro-ph.CO]`.

[67] A. H. G. Peter, M. Rocha, J. S. Bullock, and M. Kaplinghat, "Cosmological Simulations with Self-Interacting Dark Matter Ii: Halo Shapes Vs. Observations," *Mon. Not. R. Astron. Soc.* **430** (2013) 105, `arXiv:1208.3026 [astro-ph.CO]`.

[68] J. Zavala, M. Vogelsberger, and M. G. Walker, "Constraining Self-Interacting Dark Matter with the Milky Way's Dwarf Spheroidals," *Mon. Not. R. Astro. Soc.* **431** (2013) L20–L24, `arXiv:1211.6426 [astro-ph.CO]`.

[69] M. Kaplinghat, T. Linden, and H.-B. Yu, "Galactic Center Excess in γ Rays from Annihilation of Self-Interacting Dark Matter," *Phys. Rev. Lett.* **114** (2015) 211303, `arXiv:1501.03507 [hep-ph]`.

[70] J. A. Adams, S. Sarkar, and D. W. Sciama, "CMB anisotropy in the decaying neutrino cosmology," *Mon. Not. Roy. Astron. Soc.* **301** (1998) 210–214, `arXiv:astro-ph/9805108 [astro-ph]`.

[71] X.-L. Chen and M. Kamionkowski, "Particle decays during the cosmic dark ages," *Phys. Rev.* **D70** (2004) 043502, `arXiv:astro-ph/0310473 [astro-ph]`.

[72] N. Padmanabhan and D. P. Finkbeiner, "Detecting dark matter annihilation with CMB polarization: Signatures and experimental prospects," *Phys. Rev.* **D72** (2005) 023508, `arXiv:astro-ph/0503486 [astro-ph]`.

[73] T. R. Slatyer, "Indirect dark matter signatures in the cosmic dark ages. I. Generalizing the bound on s-wave dark matter annihilation from Planck results," *Phys. Rev.* **D93** no. 2, (2016) 023527, `arXiv:1506.03811 [hep-ph]`.

[74] M. Buschmann, J. Kopp, J. Liu, and P. A. N. Machado, "Lepton Jets from Radiating Dark Matter," *JHEP* **07** (2015) 045, `arXiv:1505.07459 [hep-ph]`.

[75] A. R. Zentner, "High-Energy Neutrinos From Dark Matter Particle Self-Capture Within the Sun," *Phys. Rev.* **D80** (2009) 063501, `arXiv:0907.3448 [astro-ph.HE]`.

[76] P. Baratella, M. Cirelli, A. Hektor, J. Pata, M. Piibeleht, *et al.*, "PPPC 4 DM ν: a Poor Particle Physicist Cookbook for Neutrinos from Dark Matter Annihilations in the Sun," *JCAP* **1403** (2014) 053, `arXiv:1312.6408 [hep-ph]`.

[77] N. Fornengo, P. Panci, and M. Regis, "Long-Range Forces in Direct Dark Matter Searches," *Phys. Rev.* **D84** (2011) 115002, `arXiv:1108.4661 [hep-ph]`.

[78] J. Lewin and P. Smith, "Review of Mathematics, Numerical Factors, and Corrections for Dark Matter Experiments Based on Elastic Nuclear Recoil," *Astropart.Phys.* **6** (1996) 87–112.

[79] A. M. Dziewonski and D. L. Anderson, "Preliminary reference Earth model," *Physics of The Earth and Planetary Interiors* **25** (1981) 297–356.

[80] H. D. Holland and K. K. Turekian, *Treatise on Geochemistry.* Pergamon [Imprint], 2003.

[81] A. Gould, "Gravitational diffusion of solar system WIMPs," *ApJ* **368** (1991) 610–615.

[82] J. I. Read, L. Mayer, A. M. Brooks, F. Governato, and G. Lake, "A dark matter disc in three cosmological simulations of Milky Way mass galaxies," *Mon. Not. R. Astro. Soc.* **397** (2009) 44–51, `arXiv:0902.0009`.

[83] J. I. Read, G. Lake, O. Agertz, and V. P. Debattista, "Thin, thick and dark discs in ΛCDM," *Mon. Not. R. Astro. Soc.* **389** (2008) 1041–1057, `arXiv:0803.2714`.

[84] C. W. Purcell, J. S. Bullock, and M. Kaplinghat, "The Dark Disk of the Milky Way," *Astrophys. J.* **703** (2009) 2275–2284, arXiv:0906.5348 [astro-ph.GA].

[85] A. Peter, "Dark Matter Bound to the Solar System: Consequences for Annihilation Searches," in *Proceedings, 44Th Rencontres De Moriond on Electroweak Interactions and Unified Theories*, pp. 359–366. 2009. arXiv:0905.2456 [astro-ph.HE].

[86] J. D. Vergados, "Modulation effect in the differential rate for supersymmetric dark matter detection," *Phys. Rev.* **D58** (1998) 103001, arXiv:hep-ph/9802253 [hep-ph].

[87] M. Vogelsberger, A. Helmi, V. Springel, S. D. White, J. Wang, *et al.*, "Phase-Space Structure in the Local Dark Matter Distribution and Its Signature in Direct Detection Experiments," *Mon. Not. R. Astron. Soc.* **395** (2009) 797–811, arXiv:0812.0362 [astro-ph].

[88] M. Fairbairn and T. Schwetz, "Spin-Independent Elastic WIMP Scattering and the Dama Annual Modulation Signal," *JCAP* **0901** (2009) 037, arXiv:0808.0704 [hep-ph].

[89] M. Kuhlen, N. Weiner, J. Diemand, P. Madau, B. Moore, *et al.*, "Dark Matter Direct Detection with Non-Maxwellian Velocity Structure," *JCAP* **1002** (2010) 030, arXiv:0912.2358 [astro-ph.GA].

[90] F. Ling, E. Nezri, E. Athanassoula, and R. Teyssier, "Dark Matter Direct Detection Signals Inferred from a Cosmological N-Body Simulation with Baryons," *JCAP* **1002** (2010) 012, arXiv:0909.2028 [astro-ph.GA].

[91] M. Lisanti, L. E. Strigari, J. G. Wacker, and R. H. Wechsler, "The Dark Matter at the End of the Galaxy," *Phys. Rev.* **D83** (2011) 023519, arXiv:1010.4300 [astro-ph.CO].

[92] Y.-Y. Mao, L. E. Strigari, R. H. Wechsler, H.-Y. Wu, and O. Hahn, "Halo-To-Halo Similarity and Scatter in the Velocity Distribution of Dark Matter," *Astrophys.J.* **764** (2013) 35, arXiv:1210.2721 [astro-ph.CO].

[93] K. Choi, C. Rott, and Y. Itow, "Impact of the dark matter velocity distribution on capture rates in the Sun," *JCAP* **1405** (2014) 049, arXiv:1312.0273 [astro-ph.HE].

[94] M. Abramowitz and I. Stegun, *Handbook of Mathematical Functions: With Formulas, Graphs, and Mathematical Tables.* Applied mathematics series. Dover Publications, 1964. See Section 5.1.

[95] J. Liu, N. Weiner, and W. Xue, "Signals of a Light Dark Force in the Galactic Center," *JHEP* **08** (2015) 050, arXiv:1412.1485 [hep-ph].

[96] A. Sommerfeld, "Über die Beugung und Bremsung der Elektronen," *Ann. der Physik* **403** (1931) 257.

[97] S. Cassel, "Sommerfeld factor for arbitrary partial wave processes," *J.Phys.* **G37** (2010) 105009, arXiv:0903.5307 [hep-ph].

[98] T. R. Slatyer, "The Sommerfeld enhancement for dark matter with an excited state," *JCAP* **1002** (2010) 028, arXiv:0910.5713 [hep-ph].

[99] J. L. Feng, M. Kaplinghat, and H.-B. Yu, "Sommerfeld Enhancements for Thermal Relic Dark Matter," *Phys. Rev.* **D82** (2010) 083525, arXiv:1005.4678 [hep-ph].

[100] **IceCube** Collaboration, R. Abbasi *et al.*, "The Design and Performance of IceCube DeepCore," *Astropart. Phys.* **35** (2012) 615–624, arXiv:1109.6096 [astro-ph.IM].

[101] E. Del Nobile, M. Kaplinghat, and H.-B. Yu, "Direct Detection Signatures of Self-Interacting Dark Matter with a Light Mediator," arXiv:1507.04007 [hep-ph].

[102] J. B. Dent, F. Ferrer, and L. M. Krauss, "Constraints on Light Hidden Sector Gauge Bosons from Supernova Cooling," arXiv:1201.2683 [astro-ph.CO].

[103] H. K. Dreiner, J.-F. Fortin, C. Hanhart, and L. Ubaldi, "Supernova constraints on MeV dark sectors from e^+e^- annihilations," *Phys. Rev.* **D89** (2014) 105015, arXiv:1310.3826 [hep-ph].

[104] D. Kazanas, R. N. Mohapatra, S. Nussinov, V. L. Teplitz, and Y. Zhang, "Supernova Bounds on the Dark Photon Using its Electromagnetic Decay," *Nucl.Phys.* **B890** (2014) 17–29, arXiv:1410.0221 [hep-ph].

[105] E. Rrapaj and S. Reddy, "Nucleon-Nucleon Bremsstrahlung of Dark Gauge Bosons and Revised Supernova Constraints," arXiv:1511.09136 [nucl-th].

[106] **PandaX-II** Collaboration, X. Cui *et al.*, "Dark Matter Results From 54-Ton-Day Exposure of PandaX-II Experiment," arXiv:1708.06917 [astro-ph.CO].

[107] C. Mahoney, A. K. Leibovich, and A. R. Zentner, "Updated Constraints on Self-Interacting Dark Matter from Supernova 1987A," *Phys. Rev.* **D96** no. 4, (2017) 043018, arXiv:1706.08871 [hep-ph].

[108] **LUX** Collaboration, D. S. Akerib *et al.*, "First Results from the Lux Dark Matter Experiment at the Sanford Underground Research Facility," *Phys. Rev. Lett.* **112** (2014) 091303, arXiv:1310.8214 [astro-ph.CO].

[109] M. Kaplinghat, S. Tulin, and H.-B. Yu, "Direct Detection Portals for Self-interacting Dark Matter," *Phys. Rev.* **D89** (2014) 035009, arXiv:1310.7945 [hep-ph].

[110] H. An, M. Pospelov, J. Pradler, and A. Ritz, "Direct Detection Constraints on Dark Photon Dark Matter," *Phys. Lett.* **B747** (2015) 331–338, arXiv:1412.8378 [hep-ph].

[111] J. Billard, L. Strigari, and E. Figueroa-Feliciano, "Implication of Neutrino Backgrounds on the Reach of Next Generation Dark Matter Direct Detection Experiments," *Phys. Rev.* **D89** no. 2, (2014) 023524, arXiv:1307.5458 [hep-ph].

[112] **Particle Data Group** Collaboration, K. A. Olive *et al.*, "Review of Particle Physics," *Chin. Phys.* **C38** (2014) 090001.

[113] I. Albuquerque, G. Burdman, and Z. Chacko, "Neutrino telescopes as a direct probe of supersymmetry breaking," *Phys. Rev. Lett.* **92** (2004) 221802, `arXiv:hep-ph/0312197 [hep-ph]`.

[114] I. F. M. Albuquerque, G. Burdman, and Z. Chacko, "Direct detection of supersymmetric particles in neutrino telescopes," *Phys. Rev.* **D75** (2007) 035006, `arXiv:hep-ph/0605120 [hep-ph]`.

[115] S. Kopper, "Search for Neutrino-Induced Double Tracks as an Exotic Physics Signature in IceCube," *Proceedings of 'The 34th International Cosmic Ray Conference'* (2015) . PoS (ICRC2015) 1104.

[116] F. Halzen and S. R. Klein, "Icecube: an Instrument for Neutrino Astronomy," *Rev.Sci.Instrum.* **81** (2010) 081101, `arXiv:1007.1247 [astro-ph.HE]`.

[117] **IceCube PINGU** Collaboration, M. G. Aartsen *et al.*, "Letter of Intent: The Precision IceCube Next Generation Upgrade (PINGU)," `arXiv:1401.2046 [physics.ins-det]`.

[118] **AMS 02 ECAL Group** Collaboration, G. Gallucci, "Performance of the AMS-02 Electromagnetic Calorimeter in Space," *J.Phys.Conf.Ser.* **587** (2015) 012028.

[119] G. Steigman, B. Dasgupta, and J. F. Beacom, "Precise Relic WIMP Abundance and Its Impact on Searches for Dark Matter Annihilation," *Phys.Rev.* **D86** (2012) 023506, `arXiv:1204.3622 [hep-ph]`.

[120] J. D. Bjorken, S. Ecklund, W. R. Nelson, A. Abashian, C. Church, B. Lu, L. W. Mo, T. A. Nunamaker, and P. Rassmann, "Search for Neutral Metastable Penetrating Particles Produced in the SLAC Beam Dump," *Phys. Rev.* **D38** (1988) 3375.

[121] J. D. Bjorken, R. Essig, P. Schuster, and N. Toro, "New Fixed-Target Experiments to Search for Dark Gauge Forces," *Phys. Rev.* **D80** (2009) 075018, `arXiv:0906.0580 [hep-ph]`.

[122] B. Batell, M. Pospelov, and A. Ritz, "Exploring Portals to a Hidden Sector Through Fixed Targets," *Phys. Rev.* **D80** (2009) 095024, `arXiv:0906.5614 [hep-ph]`.

[123] R. Essig, R. Harnik, J. Kaplan, and N. Toro, "Discovering New Light States at Neutrino Experiments," *Phys. Rev.* **D82** (2010) 113008, `arXiv:1008.0636 [hep-ph]`.

[124] **LSND** Collaboration, C. Athanassopoulos, L. B. Auerbach, R. L. Burman, D. O. Caldwell, E. D. Church, I. Cohen, J. B. Donahue, A. Fazely, F. J. Federspiel, G. T. Garvey, R. M. Gunasingha, R. Imlay, K. Johnston, H. J. Kim, W. C. Louis, R. Majkic, K. McIlhany, W. Metcalf, G. B. Mills, R. A. Reeder, V. Sandberg, D. Smith, I. Stancu, W. Strossman, R. Tayloe, G. J. VanDalen, W. Vernon,

N. Wadia, J. Waltz, D. H. White, D. Works, Y. Xiao, and S. Yellin, "Results on $\nu_\mu \to \nu_e$ oscillations from pion decay in flight neutrinos," *Phys. Rev. C* **58** (1998) 2489–2511. http://link.aps.org/doi/10.1103/PhysRevC.58.2489.

[125] S. Gninenko, "Constraints on sub-gev hidden sector gauge bosons from a search for heavy neutrino decays," *Physics Letters B* **713** no. 3, (2012) 244 – 248. http://www.sciencedirect.com/science/article/pii/S0370269312006284.

[126] **CHARM** Collaboration, F. Bergsma *et al.*, "A search for decays of heavy neutrinos in the mass range 0.5 gev to 2.8 gev," *Phys. Lett.* **B166** (1986) 473.

[127] Y. Zhang, "Supernova Cooling in a Dark Matter Smog," *JCAP* **1411** no. 11, (2014) 042, arXiv:1404.7172 [hep-ph].

[128] A. Fradette, M. Pospelov, J. Pradler, and A. Ritz, "Cosmological Constraints on Very Dark Photons," *Phys. Rev.* **D90** (2014) 035022, arXiv:1407.0993 [hep-ph].

[129] A. Serenelli, S. Basu, J. W. Ferguson, and M. Asplund, "New Solar Composition: the Problem with Solar Models Revisited," *Astrophys. J.* **705** (2009) L123–L127, arXiv:0909.2668 [astro-ph.SR].

[130] A. M. Serenelli, "New Results on Standard Solar Models," *Astrophys. Space Sci.* **328** (2010) 13–21, arXiv:0910.3690 [astro-ph.SR].

[131] A. Serenelli, "Standard solar model and solar neutrinos." http://wwwmpa.mpa-garching.mpg.de/∼aldos/solar_main.html.

[132] S. A. Khrapak, A. V. Ivlev, G. E. Morfill, and S. K. Zhdanov, "Scattering in the attractive yukawa potential in the limit of strong interaction," *Phys. Rev. Lett.* **90** (Jun, 2003) 225002. http://link.aps.org/doi/10.1103/PhysRevLett.90.225002.

[133] S. Khrapak, "Classical Scattering in Strongly Attractive Potentials," *Phys. Rev.* **E89** no. 3, (2014) 032145, arXiv:1403.6000 [physics.chem-ph].

[134] J. L. Feng, M. Kaplinghat, and H.-B. Yu, "Halo Shape and Relic Density Exclusions of Sommerfeld-Enhanced Dark Matter Explanations of Cosmic Ray Excesses," *Phys. Rev. Lett.* **104** (2010) 151301, arXiv:0911.0422 [hep-ph].

[135] **AMS** Collaboration, M. Aguilar *et al.*, "Electron and Positron Fluxes in Primary Cosmic Rays Measured with the Alpha Magnetic Spectrometer on the International Space Station," *Phys. Rev. Lett.* **113** (2014) 121102.

[136] F. Machate, H. Gast, and S. Schael for the AMS Collaboation. Private communication.

[137] E. N. Parker, "Dynamics of the Interplanetary Gas and Magnetic Fields.," **128** (1958) 664.

[138] M. S. Potgieter, "Solar modulation of cosmic rays," *Living Reviews in Solar Physics* **10** no. 3, (2013) . http://www.livingreviews.org/lrsp-2013-3.

[139] A. Balogh, L. Lanzerotti, and S. Suess, *The Heliosphere through the Solar Activity Cycle*. Springer Praxis Books. Springer Berlin Heidelberg, 2007.

[140] J. P. Roberts, "PAMELA Through a Magnetic Lense," *JCAP* **1102** (2011) 029, `arXiv:1005.4668 [astro-ph.HE]`.

[141] E. Izaguirre, G. Krnjaic, and B. Shuve, "Discovering Inelastic Thermal-Relic Dark Matter at Colliders," *Phys. Rev.* **D93** (2016) 063523, `arXiv:1508.03050 [hep-ph]`.

[142] D. Tucker-Smith and N. Weiner, "Inelastic dark matter," *Phys. Rev.* **D64** (2001) 043502, `arXiv:hep-ph/0101138 [hep-ph]`.

[143] S. Chang, G. D. Kribs, D. Tucker-Smith, and N. Weiner, "Inelastic Dark Matter in Light of DAMA/LIBRA," *Phys. Rev.* **D79** (2009) 043513, `arXiv:0807.2250 [hep-ph]`.

[144] M. Blennow, S. Clementz, and J. Herrero-Garcia, "Self-interacting inelastic dark matter: A viable solution to the small scale structure problems," `arXiv:1612.06681 [hep-ph]`.

[145] **ANTARES** Collaboration, S. Adrián-Martínez *et al.*, "A search for Secluded Dark Matter in the Sun with the ANTARES neutrino telescope," *JCAP* **1605** no. 05, (2016) 016, `arXiv:1602.07000 [hep-ex]`.

[146] C. Kouvaris, K. Langaeble, and N. G. Nielsen, "The Spectrum of Darkonium in the Sun," `arXiv:1607.00374 [hep-ph]`.

[147] N. Arkani-Hamed, D. P. Finkbeiner, T. R. Slatyer, and N. Weiner, "A Theory of Dark Matter," *Phys. Rev.* **D79** (2009) 015014, `arXiv:0810.0713 [hep-ph]`.

[148] Y. Bai and T. M. P. Tait, "Inelastic Dark Matter at the LHC," *Phys. Lett.* **B710** (2012) 335–338, `arXiv:1109.4144 [hep-ph]`.

[149] A. Menon, R. Morris, A. Pierce, and N. Weiner, "Capture and Indirect Detection of Inelastic Dark Matter," *Phys. Rev.* **D82** (2010) 015011, `arXiv:0905.1847 [hep-ph]`.

[150] R. Harnik and G. D. Kribs, "An Effective Theory of Dirac Dark Matter," *Phys. Rev.* **D79** (2009) 095007, `arXiv:0810.5557 [hep-ph]`.

[151] D. Feldman, Z. Liu, and P. Nath, "The Stueckelberg Z-Prime Extension with Kinetic Mixing and Milli-Charged Dark Matter from the Hidden Sector," *Phys.Rev.* **D75** (2007) 115001, `arXiv:hep-ph/0702123 [HEP-PH]`.

[152] E. Izaguirre and I. Yavin, "New Window to Millicharged Particles at the LHC," *Phys. Rev.* **D92** no. 3, (2015) 035014, `arXiv:1506.04760 [hep-ph]`.

[153] K. Griest and D. Seckel, "Three exceptions in the calculation of relic abundances," *Phys. Rev.* **D43** (1991) 3191–3203.

[154] D. Tucker-Smith and N. Weiner, "The Status of inelastic dark matter," *Phys. Rev.* **D72** (2005) 063509, `arXiv:hep-ph/0402065 [hep-ph]`.

[155] M. Blennow, S. Clementz, and J. Herrero-Garcia, "Pinning down inelastic dark matter in the Sun and in direct detection," *JCAP* **1604** no. 04, (2016) 004, `arXiv:1512.03317 [hep-ph]`.

[156] K. Freese, J. A. Frieman, and A. Gould, "Signal Modulation in Cold Dark Matter Detection," *Phys. Rev.* **D37** (1988) 3388–3405.

[157] J. H. Chang, R. Essig, and S. D. McDermott, "Revisiting Supernova 1987A Constraints on Dark Photons," `arXiv:1611.03864 [hep-ph]`.

[158] E. Hardy and R. Lasenby, "Stellar cooling bounds on new light particles: including plasma effects," `arXiv:1611.05852 [hep-ph]`.

[159] S. Nussinov, L.-T. Wang, and I. Yavin, "Capture of Inelastic Dark Matter in the Sun," *JCAP* **0908** (2009) 037, `arXiv:0905.1333 [hep-ph]`.

[160] **Planck** Collaboration, P. A. R. Ade *et al.*, "Planck 2015 results. XIII. Cosmological parameters," *Astron. Astrophys.* **594** (2016) A13, `arXiv:1502.01589 [astro-ph.CO]`.

[161] J. L. Feng and J. Kumar, "The WIMPless Miracle: Dark-Matter Particles without Weak-Scale Masses or Weak Interactions," *Phys. Rev. Lett.* **101** (2008) 231301, `arXiv:0803.4196 [hep-ph]`.

[162] C. Boehm and P. Fayet, "Scalar dark matter candidates," *Nucl. Phys.* **B683** (2004) 219–263, `arXiv:hep-ph/0305261 [hep-ph]`.

[163] M. Pospelov, "Secluded U(1) below the weak scale," *Phys. Rev.* **D80** (2009) 095002, `arXiv:0811.1030 [hep-ph]`.

[164] **BaBar** Collaboration, J. P. Lees *et al.*, "Search for a Dark Photon in e^+e^- Collisions at BaBar," *Phys. Rev. Lett.* **113** (2014) 201801, `arXiv:1406.2980 [hep-ex]`.

[165] **BaBar** Collaboration, J. P. Lees *et al.*, "Search for invisible decays of a dark photon produced in e+e- collisions at BaBar," `arXiv:1702.03327 [hep-ex]`.

[166] **CRESST** Collaboration, G. Angloher *et al.*, "Results on light dark matter particles with a low-threshold CRESST-II detector," *Eur. Phys. J.* **C76** (2016) 25, `arXiv:1509.01515 [astro-ph.CO]`.

[167] B. Batell, R. Essig, and Z. Surujon, "Strong Constraints on Sub-GeV Dark Sectors from SLAC Beam Dump E137," *Phys. Rev. Lett.* **113** (2014) 171802, `arXiv:1406.2698 [hep-ph]`.

[168] E. Izaguirre, Y. Kahn, G. Krnjaic, and M. Moschella, "Testing Light Dark Matter Coannihilation With Fixed-Target Experiments," `arXiv:1703.06881 [hep-ph]`.

[169] **LSND** Collaboration, C. Athanassopoulos *et al.*, "The Liquid scintillator neutrino detector and LAMPF neutrino source," *Nucl. Instrum. Meth.* **A388** (1997) 149–172, `arXiv:nucl-ex/9605002 [nucl-ex]`.

[170] P. deNiverville, M. Pospelov, and A. Ritz, "Observing a light dark matter beam with neutrino experiments," *Phys. Rev.* **D84** (2011) 075020, `arXiv:1107.4580 [hep-ph]`.

[171] P. deNiverville, C.-Y. Chen, M. Pospelov, and A. Ritz, "Light dark matter in neutrino beams: production modelling and scattering signatures at MiniBooNE, T2K and SHiP," *Phys. Rev.* **D95** no. 3, (2017) 035006, `arXiv:1609.01770 [hep-ph]`.

[172] **NA64** Collaboration, D. Banerjee *et al.*, "Search for invisible decays of sub-GeV dark photons in missing-energy events at the CERN SPS," *Phys. Rev. Lett.* **118** (2017) 011802, `arXiv:1610.02988 [hep-ex]`.

[173] **BDX** Collaboration, M. Battaglieri *et al.*, "Dark Matter Search in a Beam-Dump eXperiment (BDX) at Jefferson Lab," `arXiv:1607.01390 [hep-ex]`.

[174] **BDX** Collaboration, M. Bondí, "Light Dark Matter search in a beam-dump experiment: BDX at Jefferson Lab," *EPJ Web Conf.* **142** (2017) 01005.

[175] C. Hearty, "Dark sector searches at b-factories and outlook for belle ii," 2017. `https://indico.fnal.gov/getFile.py/access?contribId=123&sessionId=9&resId=0&materialId=slides&confId=13702`.

[176] "COHERENT experiment." `http://sites.duke.edu/coherent`.

[177] P. deNiverville, M. Pospelov, and A. Ritz, "Light new physics in coherent neutrino-nucleus scattering experiments," *Phys. Rev.* **D92** (2015) 095005, `arXiv:1505.07805 [hep-ph]`.

[178] J. Balewski *et al.*, "The DarkLight Experiment: A Precision Search for New Physics at Low Energies," 2014. `arXiv:1412.4717 [physics.ins-det]`.

[179] "LDMX experiment." `https://confluence.slac.stanford.edu/display/MME/Light+Dark+Matter+Experiment`.

[180] **MiniBooNE** Collaboration, A. A. Aguilar-Arevalo *et al.*, "Dark Matter Search in a Proton Beam Dump with MiniBooNE," *Phys. Rev. Lett.* **118** (2017) 221803, `arXiv:1702.02688 [hep-ex]`.

[181] J. Alexander, "Dark Photon Search in e+e- Annihilation," 2016. `https://indico.cern.ch/event/507783/contributions/2150181/attachments/1266367/1874844/SLAC-MMAPS-alexander.pdf`.

[182] S. N. Gninenko, "NA64++," 2017. `https://indico.cern.ch/event/608491/contributions/2457799/attachments/1420197/2176021/NA64_0317.pdf`.

[183] M. Raggi and V. Kozhuharov, "Proposal to Search for a Dark Photon in Positron on Target Collisions at DAΦNE Linac," *Adv. High Energy Phys.* **2014** (2014) 959802, arXiv:1403.3041 [physics.ins-det].

[184] M. Raggi, V. Kozhuharov, and P. Valente, "The PADME experiment at LNF," *EPJ Web Conf.* **96** (2015) 01025, arXiv:1501.01867 [hep-ex].

[185] S. Alekhin *et al.*, "A facility to Search for Hidden Particles at the CERN SPS: the SHiP physics case," *Rept. Prog. Phys.* **79** (2016) 124201, arXiv:1504.04855 [hep-ph].

[186] **SHiP** Collaboration, M. Anelli *et al.*, "A facility to Search for Hidden Particles (SHiP) at the CERN SPS," arXiv:1504.04956 [physics.ins-det].

[187] **LAr1-ND, ICARUS-WA104, MicroBooNE** Collaboration, M. Antonello *et al.*, "A Proposal for a Three Detector Short-Baseline Neutrino Oscillation Program in the Fermilab Booster Neutrino Beam," arXiv:1503.01520 [physics.ins-det].

[188] R. Van de Water, "Future Sub-GeV Dark Matter Searches with Proton Fixed Targets at FNAL." https://indico.fnal.gov/getFile.py/access?contribId=157&sessionId=6&resId=10&materialId=minutes&confId=13702.

[189] B. Wojtsekhowski, D. Nikolenko, and I. Rachek, "Searching for a new force at VEPP-3," arXiv:1207.5089 [hep-ex].

[190] E. Izaguirre, G. Krnjaic, P. Schuster, and N. Toro, "Analyzing the Discovery Potential for Light Dark Matter," *Phys. Rev. Lett.* **115** (2015) 251301, arXiv:1505.00011 [hep-ph].

[191] E. Jones, T. Oliphant, P. Peterson, *et al.*, "SciPy: Open source scientific tools for Python," 2001–. http://www.scipy.org. [Online; accessed 6/10/2017].

[192] M. R. Zaghloul and A. N. Ali, "Algorithm 916: Computing the faddeyeva and voigt functions," *ACM Trans. Math. Softw.* **38** (Jan., 2012) 15:1–15:22.

[193] R. Essig, J. Mardon, and T. Volansky, "Direct Detection of Sub-GeV Dark Matter," *Phys. Rev.* **D85** (2012) 076007, arXiv:1108.5383 [hep-ph].

[194] R. Essig, M. Fernandez-Serra, J. Mardon, A. Soto, T. Volansky, and T.-T. Yu, "Direct Detection of sub-GeV Dark Matter with Semiconductor Targets," *JHEP* **05** (2016) 046, arXiv:1509.01598 [hep-ph].

[195] R. Essig, A. Manalaysay, J. Mardon, P. Sorensen, and T. Volansky, "First Direct Detection Limits on sub-GeV Dark Matter from XENON10," *Phys. Rev. Lett.* **109** (2012) 021301, arXiv:1206.2644 [astro-ph.CO].

[196] R. Essig, T. Volansky, and T.-T. Yu, "New Constraints and Prospects for sub-GeV Dark Matter Scattering off Electrons in Xenon," arXiv:1703.00910 [hep-ph].

[197] S. Derenzo, R. Essig, A. Massari, A. Soto, and T.-T. Yu, "Direct Detection of sub-GeV Dark Matter with Scintillating Targets," *Phys. Rev.* **D96** (2017) 016026, arXiv:1607.01009 [hep-ph].

[198] Y. Hochberg, Y. Kahn, M. Lisanti, C. G. Tully, and K. M. Zurek, "Directional detection of dark matter with two-dimensional targets," *Phys. Lett.* **B772** (2017) 239–246, arXiv:1606.08849 [hep-ph].

[199] Y. Hochberg, M. Pyle, Y. Zhao, and K. M. Zurek, "Detecting Superlight Dark Matter with Fermi-Degenerate Materials," *JHEP* **08** (2016) 057, arXiv:1512.04533 [hep-ph].

[200] Y. Hochberg, Y. Zhao, and K. M. Zurek, "Superconducting Detectors for Superlight Dark Matter," *Phys. Rev. Lett.* **116** (2016) 011301, arXiv:1504.07237 [hep-ph].

[201] **DAMIC** Collaboration, A. Aguilar-Arevalo *et al.*, "Search for low-mass WIMPs in a 0.6 kg day exposure of the DAMIC experiment at SNOLAB," *Phys. Rev.* **D94** (2016) 082006, arXiv:1607.07410 [astro-ph.CO].

[202] **DAMIC** Collaboration, A. Aguilar-Arevalo *et al.*, "First Direct-Detection Constraints on eV-Scale Hidden-Photon Dark Matter with DAMIC at SNOLAB," *Phys. Rev. Lett.* **118** (2017) 141803, arXiv:1611.03066 [astro-ph.CO].

[203] J. Tiffenberg, M. Sofo-Haro, A. Drlica-Wagner, R. Essig, Y. Guardincerri, S. Holland, T. Volansky, and T.-T. Yu, "Single-electron and single-photon sensitivity with a silicon Skipper CCD," arXiv:1706.00028 [physics.ins-det].

[204] **SuperCDMS** Collaboration, R. Agnese *et al.*, "Search for Low-Mass Weakly Interacting Massive Particles with SuperCDMS," *Phys. Rev. Lett.* **112** (2014) 241302, arXiv:1402.7137 [hep-ex].

[205] **SuperCDMS** Collaboration, R. Agnese *et al.*, "New Results from the Search for Low-Mass Weakly Interacting Massive Particles with the CDMS Low Ionization Threshold Experiment," *Phys. Rev. Lett.* **116** (2016) 071301, arXiv:1509.02448 [astro-ph.CO].

[206] K. Schutz and K. M. Zurek, "Detectability of Light Dark Matter with Superfluid Helium," *Phys. Rev. Lett.* **117** (2016) 121302, arXiv:1604.08206 [hep-ph].

[207] S. Knapen, T. Lin, and K. M. Zurek, "Light Dark Matter in Superfluid Helium: Detection with Multi-excitation Production," *Phys. Rev.* **D95** (2017) 056019, arXiv:1611.06228 [hep-ph].

[208] W. Guo and D. N. McKinsey, "Concept for a dark matter detector using liquid helium-4," *Phys. Rev.* **D87** (2013) 115001, arXiv:1302.0534 [astro-ph.IM].

[209] F. W. Carter, S. A. Hertel, M. J. Rooks, D. N. McKinsey, and D. E. Prober, "Toward the in situ detection of individual he2 excimers using a ti tes in superfluid helium," *IEEE Transactions an Applied Superconductivity* **25** (2015) 2100707.

[210] H. J. Maris, G. M. Seidel, and D. Stein, "Dark Matter Detection Using Helium Evaporation and Field Ionization," arXiv:1706.00117 [astro-ph.IM].

[211] R. Essig, J. Mardon, O. Slone, and T. Volansky, "Detection of sub-GeV Dark Matter and Solar Neutrinos via Chemical-Bond Breaking," *Phys. Rev.* **D95** (2017) 056011, arXiv:1608.02940 [hep-ph].

[212] R. Budnik, O. Chesnovsky, O. Slone, and T. Volansky, "Direct Detection of Light Dark Matter and Solar Neutrinos via Color Center Production in Crystals," arXiv:1705.03016 [hep-ph].

[213] P. C. Bunting, G. Gratta, T. Melia, and S. Rajendran, "Magnetic Bubble Chambers and Sub-GeV Dark Matter Direct Detection," *Phys. Rev.* **D95** (2017) 095001, arXiv:1701.06566 [hep-ph].

[214] D. Baxter *et al.*, "First Demonstration of a Scintillating Xenon Bubble Chamber for Detecting Dark Matter and Coherent Elastic Neutrino-Nucleus Scattering," *Phys. Rev. Lett.* **118** (2017) 231301, arXiv:1702.08861 [physics.ins-det].

[215] C. Kouvaris and J. Pradler, "Probing sub-GeV Dark Matter with conventional detectors," *Phys. Rev. Lett.* **118** (2017) 031803, arXiv:1607.01789 [hep-ph].

[216] C. McCabe, "New constraints and discovery potential of sub-GeV dark matter with xenon detectors," *Phys. Rev.* **D96** (2017) 043010, arXiv:1702.04730 [hep-ph].

[217] G. Servant and T. M. P. Tait, "Is the lightest Kaluza-Klein particle a viable dark matter candidate?," *Nucl. Phys.* **B650** (2003) 391–419, arXiv:hep-ph/0206071 [hep-ph].

[218] H.-C. Cheng, J. L. Feng, and K. T. Matchev, "Kaluza-Klein dark matter," *Phys. Rev. Lett.* **89** (2002) 211301, arXiv:hep-ph/0207125 [hep-ph].

[219] M. Kakizaki, S. Matsumoto, Y. Sato, and M. Senami, "Significant effects of second KK particles on LKP dark matter physics," *Phys. Rev.* **D71** (2005) 123522, arXiv:hep-ph/0502059 [hep-ph].

[220] D. Feldman, Z. Liu, and P. Nath, "PAMELA Positron Excess as a Signal from the Hidden Sector," *Phys. Rev.* **D79** (2009) 063509, arXiv:0810.5762 [hep-ph].

[221] M. Ibe, H. Murayama, and T. T. Yanagida, "Breit-Wigner Enhancement of Dark Matter Annihilation," *Phys. Rev.* **D79** (2009) 095009, arXiv:0812.0072 [hep-ph].

[222] W.-L. Guo and Y.-L. Wu, "Enhancement of Dark Matter Annihilation via Breit-Wigner Resonance," *Phys. Rev.* **D79** (2009) 055012, arXiv:0901.1450 [hep-ph].

Appendix A

Decay Product Distributions

We summarize analytic results for the kinematic distributions of the dark photon decay products, presenting the forward velocity difference between the two final states and the lab frame opening angle, which may be used to determine the time delay and track separation between these objects in a detector. For simplicity, we assume the dark photon decays isotropically in its rest frame. Angular correlations will modify our distributions, but will not change the ranges of time delay and track separation, which are our primary interest. With this approximation, in the center-of-mass frame, the dark photon decay products are evenly distributed in $\cos\theta_{\mathrm{CM}}$, where θ_{CM} is the angle between the dark photon boost direction and one of the decay products. The value of a kinematic quantity k for fixed model parameters is a function κ of $\cos\theta_{\mathrm{CM}}$. The distribution of these values f is

$$f(k) = \sum_{\cos\theta^i_{\mathrm{CM}}}^{\kappa(\cos\theta^i_{\mathrm{CM}})=k} \frac{1}{|\kappa'(\cos\theta^i_{\mathrm{CM}})|} \ . \tag{A.1}$$

Throughout this appendix we consider two-body decays $A' \to f\bar{f}$ and define

$$a = \frac{2m_f}{m_{A'}} \qquad\qquad b = \frac{m_{A'}}{m_X} \ . \tag{A.2}$$

A.1 Velocity Distribution and Time Delay

In the Earth's rest frame, the forward velocities of the particles produced in A' decay are

$$u_\pm = \frac{\sqrt{1-b^2} \pm \sqrt{1-a^2}\cos\theta_{\rm CM}}{1 \pm \sqrt{1-b^2}\sqrt{1-a^2}\cos\theta_{\rm CM}} \ , \tag{A.3}$$

where we use natural units $c = 1$. The difference of these velocities is

$$\Delta u \equiv u_+ - u_- = \frac{2b^2\sqrt{1-a^2}\cos\theta_{\rm CM}}{1-(1-b^2)(1-a^2)\cos^2\theta_{\rm CM}} \approx \frac{2b^2\sqrt{1-a^2}\cos\theta_{\rm CM}}{1-(1-a^2)\cos^2\theta_{\rm CM}} \ , \tag{A.4}$$

where the last expression is valid for $b \ll 1$, the values we are most interested in. We plot $\Delta u(\cos\theta_{\rm CM})$ in Fig. A.1. Observe that Δu scales like b^2 for small b; this is also seen in Fig. 2.5, where the $m_X = 1$ TeV and $m_X = 10$ TeV plots are related by a simple rescaling. Further, the distribution is fairly insensitive to $a = 2m_\ell/m_{A'}$ for $m_{A'} \sim$ GeV and for $\ell = e, \mu$.

For a given Δu, the (dimensionful) time delay between the two decay products for a decay that occurs a distance L from the detection point is

$$\Delta t = \frac{L}{cu_-} - \frac{L}{cu_+} = \frac{L\Delta u}{cu_-u_+} \approx \frac{L}{c}\Delta u \ , \tag{A.5}$$

where we've taken the limit of large boost so that $u_\pm \to 1$.

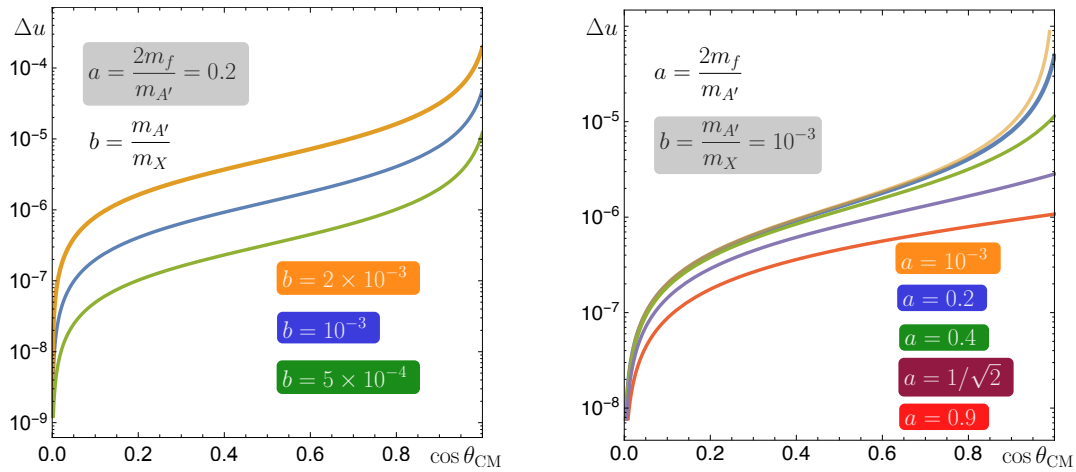

Figure A.1: Velocity difference, Δu, of the two particles produced in A' decay as a function of the center-of-mass frame angle $\cos\theta_{\rm CM}$ for representative values of a and b.

A.2 Opening Angle and Track Separation

In the Earth's rest frame, the angles $\theta_\pm$ of the decay products relative to the A' decay direction are

$$\tan\theta_\pm = \frac{\pm b\sqrt{1-a^2}\sin\theta_{\rm CM}}{\sqrt{1-b^2} \pm \sqrt{1-a^2}\cos\theta_{\rm CM}} \ . \tag{A.6}$$

The opening angle between the two decay products is therefore

$$\Delta\theta_{\rm lab} \equiv \tan^{-1}\theta_+ - \tan^{-1}\theta_- \approx \frac{2b\sqrt{1-a^2}\sin\theta_{\rm CM}}{1-(1-a^2)\cos^2\theta_{\rm CM}} \ , \tag{A.7}$$

where the last expression is valid for $b \ll 1$. The scaling $\Delta\theta_{\rm lab} \propto b$ can be seen in the center and right plots in Fig. 2.6. The maximal opening angle is

$$\Delta\theta_{\rm lab}^{\rm max} = \begin{cases} 2b\sqrt{1-a^2} \text{ at } \cos\theta_{\rm CM} = 0 \ , & a \geq \frac{1}{\sqrt{2}} \\ \frac{b}{a} \text{ at } \cos\theta_{\rm CM} = \sqrt{\frac{1-2a^2}{1-a^2}} \ , & a < \frac{1}{\sqrt{2}} \end{cases} \ . \tag{A.8}$$

We plot $\Delta\theta_{\rm lab}(\cos\theta_{\rm CM})$ in Fig. A.2. For large a, the opening angle is maximized at $\cos\theta_{\rm CM} =$

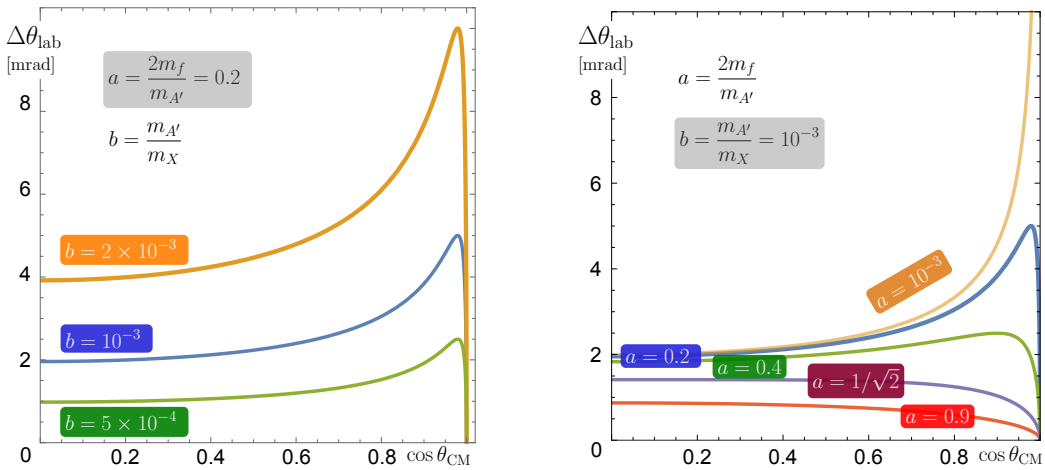

Figure A.2: Earth-frame opening angle between the two particles produced in A' decay as a function of the center-of-mass frame angle $\cos\theta_{\rm CM}$ for representative values of a and b.

0, consistent with the intuition that the largest opening angle should correspond to fully transverse decays in the center-of-mass frame. But for small a, this intuition does not hold: the maximal opening angle occurs for $\cos\theta_{\rm CM} \approx 1$, where one particle is emitted "backwards" in the A' center-of-mass frame so that its forward velocity is significantly reduced, enlarging the opening angle. In most of the range of $\cos\theta_{\rm CM}$, $\Delta\theta_{\rm lab} \approx 2b$, but the maximal opening angle $\Delta\theta_{\rm lab}^{\rm max} \approx b/a$ occurs for large $\cos\theta_{\rm CM} \approx 1 - \frac{1}{2}a^2$.

Finally we show the correlation between $\Delta\theta_{\rm lab}$ and Δu in Fig. A.3. These plots identify where one may use the combination of the opening angle and time delay to discriminate the two final state particles.

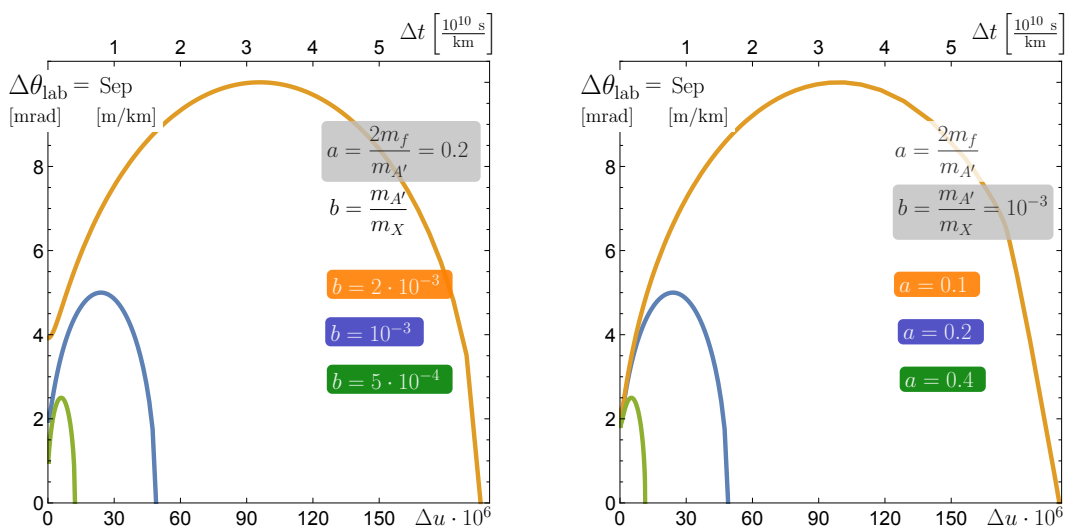

Figure A.3: The correlation between the velocity difference and the lab-frame opening angle of the two particles produced in A' decay for representative values of a and b.

Appendix B

Diagonalization of the Dark Photon Hamiltonian

Here we present a systematic derivation of the transformation from the dark photon gauge eigenstates to the mass eigenstates. The results in this appendix are known in the literature, see e.g. [151, 152]; we present the derivation for clarification and to establish conventions. For simplicity, in this appendix we write the field strengths as $A'_{\mu\nu} = \partial_{[\mu} A'_{\nu]}$.

B.1 Kinetic Mixing Between Massless and Massive Abelian Gauge Bosons

We first examine the case of a massive U(1) gauge boson, D, mixing with a massless U(1) gauge boson, B. This is the diagonalization relevant for a dark photon ($D = A'$) which kinetically mixes with hypercharge in the limit $m_D \ll v$ so that the mixing is effectively only

with the photon ($B = A$). The gauge-basis Lagrangian is

$$\mathcal{L} = -\frac{1}{4}D_{\mu\nu}D^{\mu\nu} - \frac{1}{4}B_{\mu\nu}B^{\mu\nu} + \frac{\varepsilon}{2}B_{\mu\nu}D^{\mu\nu} + \frac{1}{2}m_D^2 D_\mu D^\mu \ . \tag{B.1}$$

We first remove the kinetic mixing term with a $\pi/4$ rotation,

$$D = \frac{D_1 - B_1}{\sqrt{2}} \qquad\qquad B = \frac{D_1 + B_1}{\sqrt{2}} \ , \tag{B.2}$$

where B_1 and D_1 are the rotated fields. The kinetic terms are now diagonal, but are not canonically normalized,

$$\mathcal{L} = -\frac{1}{4}(1-\varepsilon)D_{1\mu\nu}D_1^{\mu\nu} - \frac{1}{4}(1+\varepsilon)B_{1\mu\nu}B_1^{\mu\nu} + \frac{1}{4}m_D^2(D_1 - B_1)_\mu(D_1 - B_1)^\mu \ . \tag{B.3}$$

To canonically normalize the kinetic terms, we perform a rescaling,

$$D_1 = \frac{D_2}{\sqrt{1-\varepsilon}} \qquad\qquad B_1 = \frac{B_2}{\sqrt{1+\varepsilon}} \ . \tag{B.4}$$

With this, the kinetic terms are now universal and do not transform under subsequent rotations so that we are free to diagonalize the mass term. Were it not for the rescaling in Eq. (B.4), this would simply be a $-\pi/4$ rotation. Plugging in a general rotation,

$$D_2 = c_3 D_3 - s_3 B_3 \qquad\qquad B_2 = s_3 D_3 + c_3 B_3 \ , \tag{B.5}$$

one finds that the mass matrix is diagonalized when[1]

$$s_3 = -\sqrt{\frac{1-\varepsilon}{2}} \qquad\qquad c_3 = \sqrt{\frac{1+\varepsilon}{2}} \ . \tag{B.6}$$

[1] A shortcut to obtain this result is to observe that invariance of the unbroken U(1) gauge symmetry implies that the mass term for B_3 should also vanish. This coefficient of the mass matrix is simpler to solve than the off-diagonal element and gives $s_3 \propto \pm\sqrt{1-\varepsilon}$ and $c_3 \propto \mp\sqrt{1+\varepsilon}$.

The choice of sign amounts to the sign of the B coupling. Plugging this in gives the transformation from the gauge to energy eigenbasis:

$$D = \frac{1}{\sqrt{1-\varepsilon^2}} D_3 \qquad\qquad B = B_3 + \frac{\varepsilon}{\sqrt{1-\varepsilon^2}} D_3 \ . \tag{B.7}$$

From this we see that the dark photon picks up an $\mathcal{O}(\varepsilon)$ coupling to the B-current, $j_B \cdot B \supset \varepsilon_{\text{eff}} j_B \cdot D_3$, where $\varepsilon_{\text{eff}} = \varepsilon/\sqrt{1-\varepsilon^2}$, while the B does not pick up any coupling to the dark current as expected by gauge invariance. The dark photon mass is rescaled to $m_D/\sqrt{1-\varepsilon^2}$.

For the case where $m_D = 0$, the gauge Lagrangian is diagonalized and normalized after Eq. (B.4) and the rotation in Eq. (B.5) with parameters in Eq. (B.6) is not strictly necessary. In fact, in this case one may chose to rotate the D_2 and B_2 into each other with any arbitrary SO(2) rotation. The choice in Eq. (B.6) is convenient because it is close to the gauge basis. Phenomenologically, however, it is common to pick a rotation such that the ordinary photon couples to the dark current proportional to ε so that the dark matter appears to be millicharged under electromagnetism. Ref. [152] calls this the Holdom phase. This interpretation is equivalent since in the case where m_D is negligibly small, the photon and dark photon propagators are identical. Whether a process is identified as coming from a dark photon with ε coupling to j_{EM} or an ordinary photon with ε coupling to j_X is equivalent; and in general both diagrams must be included.

B.2 Dark Photon–Hypercharge Mixing

The dark photon–photon mixing is only an effective description since at high energies one must satisfy electroweak gauge invariance. This imposes that the UV mixing is actually between the dark sector U(1) and hypercharge, which is itself broken by the Higgs vev, v. Thus one must generically consider the mixing between the D, the photon A, and the Z

boson. The amount of D–A mixing versus D–Z mixing determines the extent to which the D picks up the electroweak chiral couplings versus the vector-like electromagnetic couplings.

The hypercharge boson is related to the SM mass eigenstates by $B = -s_W Z + c_W A$. The mixing in Eq. (B.1) is thus

$$\frac{\varepsilon}{2} B_{\mu\nu} D^{\mu\nu} = -\frac{\varepsilon s_W}{2} Z_{\mu\nu} D^{\mu\nu} + \frac{\varepsilon c_W}{2} A_{\mu\nu} D^{\mu\nu} \ , \tag{B.8}$$

with A massless and Z picking up an electroweak symmetry breaking mass of M_Z. The D–A system is now identical to the D–B system above, so we may diagonalize using the transformation in Eq. (B.7),

$$D = \frac{1}{\sqrt{1-\varepsilon^2 c_W^2}} D_1 \qquad A = A_1 + \frac{\varepsilon c_W}{\sqrt{1-\varepsilon^2 c_W^2}} D_1 \qquad Z = Z_1. \tag{B.9}$$

This diagonalizes and canonically normalizes the D–A system, but also changes the kinetic mixing between the D and Z:

$$-\frac{\varepsilon s_W}{2} Z_{\mu\nu} D^{\mu\nu} = -\frac{1}{2} \frac{\varepsilon s_W}{\sqrt{1-\varepsilon^2 c_W^2}} Z_{1\mu\nu} D_1^{\mu\nu} = -\frac{\varepsilon_s}{2} Z_{1\mu\nu} D_1^{\mu\nu} \ . \tag{B.10}$$

In the above equation we have defined for convenience a new D–Z mixing parameter ε_s

$$\varepsilon_s \equiv \frac{\varepsilon s_W}{\sqrt{1-\varepsilon^2 c_W^2}} \ . \tag{B.11}$$

This kinetic mixing is removed with a $\pi/4$ rotation and canonical normalization is restored with a subsequent rescaling analogous to Eqs. (B.2),(B.4):

$$D_1 = \frac{D_2 - Z_2}{\sqrt{2}} \qquad Z_1 = \frac{D_2 + Z_2}{\sqrt{2}} \tag{B.12}$$

$$D_2 = \frac{D_3}{\sqrt{1+\varepsilon_s}} \qquad Z_2 = \frac{Z_3}{\sqrt{1-\varepsilon_s}} \ . \tag{B.13}$$

Unlike the previous case of a mixing between a massive and massless state, the D–Z system is a mixing between two massive states. The mass matrix is diagonal in the (D, A, Z) basis where D is a gauge eigenstate and A and Z are mass eigenstates with respect to the electroweak symmetry-breaking mass terms. Note that the A has now decoupled completely and it is sufficient to consider the D–Z system independently. For convenience, we perform a $-\pi/4$ rotation, which captures most of the rotation in Eq. (B.5):

$$D_3 = \frac{D_4 + Z_4}{\sqrt{2}} \qquad\qquad Z_3 = \frac{Z_4 - D_4}{\sqrt{2}} \ . \tag{B.14}$$

The original D and Z fields may now be written as

$$D = a\left(\Delta D_4 + \delta Z_4\right) \qquad\qquad Z = \Delta Z_4 + \delta D_4 \ , \tag{B.15}$$

where we define convenient shorthand,

$$a = \frac{1}{\sqrt{1-\varepsilon^2 c_W^2}} \qquad = 1 + \frac{1}{2}\varepsilon^2 c_W^2 + \mathcal{O}(\varepsilon^3) \tag{B.16}$$

$$\Delta = \frac{1}{2}\left(\frac{1}{\sqrt{1+\varepsilon_s}} + \frac{1}{\sqrt{1-\varepsilon_s}}\right) = 1 + \frac{3}{8}\varepsilon_s^2 + \mathcal{O}(\varepsilon^3) \tag{B.17}$$

$$\delta = \frac{1}{2}\left(\frac{1}{\sqrt{1+\varepsilon_s}} - \frac{1}{\sqrt{1-\varepsilon_s}}\right) = -\frac{1}{2}\varepsilon_s + \mathcal{O}(\varepsilon^4) \ . \tag{B.18}$$

The mass term is then

$$\frac{1}{2}\begin{pmatrix} D & Z \end{pmatrix}\begin{pmatrix} m_D^2 & \\ & M_Z^2 \end{pmatrix}\begin{pmatrix} D \\ Z \end{pmatrix} = \frac{1}{2}\begin{pmatrix} D_4 & Z_4 \end{pmatrix}\begin{pmatrix} M_{11}^2 & M_{12}^2 \\ M_{12}^2 & M_{22}^2 \end{pmatrix}\begin{pmatrix} D_4 \\ Z_4 \end{pmatrix} \ , \tag{B.19}$$

where the elements on the right-hand side are, writing $\bar{m}_D^2 \equiv a^2 m_D^2$,

$$M_{11}^2 = \Delta^2 \bar{m}_D^2 + \delta^2 M_Z^2 \sim m_D^2 + \mathcal{O}(\varepsilon^2) \tag{B.20}$$

$$M_{22}^2 = \Delta^2 M_Z^2 + \delta^2 \bar{m}_D^2 \sim M_Z^2 + \mathcal{O}(\varepsilon^2) \tag{B.21}$$

$$2M_{12}^2 = 2\delta\Delta(\bar{m}_D^2 + M_Z^2) \sim -\varepsilon_s(m_D^2 + M_Z^2) + \mathcal{O}(\varepsilon^3) \ , \tag{B.22}$$

One may now perform a final rotation to go the the mass eigenstates of the system. Observe that the off-diagonal element of the mass matrix is proportional to ε, so that the rotation is small in the small ε limit. Writing $c = \cos\theta$ and $s = \sin\theta$, the rotation is given by

$$D_4 = cD_5 + sZ_5 \qquad Z_4 = cZ_5 - sD_5 \qquad \tan 2\theta = \frac{2M_{12}^2}{M_{22}^2 - M_{11}^2} \ , \tag{B.23}$$

where c and s are written to $\mathcal{O}(\varepsilon^2)$ as

$$c = 1 + \mathcal{O}(\varepsilon^2) \qquad s = -\frac{\varepsilon_s}{2}\frac{m_D^2 + M_Z^2}{M_Z^2 - m_D^2} + \mathcal{O}(\varepsilon^3) \ . \tag{B.24}$$

Plugging in the sequence of rotations in Eqs. (B.9), (B.12), (B.13), (B.14), (B.23), the electroweak basis and mass basis are related by

$$D = \frac{\Delta c - \delta s}{\sqrt{1-\varepsilon^2 c_W^2}} D_5 + \frac{\Delta s + \delta c}{\sqrt{1-\varepsilon^2 c_W^2}} Z_5 \qquad Z = (\Delta c + \delta s) Z_5 + (\delta c - \Delta s) D_5 \tag{B.25}$$

$$= D_5 - \frac{\varepsilon_s M_Z^2}{M_Z^2 - \bar{m}_D^2} Z_5 + \mathcal{O}(\varepsilon^2) \qquad = Z_5 + \frac{\varepsilon_s \bar{m}_D^2}{M_Z^2 - \bar{m}_D^2} D_5 + \mathcal{O}(\varepsilon^2) \tag{B.26}$$

$$= D_5 - \varepsilon_s Z_5 + \mathcal{O}(\varepsilon^2, \frac{m_D^2}{M_Z^2}) \qquad = Z_5 + \varepsilon_s \frac{m_D^2}{M_Z^2} D_5 + \mathcal{O}(\varepsilon^2, \frac{m_D^2}{M_Z^2}) \ . \tag{B.27}$$

From this we observe that D_5 couples to the weak neutral current suppressed by $\varepsilon_s m_D^2/M_Z^2$, so that in the $m_D \ll m_Z$ limit the Standard Model couplings are effectively vector-like coming from the mixing with the photon. In this limit one may disregard the D–Z mixing relative to the D–A mixing.